2016

Guided Wave Inspection Of Cracks In The Rivet Hole Of An Aerospace Lap Joint Using Analytical-Fem Approach

Md Yeasin Bhuiyan
University of South Carolina

Recommended Citation

Bhuiyan, M. Y.(2016). *Guided Wave Inspection Of Cracks In The Rivet Hole Of An Aerospace Lap Joint Using Analytical-Fem Approach.* (Master's thesis). Retrieved from https://scholarcommons.sc.edu/etd/3915

GUIDED WAVE INSPECTION OF CRACKS IN THE RIVET HOLE OF AN AEROSPACE LAP JOINT USING ANALYTICAL-FEM APPROACH

by

Md Yeasin Bhuiyan

Bachelor of Science
Bangladesh University of Engineering & Technology, 2011

Master of Science
Bangladesh University of Engineering & Technology, 2013

Submitted in Partial Fulfillment of the Requirements

For the Degree of Master of Science in

Aerospace Engineering

College of Engineering and Computing

University of South Carolina

2016

Accepted by:

Victor Giurgiutiu, Director of Thesis

Sourav Banerjee, Reader

Cheryl L. Addy, Vice Provost and Dean of the Graduate School

DEDICATION

This work is dedicated to my wife, Tunazzena Mubashsharah Alam, who has been a constant source of support and encouragement during the challenges of my life. This work is also dedicated to my parents, brothers, and sisters who have always loved me unconditionally and whose good examples have taught me to work hard for the things that I aspire to achieve.

ACKNOWLEDGEMENTS

I would like to express my sincere gratitude to my academic advisor, Dr. Victor Giurgiutiu, for his strong support, knowledgeable guidance, and giving me the opportunity to join the Laboratory of Active Materials and Smart Structures (LAMSS). It has been such a rewarding experience to be his student. His passionate attitude toward science and enlightening instruction has helped me overcome many difficulties. This will remain as life-time encouragement in my future career.

I would also like to thank Dr. Sourav Banerjee for being the second reader and his valuable suggestions toward my thesis. I would like to thank my dear colleagues of LAMSS group especially Dr. Jingjing Bao and Dr. Bin Lin for their valuable suggestions. I would like to thank Dr. Yangfen Shen for his valuable guidance toward my research. Special thanks to my colleague Banibrata Poddar for conceptual discussion and experiments on the wave problems. I would also like to thank my dear friends Erik Frankforter, William Roth, Roshan Joseph, Mohammad Faisal Haider, Hanfei Mei for their constructive suggestion on my thesis.

The following funding supports are thankfully acknowledged: Office of Naval Research # N00014-14-1-0655, Dr. Ignacio Perez, Technical Representative; Air Force Office of Scientific Research #FA9550-11-1-0133, Dr. David Stargel, Program Manager.

ABSTRACT

Ultrasonic guided waves are very attractive for the inspection of large structures using nondestructive evaluation (NDE) and structural health monitoring (SHM) technique. Combined analytical and finite element analysis (CAFA) has been introduced for the detection of butterfly cracks in the rivet hole of the aerospace lap joint. Finite element analyses have been performed on the local damage area in spite of the whole large structure. Fundamental Lamb wave modes (S0 and A0) have been strike on the local damage from multiple directions to analyze the cracks of multiple-rivet-hole lap joint. The rivet hole cracks (damage) in the plate structure gives rise to the non-axisymmetric scattering of Lamb wave as well as shear horizontal (SH) wave although the incident Lamb wave source (primary source) is axisymmetric. Hence, the damage in the plate acts as a non-axisymmetric secondary source of Lamb wave and SH wave. The non-axisymmetric scattering of Lamb and SH waves are described using the wave damage interaction coefficient (WDIC). The WDIC of scattered Lamb and SH waves depends on the azimuth directions of the rivet hole as well as the frequencies of excitation.

The WDIC involves scattering and mode conversion of Lamb waves occurred due to local damage. WDIC is captured around the damage for each direction of incidence over the frequency domain and “scatter cube” is formed for each incident Lamb mode. By analyzing the scattered cube of WDICs over the frequency domain and azimuth directions, the optimum parameters (frequency and location of sensor) can be determined for each angle of incidence. The scatter cubes are fed into the exact analytical framework

to produce the time domain signal. This analysis enables us to obtain the optimum design parameters for better detection of the cracks in the rivet holes. The optimum parameters can be obtained for all possible cases of incident Lamb waves that would help to analyze the multiple-rivet-hole problem. Some examples of obtaining the optimum parameters are illustrated based on the most prominent time domain signal. The optimum parameters provide the guideline of the design of the sensor installation to obtain the most noticeable signals that represent the presence of cracks in the rivet hole.

The thesis finishes with conclusions, and suggestions for future work.

TABLE OF CONTENTS

LIST OF FIGURES

CHAPTER 1

INTRODUCTION

Structural Health Monitoring (SHM) is an emerging multi-disciplinary field which aims at detecting/characterizing structural damage and providing diagnosis/prognosis of structural health status in a real-time or on-demand manner. With the advancement of SHM technology, the industry can reduce the maintenance cost, shorten the machine service down time, and improve the safety and reliability of engineering structures. It has shown great potential in both the health management of aging structures and the development of novel self-sensing smart structures. This chapter serves as the introduction to the entire thesis by addressing the motivation and importance of conducting the research, discussing research goal, scope, and objectives will be discussed, and introducing the organization of the thesis.

1.1 MOTIVATION

The detection of various types of defects in the structures, for example, corrosion, cracks, impact, disbands etc is an important research area of SHM and NDE. Corrosion and fatigue cracks development at the rivet holes and fasteners in the aircraft structures is the most frequent problem of the aircraft maintenance. The aircraft structural integrity program (ASIP) allows having some type of internal damage in all in-service aircraft structures (a.k.a., airframes) which is undetectable with the existing nondestructive inspection methods (NDI) [1][2]. However, the airframes should be damage tolerant and hence safe to fly with such ‘initial flaws” The consistent application of the requirements of ASIP has prevented structural failures due to fatigue, stress corrosion, and corrosion-fatigue. However, during the operation cycle of an aircraft, the cracks in the structure can grow to a critical size and jeopardize the structural integrity if they remain undetected.

1.1.1 COST OF UNDETECTED FATIGUE CRACK

In 1989, the united airlines flight 232 (DC-10) crash landed in the airport due to one of the engines failure (Figure 1.1). The failed stage 1 fan disk came out of the engine nacelle during inflight in the air and damaged the three hydraulics situated next to the engine. The subsequent catastrophic disintegration of the disk resulted in the liberation of debris in a pattern of distribution The debris of the failed engine also damaged the horizontal stabilizer as shown in Figure 1.2. The main reason of the catastrophic failure of the fan disk was the fatigue crack of 13 mm that occurred during its 17 years of service and remained undetected due to the human factors limitaions in the nondestructive inspection (NDI) [3].

Ultrasonic guided wave methods can be employed instead of the laborious point by point inspection method for fast, accurate and efficient detection of the crack inauguration in the riveted holes and/or from any manufacturing flaws.

1.1.2 LAP JOINTS IN AIRCRAFT STRUCTURES

A section of the fuselage lap joints of a Boeing 737-200 is shown in Figure 1.3. It shows that along a lap joint there are thousands of rivets. Any crack initiating form any one of the rivets can ruin the integrity of the metal along the entire aircraft lap joint. The Federal Aviation Administration (FAA) recently grounded three passenger jets due to "scribe marks" and has identified 32 more Boeing planes with damaging box cutter-type cuts along the lap joint. The investigators discovered cracks, corrosion and weakened

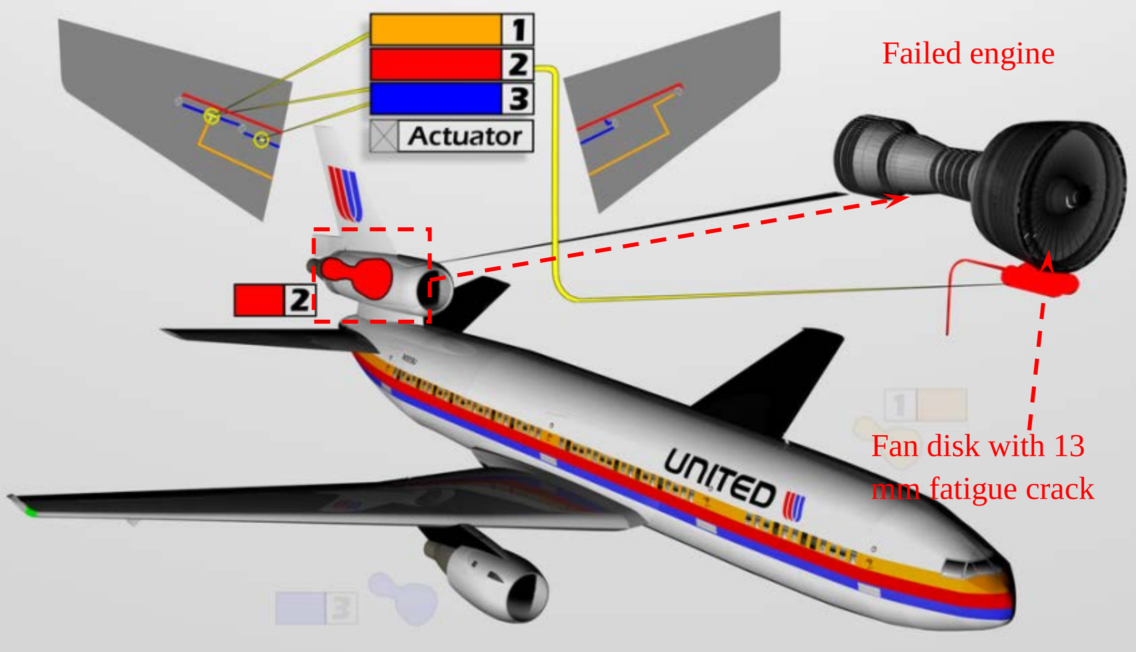

Figure 1.1: Engine failure of UA flight 232 due to a fatigue crack in the fan disk [4]

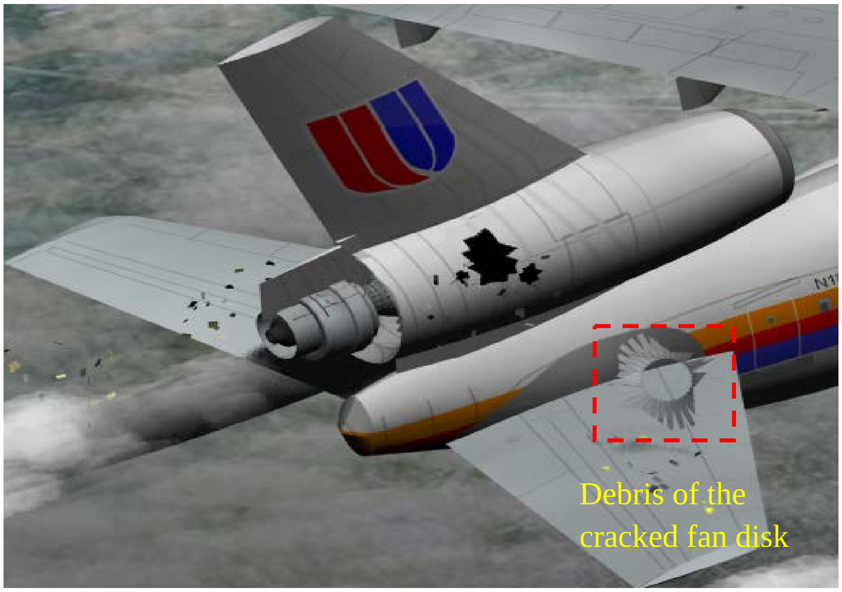

Figure 1.2: The debris of the failed fan disk came out of the engine nacelle [4]

metal hidden inside a growing number of Boeing passenger jets. A big new problem for Boeing is centered on "lap-joint metal fatigue" also called "scoring". Spotting the fatigue cracks in the lap joints on the outside of an aircraft, through the paint, is nearly impossible for the usual NDI.

Figure 1.3: Riveted lap joints on the fuselage of Boeing B737 (Courtesy: Boeing Company)

1.1.3 POSSIBLE DAMAGES IN THE LAP JOINTS

The riveted lap joint of an aircraft fuselage in the manufacturing stage is shown in Figure 1.4a. Under critical loading condition the cracks are initiated from the rivets and sometimes widespread fatigue damage (WFD) could happen as shown in Figure 1.4b WFD in an airplane’s structure is defined as the simultaneous presence of cracks at multiple locations that are of sufficient size and density that the structure will no longer meet required damage tolerance and will not maintain required residual strength after partial structural failure. The risk of WFD onset increases as airplanes are operated well past their original design objectives in flight cycles or flight hours.

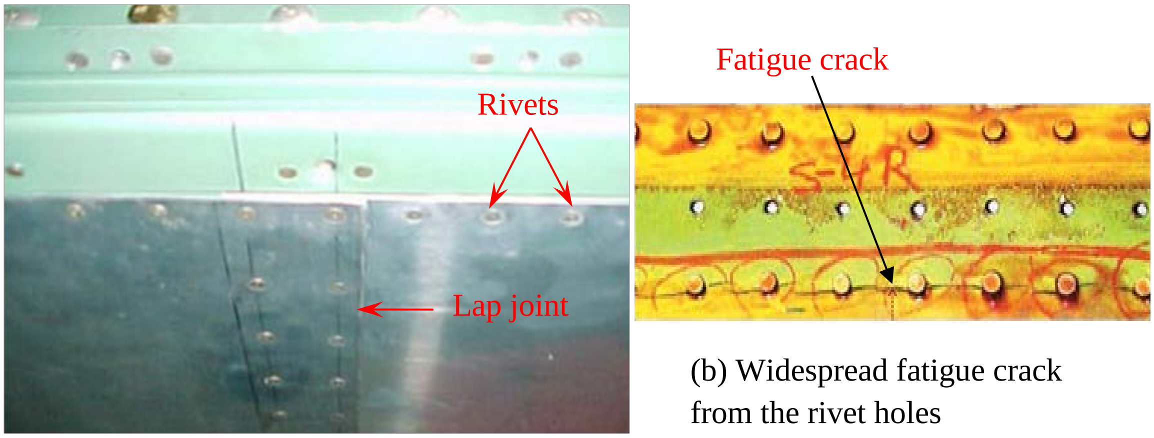

(b) Widespread fatigue crack from the rivet holes

(a) Riveted section of a fuselage

Figure 1.4: (a) Riveted lap joint of a fuselage (b) Widespread fatigue cracks from the rivet holes [5]

As part of rule compliance, Boeing is required to identify WFD-susceptible areas for both the as-delivered structure and any structure that required modification by an airworthiness directive (AD). Boeing also must predict which of the identified WFD-susceptible areas will develop WFD prior to when the limits of validity (LOV) is reached and provide service bulletin actions to prevent that development (Figure 1.5b). These service actions would be in the form of service bulletins that would require inspection, modification, or both. The FAA issued an AD to make these service bulletins mandatory[5].

1.1.4 Pioneer Researches on Cracks in the Rivet Holes

Over the topical years, the detection of cracks around the rivet hole has become an important topic of the NDE reasearch field. In 2009, the probability of detection (POD) by model-assisted approach has been demonstrated for the fatigue crack growth in wing lap joint, wing skin fastener holes, airframe fastener holes [6]. In 2012, the use of the transfer function approach to model-assisted POD is investigated by Bode et al.[7]

through the inspection of a specimen of aircraft lap joint. However, the researches emphasized the detection of fastener hole cracks mainly based on nondestructive inspection (NDI) technique.

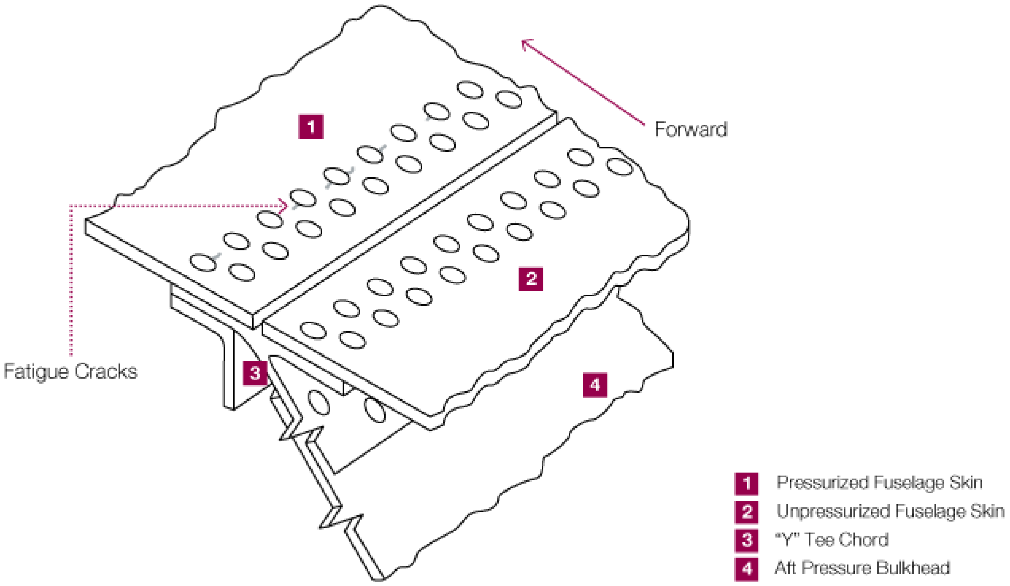

Figure 1.5: Example of multiple-rivet-hole lap joint structure susceptible to WFD [5]

In 2015, the SHM based POD was obtained for the fatigue crack initiation in the lug with a wing attachment which acted as a representative airplane component [8]. The excitation signals of 200 kHz to 1000 kHz center frequency were used to analyze the guided waves within fundamental Lamb wave modes. In 2014, Fu-Kuo Chang group [9] used ultrasonic SHM techniques to detect the damage and showed the variation of damage index with crack size. They determined the most influencing parameters to the sensitivity of damage detection and compared the SHM and NDE techniques. A set of transmitter and receiver sensors were used around the cracked rivet hole. However, the study of the proper location of the installed sensors around the damage was not described. The motivation and importance of the present research work has been derived from these researches.

1.2 RESEARCH GOAL, SCOPE, AND OBJECTIVES

The development of computational models for Lamb wave propagation and interaction with damage is of great importance for both SHM system design and signal interpretation purposes. Effective design of SHM systems requires the exploration of a wide range of parameters (transducer size, sensor-damage relative locations, interrogating wave characteristics, etc.) to achieve the best detection and quantification of certain types of damage. On the other hand, active sensing signals using Lamb waves are usually difficult to interpret due to the multi-mode and dispersive nature of Lamb waves. Their interaction with damage involves even more complex scattering and mode conversion phenomena.

Practical applications have imposed three main requirements on computational models: (1) accuracy for high frequency, short wavelength, and long propagation distance waves; (2) efficiency in terms of computational time and computer resources; and (3) versatility with a wide range of parameter exploration capabilities. However, these requirements have not been satisfied with conventional analytical methods or commercially available finite element software. Thus, it is of great importance to develop accurate, efficient, and versatile computational techniques for the simulation of guided wave based active sensing procedures.

In this thesis, the problem of Lamb wave scattering is explored more in the perspective of analyzing multiple-rivet-hole lap joint cracks. The detection of cracks in a multiple-rivet-hole lap joint is considered by analytical-FEM simulation which is an effective tool for the analysis in contrast to costly experimental investigation. Harmonic analysis is performed to the small-size 3-D model of the local damage using FEM. Both symmetric and anti-symmetric Lamb wave modes incident from multiple driections on the damage are analyzed and scattered coefficients are calculated around the damage corresponding to each incident direction. Wave-damage interaction coefficients (WDICs) are used to describe the scattering behaviour of the damage and “scatter cubes” are formed for both Lamb wave modes. The transfer function based on exact analytical model accompanied by “scatter cube” is used to find out the optimum center frequency of the toneburst signal from the actuator and the most damage sensitive location in the structure where the sensor can be installed. The most sensitive signal that contain the prominent damage signature is obtained analytically. Some simplified cases of the real problem has been demostrated through the simulated signals obtained using the combined analytical and FEM method.

1.3 ORGANIZATION OF THE THESIS

To achieve the objectives set forth in the preceding section, the thesis is organized in six chapters.

The motivation and importance of the research work is discussed in Chapter 1. It also introduces the scope, goal and contents of each chapter.

In Chapter 2, fundamentals of the guided wave theory are briefly reviewed, guided wave application to SHM is discussed, and fundamentals of the piezoelectric wafer active sensors (PWAS), tuning effect of the bonded PWAS on the structure are introduced.

In Chapter 3, SHM of a multiple-rivet-hole is described, a simplified representation of the multiple-rivet-hole is discussed, the concept of wave damage interaction coefficient (WDIC) is illustrated, analytical formulation of WDIC is developed for a simple case, the analytical and FEM results are compared.

In Chapter 4, the local FEM simulation of the combined FEM-analytical approach is discussed. The geometric information of the local damage model, modeling of the cracks, meshing, boundary conditions and loadings are discussed. The FEM results are discussed, the formation of scatter cube from the FEM results are illustrated. The scatter cubes of complex-valued WDICs are analyzed using both linear and polar plots.

In Chapter 5, the overview of the combined FEM-analytical approach is discussed and mainly focuses on the analytical part of this approach. It also discusses the coupling of the scatter cube into the analytical framework. The chapter presents some simulated signals corresponding to some cases of the multiple-rivet-hole problem and provides the optimum frequency of excitation and locations of the actuator and sensor.

In Chapter 6, the conclusions and future work are presented.

CHAPTER 2

FUNDAMENTAL STUDY OF GUIDED WAVES AND PIEZOELECTRIC WAFER ACTIVE SENSORS FOR STRUCTURAL HEALTH MONITORING

Structural health monitoring methods based on elastic waves propagation are very diverse and a vast area of study. In order to use ultrasonic elastic waves in nondestructive evaluation (NDE) and structural health monitoring (SHM), different types of waves must be studied to understand the underlying physical phenomena. This chapter deals with fundamentals of elastic waves and then an important class of elastic waves (*guided waves*) that have widespread applications in SHM. Guided waves are especially important for SHM because they can travel at large distances in structures with only little energy loss. Thus, they enable the SHM of large areas from a single location. Guided waves have the important property that they remain confined inside the walls of a thin–wall structure, and hence can travel over large distances. In addition, guided waves can also travel inside curved walls. These properties make them well suited for the ultrasonic inspection of aircraft, missiles, pressure vessels, oil tanks, pipelines, etc. This study will also serve as the theoretical prerequisite for the wave modeling and simulation tasks. This chapter also introduces fundamental study of Piezoelectric Wafer Active Sensors (PWAS) including their working principle, their coupling with guided waves and tuning effect, and their operation modes.

2.1 GENERAL THEORY OF ELASTIC WAVES

The fundamentals of guided elastic waves are sited in the study of elastodynamics. The backbone of classical elastodynamics is the Navier-Lame equations that represent the the equations of motion for homogeneous isotropic lineraly elastic solids [10], i.e.,

$$(\lambda+\mu)\vec{\nabla}(\vec{\nabla}\cdot\vec{u})+\mu\nabla^{2}\vec{u}=\rho\ddot{\vec{u}} \tag{2.1}$$

where, $\vec{u}$ is the displacement vector, ρ is the density, λ and μ are the Lame constants.

2.1.1 Wave Equations for Potentials

To construct the solutions of Navier-Lame equations, the displacement fields can be considered as the superposition of the gradient of scalar potential Φ and the curl of the vector potential $\vec{H}$. Use the Helmholtz theorem (mentioned originally in ref. [11] and then in its translated version [12]) to write

$$\vec{u}=grad\Phi+curl\vec{H}=\vec{\nabla}\Phi+\vec{\nabla}\times\vec{H} \tag{2.2}$$

Substitute Eq. (2.2) into Eq. (2.1) to get

$$(\lambda+\mu)\vec{\nabla}\left\{\vec{\nabla}\cdot(\vec{\nabla}\Phi+\vec{\nabla}\times\vec{H})\right\}+\mu\nabla^{2}(\vec{\nabla}\Phi+\vec{\nabla}\times\vec{H})=\rho(\vec{\nabla}\ddot{\Phi}+\vec{\nabla}\times\ddot{\vec{H}}) \tag{2.3}$$

Upon rearrangement,

$$(\lambda+2\mu)\vec{\nabla}(\nabla^{2}\Phi)+\mu\vec{\nabla}\times(\nabla^{2}\vec{H})+(\lambda+\mu)\vec{\nabla}\left\{\cancelto{\vec{0}}{\vec{\nabla}\cdot(\vec{\nabla}\times\vec{H})}\right\}=\rho(\vec{\nabla}\ddot{\Phi}+\vec{\nabla}\times\ddot{\vec{H}}) \tag{2.4}$$

Applying the general vector property $\vec{\nabla}\cdot(\vec{\nabla}\times\vec{H})=0$ (divergence of any curl is zero), the second term drops out. Then, Eq.(2.4) yields

$$(\lambda+2\mu)\vec{\nabla}(\nabla^{2}\Phi)+\mu\vec{\nabla}\times(\nabla^{2}\vec{H})=\rho(\vec{\nabla}\ddot{\Phi}+\vec{\nabla}\times\ddot{\vec{H}}) \tag{2.5}$$

Combining the similar potentials, Eq. (2.5) can be written as

$$\vec{\nabla}\left\{(\lambda+2\mu)\nabla^{2}\Phi-\rho\ddot{\Phi}\right\}+\vec{\nabla}\times(\mu\nabla^{2}\vec{H}-\rho\ddot{\vec{H}})=0 \tag{2.6}$$

Eq.(2.6) holds true for any space and time, and can be separated into two equations as follows

$$(\lambda+2\mu)\nabla^2\Phi-\rho\ddot{\Phi}=0 \tag{2.7}$$

$$\mu\nabla^2\vec{H}-\rho\ddot{\vec{H}}=0 \tag{2.8}$$

Assuming harmonic time variation with circular frequency ω and defining $c_p=\sqrt{(\lambda+2\mu)/\rho}$, $c_s=\sqrt{\mu/\rho}$, Eq. (2.7) and (2.8) become

$$\nabla^2\Phi+\frac{\omega^2}{c_p^2}\Phi=0 \quad \text{(scalar wave equation)} \tag{2.9}$$

$$\nabla^2\vec{H}+\frac{\omega^2}{c_s^2}\vec{H}=0 \quad \text{(vector wave equation)} \tag{2.10}$$

Eq. (2.9) indicates that the scalar potential Φ propagates with the pressure wavespeed c_p, whereas Eq. (2.10) indicates that the vector potential $\vec{H}$ propagates with the shear wavespeed c_s. It can be shown that the pressure waves are irrotational waves i.e., have zero rotation, whereas the shear waves are equivolume waves, i.e., they have zero dilatation and are known as distortional waves [10]. From now on, we call the scalar potential Φ as pressure potential and the vector potential $\vec{H}$ as shear potential.

The pressure waves are also known as *P waves* and shear waves can be divided into *SV waves* and *SH waves* depending on the polarization of the displacement. SV waves have vertically polarized displacement whereas SH waves have horizontally polarized displacement.

2.2 GUIDED WAVES

Under certain assumptions and boundary conditions the general elastic waves turns into guided waves. Ultrasonic guided waves are sensitive to changes in the propagating medium, such as plastic zone, fatigue zone, cracks, delamination, disbonds, discontinuity. This sensitivity exists for both surface damage and cross thickness/interior damage, because guided waves have various mode shapes throughout the cross section of the waveguides.

The assumption of straight crested wave or circular crested waves make the elastic wave problem to be split into two separate cases, (1) SH waves; and (2) P+SV waves. The P+SV waves in a plate give rise to the Lamb waves through multiple reflections on the plate's lower and upper surfaces, and through constructive and destructive interference. The Lamb waves consists of a pattern of standing waves in the thickness direction also known as Lamb wave modes.

2.2.1 SHEAR HORIZONTAL PLATE WAVES

Shear horizontal (SH) plate waves have a shear-type particle motion contained in the horizontal plane. Figure 2.1 shows the coordinate definition and particle motion of SH plate waves. According to the coordinate defined, an SH wave has the particle motion along the z axis, whereas the wave propagation takes place along the x axis. The particle motion has only the u_z component.

The phase velocity dispersion curve of the SH plate wave can be calculated as

$$c(\omega) = \frac{c_S}{\sqrt{1-(\eta d)^2\left(\frac{c_S}{\omega d}\right)^2}} \tag{2.11}$$

where η is given in Eq. (2.12) and d is the half plate thickness.

$$\eta^2 = \frac{\omega^2}{c_S^2} - \frac{\omega^2}{c^2} \tag{2.12}$$

By substituting the appropriate eigenvalue, one may obtain an analytical expression for the wave-speed dispersion curve of each SH wave mode. For detailed expressions, the readers are referred to ref.[18].

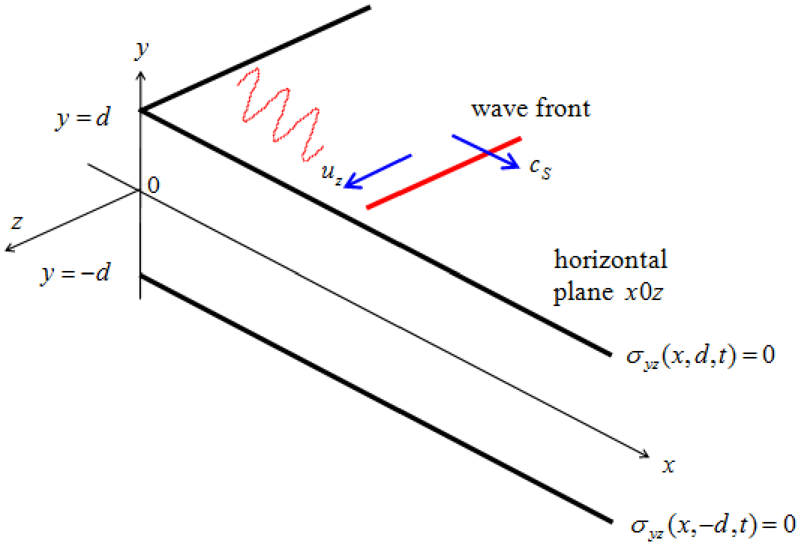

Figure 2.1: Coordinate definition and particle motion of SH plate waves[18].

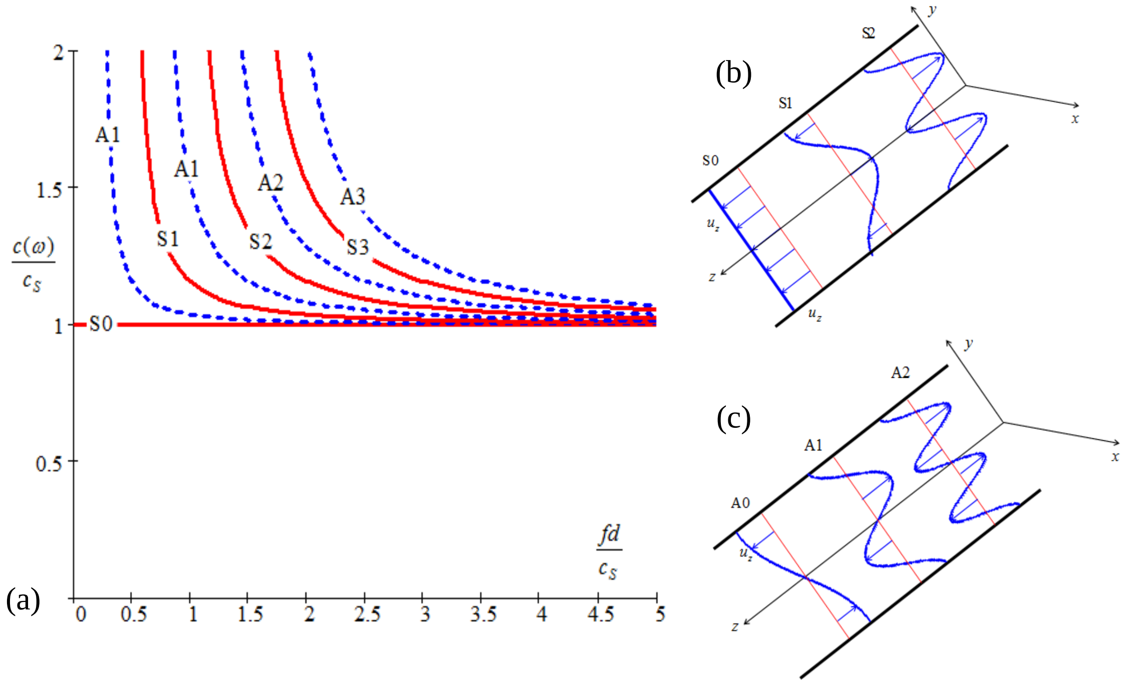

Figure 2.2: (a) SH plate wave-speed dispersion curves; (b) symmetric mode shapes; (c) antisymmetric mode shapes[18].

Figure 2.2 shows the wave-speed dispersion curve of SH plate waves and the mode shapes. It can be noticed that the fundamental symmetric mode (S0) wave is non-dispersive and always exists starting from low frequency-thickness product values. This nice property makes it a good candidate as the interrogating waves in SHM systems. Recently, considerable research has been carried out on the transmission and reception of SH plate wave for SHM [19][20]. Higher wave modes only appear beyond the corresponding cut-off frequencies, showing dispersive characteristics, i.e., their phase velocity changes with frequency. For dispersive waves, group velocity is usually used to evaluate the propagation of wave packets. The definition of group velocity is given in Eq. (2.13).

$$c_g = \frac{d\omega}{d\xi} \tag{2.13}$$

2.2.2 INCEPTION OF GAUGE CONDITION

It can be noted from Eq. (2.2) that three components of displacement are represented by the four components of potential functions. Hence, the new system of potential formulation needs additional condition to mitigate the requirement of additional unknown. This additional condition may be derived from the Navier-Lame equations.

Now let’s take a look at the dropped out term in Eq.(2.4), i.e.,

$$(\lambda+\mu)\vec{\nabla}\left\{\vec{\nabla}\cdot(\vec{\nabla}\times\vec{H})\right\}=\vec{0} \tag{2.14}$$

Using the vector property $\vec{\nabla}\left\{\vec{\nabla}\cdot(\vec{\nabla}\times\vec{H})\right\}=\vec{\nabla}\times\left\{\vec{\nabla}(\vec{\nabla}\cdot\vec{H})\right\}$, Eq. (2.14) can be written as

$$(\lambda+\mu)\vec{\nabla}\times\left\{\vec{\nabla}(\vec{\nabla}\cdot\vec{H})\right\}=\vec{0} \tag{2.15}$$

But $(\lambda+\mu)\neq 0$, hence, Eq. (2.15) can be written as

$$\vec{\nabla}\times\left\{\vec{\nabla}(\vec{\nabla}\cdot\vec{H})\right\}=\vec{0} \tag{2.16}$$

Letting, $\vec{\nabla}\cdot\vec{H}=\Gamma$, a scalar quantity, Eq. (2.16) becomes

$$\vec{\nabla}\times\left\{\vec{\nabla}\Gamma)\right\}=\vec{0} \tag{2.17}$$

Eq. (2.17) represents the vector property that curl of any gradient field is zero. Thus, Γ can be chosen arbitrarily without affecting the generality of the solution; this is called *gauge invariance.* This is similar to the *gauge invariance* used in solving the Maxwell's equations in electrodynamics through the potential approach (see section 2.5 of chapter 2 of ref. [13]). Owing to the uniqueness of the physical problem, any solution that satisfies the Navier-Lame equations be the unique solution to the problem, regardless of the value assumed by Γ.

The selection of the gauge depends on the nature of the problem. The simplest gauge condition may be selected as

$$\Gamma=\vec{\nabla}\cdot\vec{\mathrm{H}}=0 \tag{2.18}$$

However, the formula given in Eq.(2.18) is not the only possible form of the gauge condition; in fact, a multitude of alternative forms exist [13] as used in elastodynamics [10](pg. 465)[14], and electrodynamics [15] [16] [17].

2.2.3 STRAIGHT CRESTED LAMB WAVES

Lamb waves are a type of ultrasonic waves that are guided between two parallel free surfaces, such as the upper and lower surfaces of a plate. Lamb waves can exist in two basic types, symmetric and antisymmetric. Figure 2.3 shows the particle motion of symmetric and antisymmetric Lamb waves. The Lamb wave motion has asymptotic behavior at low frequency and high frequency. At low frequency, the symmetric mode resembles axial waves, while the antisymmetric mode resembles flexural waves. At high frequency, both symmetric and antisymmetric wave approaches Rayleigh waves, because the particle motion is strong at the surfaces and decays rapidly across the thickness. The axial wave and flexural wave, by their nature, are only low frequency approximations of Lamb waves. The plate structure cannot really sustain pure axial and flexural motion at large frequency-thickness product values.

Symmetric Lamb wave mode

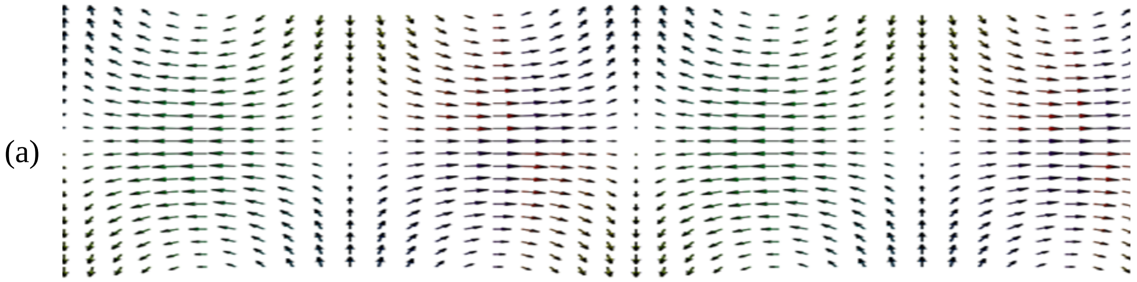

Antisymmetric Lamb wave mode

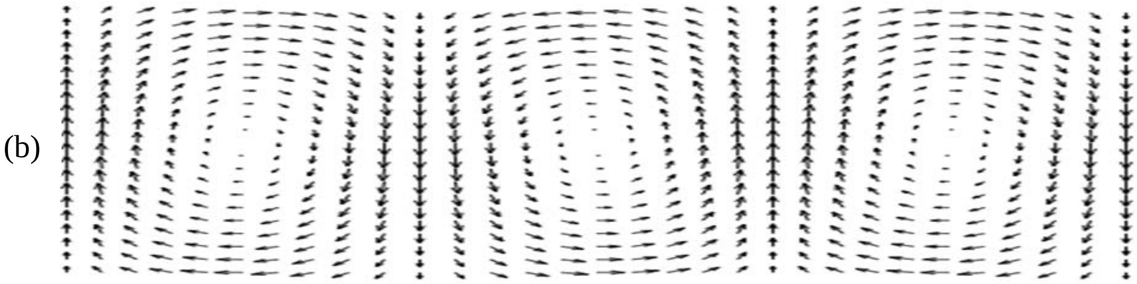

Figure 2.3: Particle motion of Lamb wave modes: (a) symmetric mode and (b) antisymmetric mode [18].

The straight crested Lamb wave equations are derived under z-invariant assumptions using pressure wave and shear vertical wave (P+SV) waves in a plate. Through multiple reflections on the plate’s lower and upper surfaces, and through constructive and destructive interference, the pressure waves and shear vertical waves give rise to the Lamb–waves, which consist of a pattern of standing waves in the thickness *y*–direction (Lamb–wave modes) behaving like traveling waves in the *x*–

direction. For detailed derivation of Lamb wave equations, readers are referred to ref. [10][18][21]. The Rayleigh-Lamb equation has been obtained as characteristic equation of the wavenumbers, i.e.,

$$\frac{\tan\eta_S d}{\tan\eta_P d}=\left[\frac{-4\eta_P\eta_S\xi^2}{\left(\xi^2-\eta_S^2\right)^2}\right]^{\pm 1} \qquad (2.19)$$

where +1 exponent corresponds to symmetric Lamb wave modes and -1 exponent corresponds to antisymmetric Lamb wave modes. d is the half plate thickness, and ξ is the frequency dependent wavenumber. η_P and η_S are given in Eq. (2.20). λ and μ are Lame's constants of the material, and ρ is the material density.

$$\eta_P^2=\frac{\omega^2}{c_p^2}-\xi^2;\quad \eta_S^2=\frac{\omega^2}{c_s^2}-\xi^2;\quad c_p=\sqrt{\frac{\lambda+2\mu}{\rho}};\quad c_s=\sqrt{\frac{\mu}{\rho}}; \qquad (2.20)$$

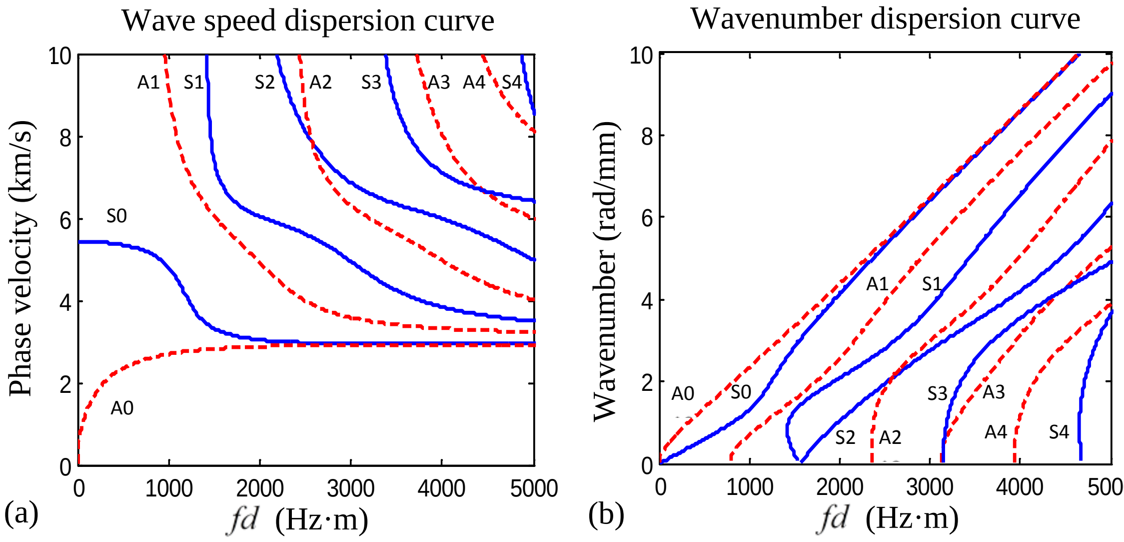

Figure 2.4: (a) Wave speed dispersion curve; (b) wavenumber dispersion curve [22]

Figure 2.4 shows the dispersion curves of aluminum plates calculated from the Rayleigh-Lamb equations. It can be noticed at least two wave modes (the fundamental symmetric mode: S0; the fundamental antisymmetric mode: A0) exist simultaneously. Beyond the corresponding cut-off frequencies, higher Lamb modes will participate in the propagation. At small frequency-thickness product values, the S0 mode is less dispersive than A0 mode, and all the Lamb wave modes converge to non-dispersive Rayleigh waves at large frequency-thickness product values. The dispersive and multi-mode nature of Lamb waves adds complexity in both Lamb wave propagation modeling and SHM application.

In their multi-modal and dispersive nature, Lamb waves also have complicated frequency dependent mode shapes associated with particle motion across the plate thickness. Even for certain Lamb modes, the mode shape changes under different frequencies. The displacement mode shapes can be calculated using Eq. (2.21) and Eq. (2.22)[18].

For symmetric Lamb modes:

$$\begin{aligned} u_x^S(x,y,t) &= iC^S\left[-2\xi^2\eta_S\cos\eta_S d\cos\eta_P y+\eta_S(\xi^2-\eta_S^2)\cos\eta_P d\cos\eta_S y\right]e^{i(\xi x-\omega t)} \\ u_y^S(x,y,t) &= C^S\left[2\xi\eta_P\eta_S\cos\eta_S d\sin\eta_P y+\xi(\xi^2-\eta_S^2)\cos\eta_P d\sin\eta_S y\right]e^{i(\xi x-\omega t)} \end{aligned} \tag{2.21}$$

For antisymmetric Lamb modes:

$$\begin{aligned} u_x^A(x,y,t) &= iC^A\left[2\xi^2\eta_S\sin\eta_S d\sin\eta_P y-\eta_S(\xi^2-\eta_S^2)\sin\eta_P d\sin\eta_S y\right]e^{i(\xi x-\omega t)} \\ u_y^A(x,y,t) &= C^A\left[2\xi\eta_P\eta_S\sin\eta_S d\cos\eta_P y+\xi(\xi^2-\eta_S^2)\sin\eta_P d\cos\eta_S y\right]e^{i(\xi x-\omega t)} \end{aligned} \tag{2.22}$$

where C^S and C^A determine the mode shape amplitudes; y is the location of interested point across the plate thickness; i is the imaginary unit; x is the coordinate along propagation direction.

Figure 2.5 shows the mode shapes of fundamental S0 and A0 Lamb waves in a 2-mm aluminum plate under various frequencies. It can be observed that for certain Lamb mode, the mode shapes vary a lot with frequency. Within low frequency range, the mode shapes show that S0 and A0 Lamb modes could be approximated by axial and flexural wave motion. However, within high frequency range, the mode shapes become more complicated and deviate from the axial-flexural approximation. And, at even higher frequency, e.g. at 10 MHz, the particle motions are mainly near the top and bottom surfaces of the plate, while the particles in the middle of the plate undergo very small oscillation. This shows that at high frequency range, Lamb modes converge to Rayleigh waves.

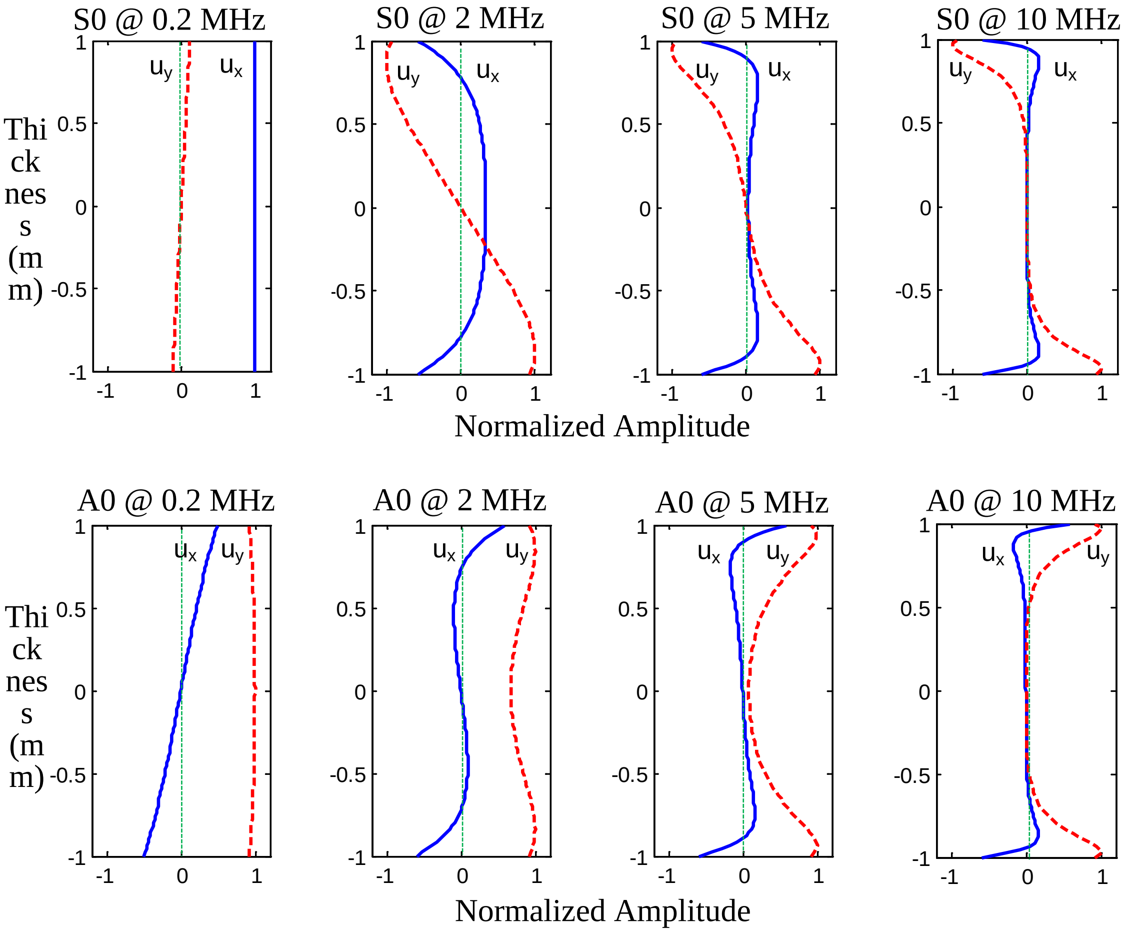

Figure 2.5: Mode shapes of S0 and A0 Lamb waves in a 2-mm thick aluminum plate[22]

2.2.4 Circular Crested Lamb Waves

In their practical applications, the interrogating Lamb waves generated by a transmitter will propagate out in a circular crested wave front instead of a straight crested wave front, because the transmitter can be considered as a point source compared with the large inspection area. With the wave propagating outward, this amount energy is distributed on a larger area. Thus, the amplitude of the interrogating wave is strong near the wave source and decays along the propagation direction. The circular crested Lamb wave solution can capture these effects due to outward propagation pattern.

A detailed and rigorous derivation of circular crested Lamb waves is well documented in[18]. The derivation of circular crested Lamb waves is found to be more appropriate in a cylindrical coordinate system shown in Figure 2.6a. The derivation arrives at the same Rayleigh-Lamb equation as Eq. (2.19), which means the circular crested Lamb waves propagate with the same wave speed as the straight crested Lamb waves.

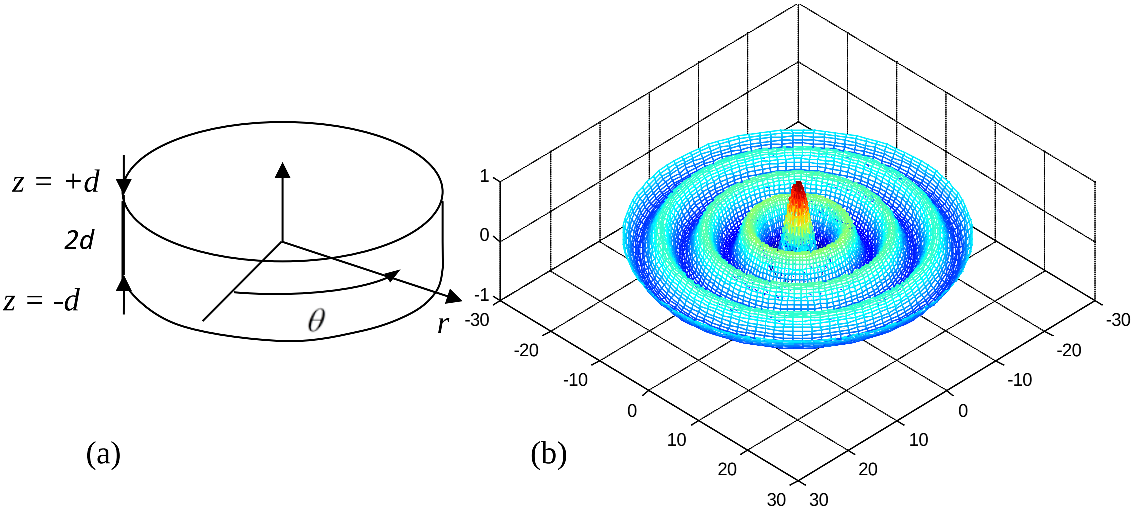

(a) (b)

Figure 2.6: (a) Cylindrical coordinate for problem derivation[18]; (b) circular crested wave pattern.

The propagation pattern of circular Lamb waves admits the Bessel and Hankel function family solution. The Bessel functions J_0 and J_1 is appropriate for standing waves, and the Hankel functions $H_0^{(1)}$ and $H_1^{(1)}$ are appropriate for propagating waves. The first kind Hankel functions ($H_0^{(1)}$ and $H_1^{(1)}$) describes an outward propagating wave field, when $e^{-i\omega t}$ is chosen as the convention for the derivation. While, the second kind Hankel functions ($H_0^{(2)}$ and $H_1^{(2)}$) describes an outward propagating wave field, when $e^{i\omega t}$ is chosen as the convention for the derivation. The mode shape solutions for the circular crested Lamb waves are given below for outward propagating wave fields.

Symmetric Lamb modes:

$$\begin{aligned} u_r^S(r,z,t) &= C^S\left[2\xi^2\zeta_S\cos\zeta_S d\cos\zeta_P z-\zeta_S\left(\xi^2-\zeta_S^2\right)\cos\zeta_P d\cos\zeta_S z\right]H_1^{(1)}(\xi r)\,e^{-i\omega t}\\ u_z^S(r,z,t) &= C^S\xi\left[2\zeta_P\zeta_S\cos\zeta_S d\sin\zeta_P z+\left(\xi^2-\zeta_S^2\right)\cos\zeta_P d\sin\zeta_S z\right]H_0^{(1)}(\xi r)e^{-i\omega t} \end{aligned} \tag{2.23}$$

Antisymmetric Lamb modes:

$$\begin{aligned} u_r^A(r,z,t) &= -C^A\zeta_S\left[2\xi^2\sin\zeta_S d\sin\zeta_P z-\left(\xi^2-\zeta_S^2\right)\sin\zeta_P d\sin\zeta_S z\right]H_1^{(1)}(\xi r)e^{-i\omega t}\\ u_z^A(r,z,t) &= C^A\xi\left[2\zeta_P\zeta_S\sin\zeta_S d\cos\zeta_P z+\left(\xi^2-\zeta_S^2\right)\sin\zeta_P d\cos\zeta_S z\right]H_0^{(1)}(\xi r)e^{-i\omega t} \end{aligned} \tag{2.24}$$

where C^S and C^A are the amplitude factor for symmetric mode and antisymmetric mode, and can be determined from the wave generation calculation. ζ_P,ζ_S are defined as

$$\zeta_P^2=\frac{\omega^2}{c_P^2}-\xi^2;\quad \zeta_S^2=\frac{\omega^2}{c_S^2}-\xi^2 \tag{2.25}$$

It can be observed from Eq. (2.23) and Eq. (2.24), that the in-plane radian direction motion accepts the solution of the first kind Hankel function of order one ($H_1^{(1)}$), while the out-of-plane direction motion accepts the solution of the first kind Hankel function of order zero($H_0^{(1)}$). Figure 2.6b shows a typical outward propagation wave pattern calculated using Hankel function $H_0^{(1)}$, describing an out-of-plane wave motion. It can be noticed that the wave amplitude at the wave source (coordinate center) is strong, and it decays as it propagates out. Figure 2.7 shows the plots of Hankel functions of order zero and order one. It can be noticed that the amplitude is high near the origin of R, and beyond certain distance, the amplitude becomes stable and changes more gradually compared with the origin range of R.

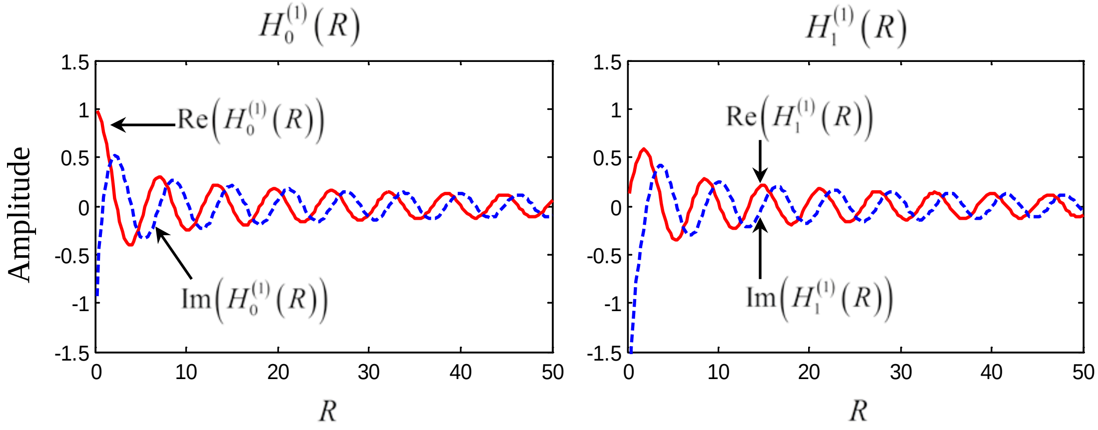

Figure 2.7: Hankel function of order zero ($H_0^{(1)}(R)$) and order one ($H_1^{(1)}(R)$).

Lamb wave field eradiating from a point source takes the following solution[18][23]:

$$u_r = \sum_{n=1}^{\infty} a_n(z) H_1^{(1)}(\xi_n r) e^{-i\omega t} \tag{2.26}$$

where u_r is the radial displacement, $a_n\left(z\right)$ is the thickness dependent modeshape of wave mode number n, and $H_1^{(1)}$ is the first kind Hankel function of order one.

2.2.5 CIRCULAR CRESTED SH WAVES

For circular crested SH waves axisymmetry ($\partial / \partial\theta \equiv 0$) applies. Shear horizontal (SH) waves irradiating from a point source can be derived starting from the governing equation under axisymmetric assumption.

$$\nabla^2 u_\theta - \frac{u_\theta}{r^2} = \frac{1}{c_S^2}\frac{\partial^2 u_\theta}{\partial t^2} \tag{2.27}$$

Where u_θ is the tangential displacement, c_S is the shear wavespeed.

In polar coordinate system, Eq. (2.27) becomes

$$\frac{\partial^2 u_\theta}{\partial r^2} + \frac{1}{r}\frac{\partial u_\theta}{\partial r} - \frac{u_\theta}{r^2} = \frac{1}{c_S^2}\frac{\partial^2 u_\theta}{\partial t^2} \tag{2.28}$$

Assuming a harmonic wave field

$$u_\theta = Ue^{-i\omega t}; \quad \frac{\partial^2 u_\theta}{\partial t^2} = -\omega^2 u_\theta \tag{2.29}$$

Substitution of Eq. (2.29) into Eq. (2.28) yields

$$\left(\xi^{SH} r\right)^2 \frac{\partial^2 u_\theta}{\partial\left(\xi^{SH} r\right)^2} + \left(\xi^{SH} r\right)\frac{\partial u_\theta}{\partial\left(\xi^{SH} r\right)} + \left((\xi^{SH} r)^2 - 1\right)u_\theta = 0 \tag{2.30}$$

where $\xi^{SH} = \omega / c_s$ is the wavenumber of SH waves. Letting $x = \xi^{SH} r$, $y = u_\theta$, and $\nu = 1$, Eq. (2.30) can be cast into the Bessel equation of order ν.

$$x^2 \frac{d^2 y}{dx^2} + x\frac{dy}{dx} + \left(x^2 - \nu^2\right)y = 0 \tag{2.31}$$

Eq. (2.30) can be immediately recognized as the Bessel equation of order one and accepts the following solution for outward propagating waves.

$$u_\theta = \sum_{n=1}^{\infty} b_n(z) H_1^{(1)}\left(\xi_n^{SH} r\right) e^{-i\omega t} \tag{2.32}$$

where $b_n(z)$ is the modeshape of the n^{th} SH mode, and $H_1^{(1)}$ is the first kind Hankel function of order one.

2.3 STRUCTURAL HEALTH MONITORING USING GUIDED WAVES

Structural Health Monitoring (SHM) is an area of growing multi-disciplinary field with wide applications. This technology evolves from the conventional nondestructive evaluation (NDE) and conditional based maintenance (CBM), where the damage detection and evaluation are done in a schedule based or conditional based manner. In contrast with NDE and CBM, SHM aims at developing real-time or on-demand damage detection and characterization systems for evaluation of structural health status. Within the scope of SHM, guided wave techniques are favorable for their capability of interrogating large areas of structure from a single location. In this section, fundamental SHM concepts are introduced, prevalent guided wave techniques are covered, and key points in guided wave based SHM are discussed.

2.3.1 STRUCTURAL HEALTH MONITORING CONCEPTS

General sensing technology can be cast into two methodological categories: (1) active sensing and (2) passive sensing. Active sensing procedure has three main advantages for SHM applications: (1) it allows the real-time and on-demand inspection of the structures; (2) the excitation can be optimized for the most sensitive and effective response for damage detection; (3) the active sensing procedure is repeatable, which allows the comparison between two independent interrogations (a baseline data and a current status data). Passive sensing systems only passively record events which happened during an interested period of time. By analyzing the recorded signal, diagnosis can be made on the health status of the structure. Examples of passive sensing SHM can be found in the acoustic emission (AE) monitoring and impact detection, where passive sensors are triggered by crack advancing or impact events. By analyzing the AE or impact signal, location of the AE or impact source can be identified. In contrast to passive sensing, active sensing methods interrogate the structures with defined excitations, and record the corresponding response. By analyzing the response, diagnosis can be made.

A schematic representation of a generic SHM system is shown in Figure 2.8. The active sensors clusters are implemented on the critical areas of high monitoring interest, such as airplane wines, engine turbines, fuselage, and fuel tank. Permanently bounded on the host structures, the sensors can actively interrogate large areas from local cluster zones in a real-time or on-demand manner, gathering sensing data to the data concentrators. These data concentrators will transmit the data to the SHM processing unit, where the data will be processed and diagnosis will be made.

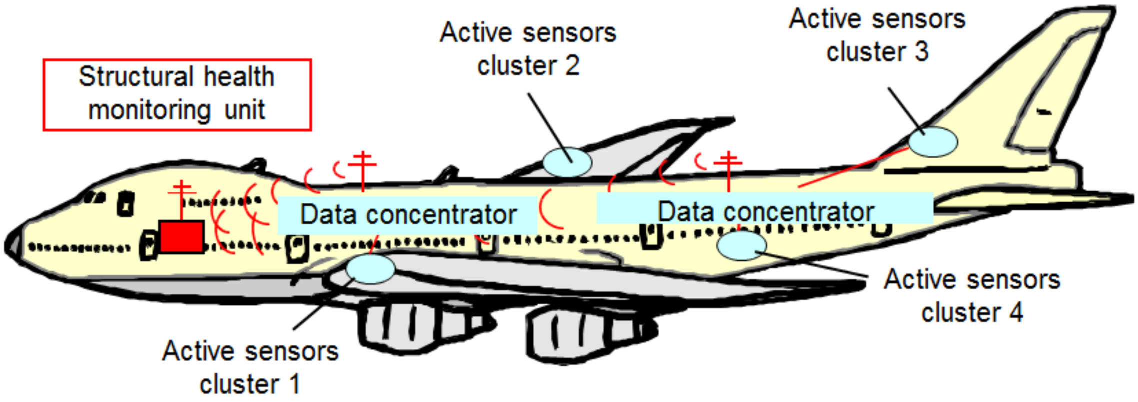

Figure 2.8: Schematic representation of a generic SHM system, consisting of active sensors, data concentrators, wireless communication, and SHM central unit[24].

2.3.2 Guided Wave Techniques

The guided wave techniques include pitch-catch, pulse-echo, electro-mechanical impedance spectroscopy (EMIS), phased array, and sparse array time-reversal imaging method. There are some nonlinear techniques as well that deal with the higher harmonic generation, subharmonic generation, and mixed frequency response [22].

The pitch-catch active sensing method in SHM is shown in Figure 2.9. One transducer (sensor 1) acts as the transmitter and radiates the guided waves, and another transducer acts as the receiver and pick up the sensing signal. In the pristine case (baseline), the interrogating waves are generated by the transmitter, propagate along the structure, and are picked up by the receiver. In the damaged case, the interrogating waves generated by the transmitter, propagate along the structure, interact with the damage, carry the damage information with them, and are finally picked up by the receiver. The subtraction between these two states reveals the damage scattering response, which may indicate the presence and severity of the damage.

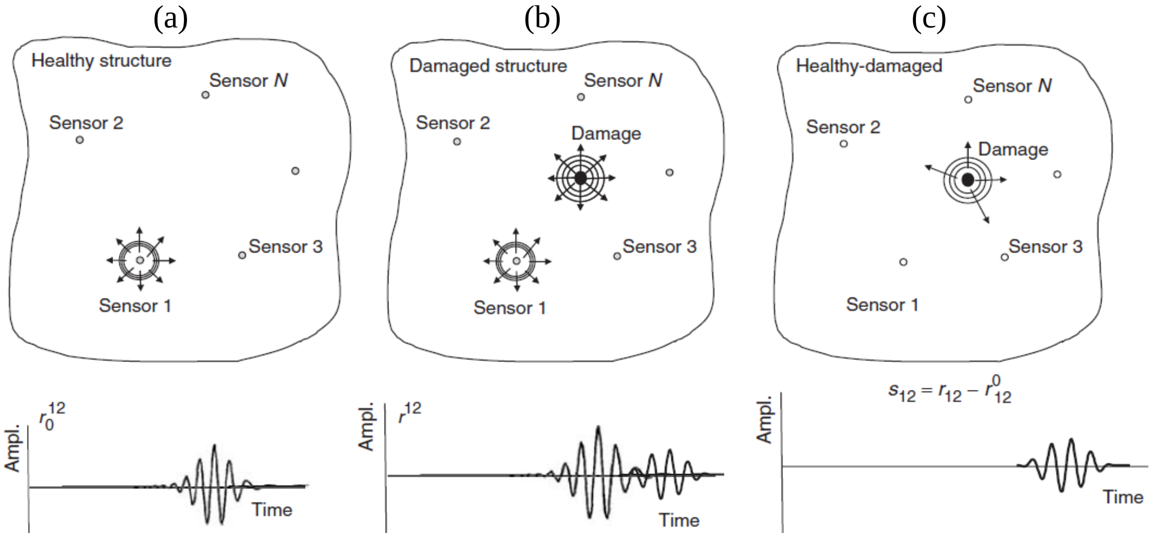

Figure 2.9: Pitch-catch active sensing: (a) baseline response; (b) response with damage; (c) scattered response [25]

Several sensors may work together in a systematically designed manner forming a sensor network and achieve more complicated diagnostic approaches. Advanced damage imaging techniques have been developed using phased array and sparse array. Giurgiutiu and Bao[26] investigated the embedded-ultrasonics structural radar (EUSR) for in situ monitoring of thin-wall structures. Figure 2.10a shows the 1-D phased array EUSR and its imaging result of a crack. Yu and Giurgiutiu [27] further extended the EUSR principle to 2-D phased array using 64 sensors. Wang et al.[28] proposed the synthetic time-reversal imaging method for structural health monitoring. Figure 2.10b shows the sparse array with four sensors and its imaging result using time-reversal method.

(a) Phased array (EUSR) (b) Sparse array (time-reversal)

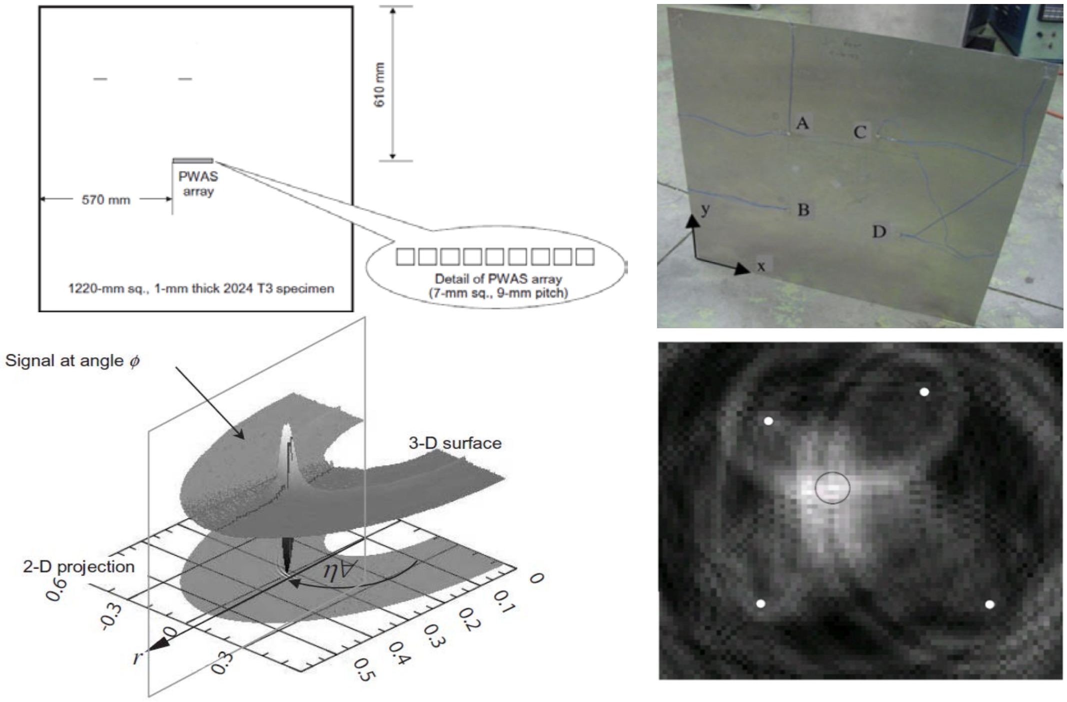

Figure 2.10: (a) Phased array imaging using EUSR [26]; (b) sparse array imaging using time-reversal method[28].

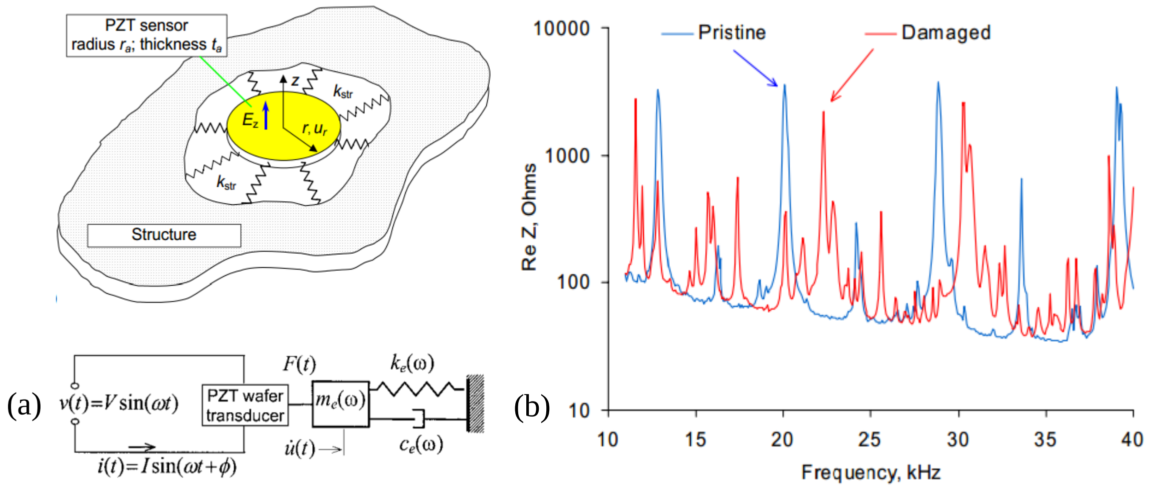

Figure 2.11: (a) Electro-mechanical coupling between the PZT active sensor and the structure[29]; (b) EMIS spectrum[30].

In addition to traveling wave techniques, the EMIS is a standing guided wave SHM method. The continuous harmonic excitation of a transducer will excite the structure with guided waves, which will be reflected by structural boundaries and damage, forming standing waves between the wave source and the reflectors. This standing wave formation will result in local mechanical resonance, which will be shown in the electrical response through the electro-mechanical coupling. Figure 2.11a shows the electro-mechanical coupling between the transducer and the structure. Figure 2.11b is a typical EMIS spectrum, showing that the damaged case spectrum deviates from the pristine case.

2.4 PIEZOELECTRIC WAFER ACTIVE SENSORS

Recently emerged piezoelectric wafer active sensors (PWAS) have the potential to improve the SHM technology significantly. PWAS are small, lightweight, inexpensive, and can be produced in different geometries. They are convenient enablers for generating and receiving guided waves. A PWAS mounted on the structure is shown in Figure 2.12.

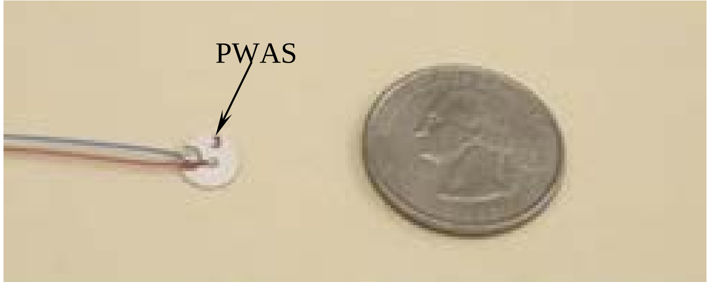

Figure 2.12: Piezoelectric wafer active sensors (PWAS).

They can be permanently bonded on host structures in large quantities and achieve real-time monitoring of the structural health status. They couple with the structure through in-plane motion and generate Lamb waves, which makes them suitable for inspection large areas of interest.

2.4.1 PWAS PRINCIPLES AND OPERATION MODES

Piezoelectric wafer active sensors (PWAS) couple the electrical and mechanical effects (mechanical strain, S_{ij}, mechanical stress, T_{kl}, electrical field, E_k, and electrical displacement, D_j). The piezoelectric constitutive equations in tensor notations can be written as

$$\begin{aligned} S_{ij} &= s^E_{ijkl} T_{kl} + d_{kij} E_k \\ D_j &= d_{klj} T_{kl} + \varepsilon^T_{jk} E_k \end{aligned} \tag{2.33}$$

where s^E_{ijkl} is the mechanical compliance of the material measured at zero electric field ($E = 0$), ε^T_{jk} is the dielectric permittivity measured at zero mechanical stress ($T = 0$), and d_{klj} represents the piezoelectric coupling effect. PWAS utilize the d_{31} coupling between in-plane strains, S_1, S_2 and transverse electric field E_3.

PWAS transducers can be used as both transmitters and receivers. Their modes of operation are shown Figure 2.13. PWAS can serve several purposes[18]: (a) high-bandwidth strain sensors; (b) high-bandwidth wave exciters and receivers; (c) resonators; (d) embedded modal sensors with the electromechanical (E/M) impedance method. By application types, PWAS transducers can be used for (i) active sensing of far-field damage using pulse-echo, pitch-catch, and phased-array methods, (ii) active sensing of near field damage using high-frequency E/M impedance method and thickness gage mode, and (iii) passive sensing of damage-generating events through detection of low-velocity impacts and acoustic emission at the tip of advancing cracks (Figure 2.13). The main advantage of PWAS over conventional ultrasonic probes is in their lightweight, low profile, and low cost. In spite of their small size, PWAS are able to replicate many of the functions performed by conventional ultrasonic probes.

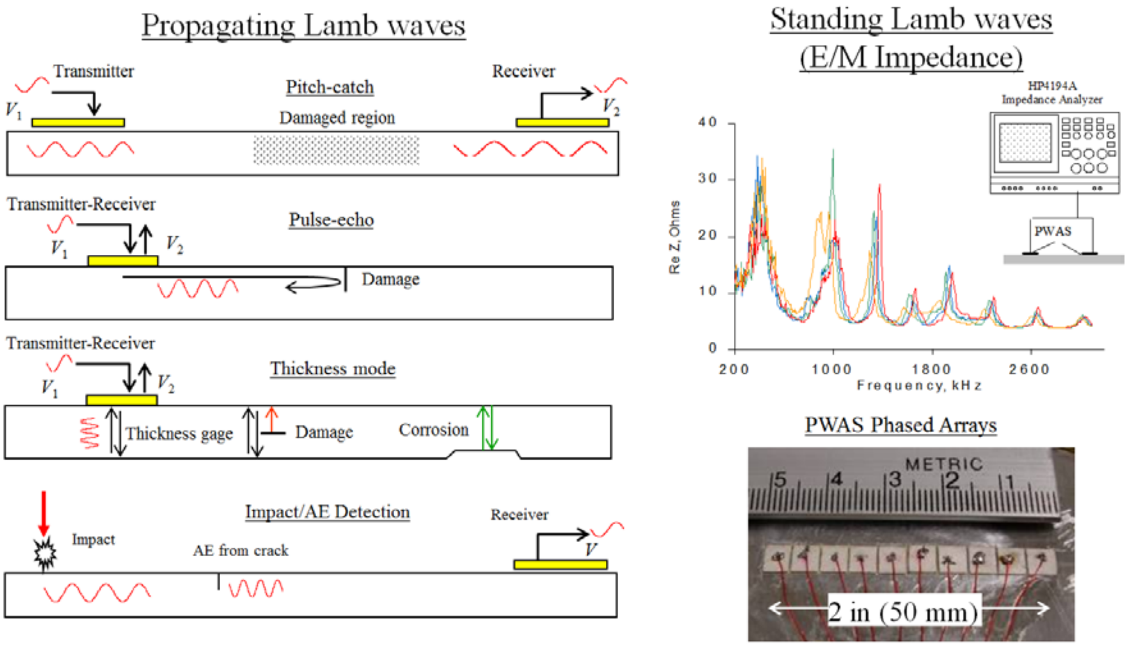

Figure 2.13: Schematic of PWAS application modes [18].

2.4.2 PWAS COUPLED GUIDED WAVES AND TUNING EFFECT

Figure 2.14 shows the coupling between PWAS and the host structure, and illustrates how PWAS transducers generate Lamb waves. When an oscillatory electric voltage at ultrasonic frequencies is applied on PWAS, due to the piezoelectric effect, a oscillatory strain is induced to the transducer. Since the structure constrains the motion of PWAS, the reacting force from the bonding layer will act as shear stress on the host structure and generate wave motion.

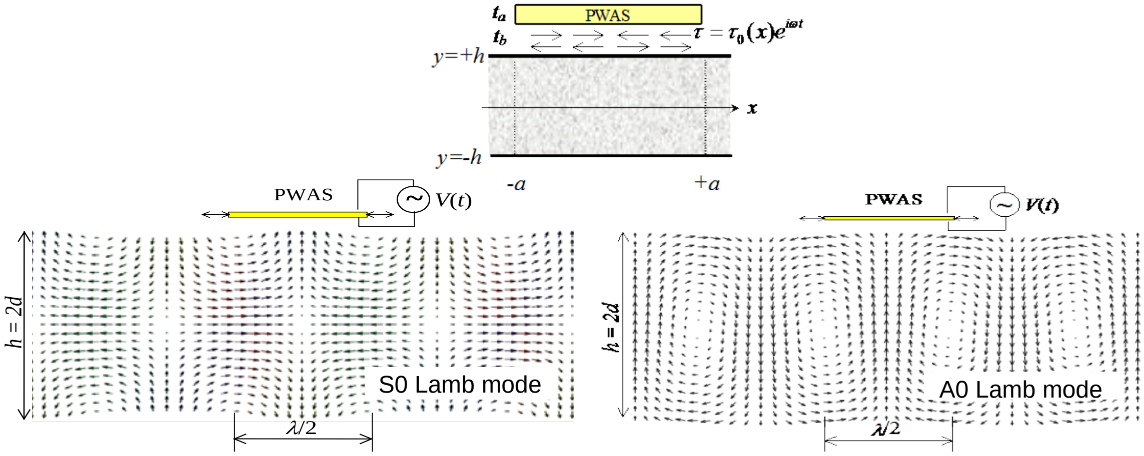

Figure 2.14: Lamb wave generation using PWAS transducers[18]

The Lamb wave amplitude excited by PWAS depends on the PWAS size, plate thickness, and excitation frequency. For a given PWAS and plate geometry, the amplitudes of Lamb modes changes with frequency. It was found that tuning possibility exists for generating single Lamb mode with PWAS transducers. The tuning effect is important because it overcomes the multimode difficulty for Lamb wave applications. The analytical expression on tuning effect was first developed by Giurgiutiu[31] as

$$\varepsilon_x\left(x,t\right) = -i\frac{a\tau_0}{\mu}\left\{\sum_{\xi^S}(\sin\xi^S a)\frac{N_S\left(\xi^S\right)}{D_S^{'}\left(\xi^S\right)}e^{-i\left(\xi^S x-\omega t\right)} + \sum_{\xi^A}(\sin\xi^A a)\frac{N_A\left(\xi^A\right)}{D_A^{'}\left(\xi^A\right)}e^{-i\left(\xi^A x-\omega t\right)}\right\} \quad (2.34)$$

Figure 2.15 shows the tuning curve for 7 mm PWAS and 1.6 mm thick aluminum plate situation. It is apparent that the amplitudes of S0 and A0 Lamb modes excited by the PWAS transducer change with frequency. Around 300 kHz, A0 Lamb mode reaches the rejecting point where no A0 mode Lamb wave will be excited. This is a sweet spot for generating only S0 wave mode for structural inspection.

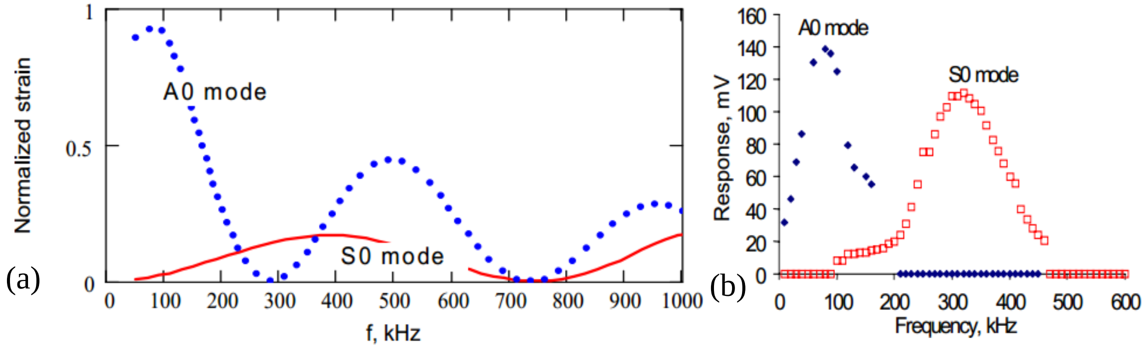

Figure 2.15: (a) Strain Lamb wave tuning results from analytical solution; (b) Experimental results from PWAS response[31].

CHAPTER 3

SCATTERING OF GUIDED WAVES FROM RIVET HOLE WITH BUTTERFLY CRACKS

Scattering of guided waves retain a central function in the development of structural health monitoring (SHM) systems. This study focuses on guided plate waves, i.e. Lamb waves, which are guided and propagate in thin wall structures. The modeling of Lamb waves is challenging, because Lamb waves propagate in structures with multi-mode dispersive characteristics. At a certain value of the plate thickness-frequency product, several Lamb modes may exist simultaneously, and their phase velocities vary with frequency [10][18]. When Lamb waves interact with damage, they will be transmitted, reflected, scattered and mode converted. This chapter presents the theory behind the guided wave scattering from the damage in the thin plate structures.

3.1 DESCRIPTION OF THE SHM OF MULTIPLE-RIVET-HOLE LAP JOINT

A multiple-rivet-hole lap joint with active transmitting-sensing sensors of an SHM system is illustrated in Figure 3.1. When electrical voltage is supplied to the piezoelectric transmitter (actuator), it generates mechanical excitation in the structure and produces Lamb waves that propagate in the structure. The Lamb waves interact with the damages that act as the secondary sources of guided waves. The scattered guided waves propagate in the structures and received by the piezoelectric sensor. Actuator dispatches Lamb waves to each of the rivet holes at a certain angle that can be calculated from the standoff distance (L) and pitch (P) of each rivet hole (Figure 3.1). The scattering phenomenon depends on the direction (θ) of incident Lamb waves as well as the azimuth direction (Φ) around the damage (the azimuth direction Φ corresponds to the sensor placement direction).

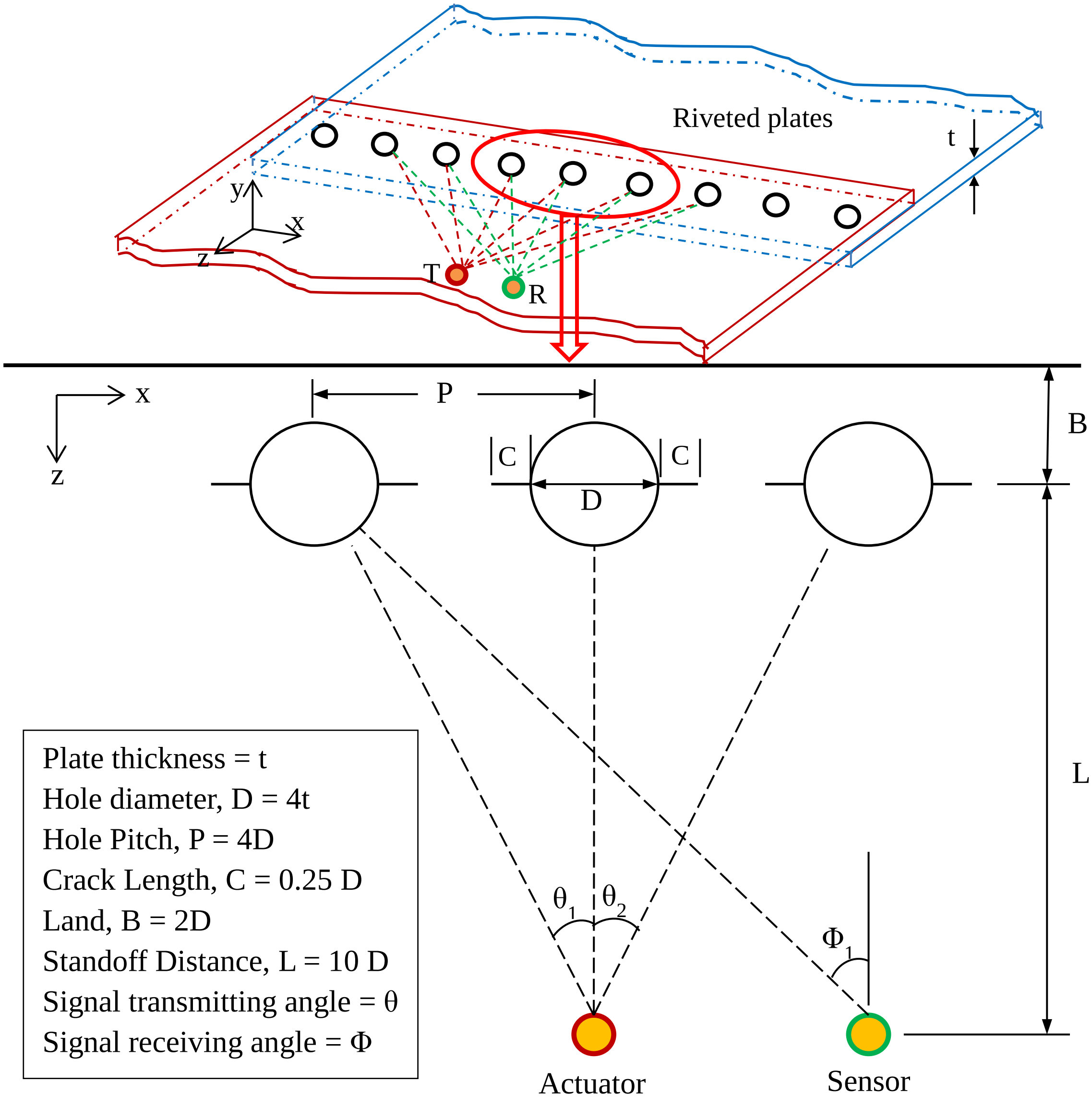

Figure 3.1: Illustration of the multiple-rivet-hole lap joint

The secondary source (cracked rivet hole) is asymmetric for a certain angle of incident Lamb waves, hence, it acts as a non-axisymmetric secondary source of scattered waves. The scattered waves contain scattered Lamb waves and SH waves Understanding the non-axisymmetric scattered waves around the damage provides the ability to better detect the emanating cracks in the rivet holes. The actuator and sensor installment as well as the excitation frequency depend on the non-axisymmetric behavior of the scattered guided waves. The design of proper transducer installation and selection of the center frequency of excitation enable capturing the better damage signature originating from the cracks of the rivet holes.

Since no closed form solution exists for the non-axisymmetric scattered waves, a combined analytical and finite element modeling has been introduced in the present study. Exact closed form analytical formulation has been used for the propagation of Lamb waves from the actuator up to the damage in the structure. The interaction of the Lamb waves with the local damage is modeled using finite element analysis and the non-axisymmetric behaviors of the scattered waves is captured through the wave damage interaction coefficients (WDICs) and scatter cubes. The concept of WDIC is discussed in Section 3.3.

3.2 INTERACTIONS OF LAMB WAVES FROM MULTIPLE DIRECTIONS

In order to solve the problem of multiple-rivet-hole splice joint, it is important to understand the scattering phenomenon of Lamb waves incident on the damage from multiple directions. Figure 3.2 shows that Lamb waves are incident on an arbitrary damage (rivet hole with cracks in the present study) from multiple directions. The incident direction of Lamb wave is denoted as θ. After hitting the damage the scattered waves are generated and directed azimuthally for each incident direction. The azimuth direction is denoted as Φ . The transmitter PWASs are located around the damage and transmitting signals from various directions that simulate the Lamb wave incident from multiple directions. The scattered coefficients for the scattered waves are to be recorded at different sensing angles (Φ) around the sensing boundary for each transmitting angle (θ). The scattered coefficient needs to be recorded for the frequencies of interest. The corresponding complex-valued WDICs can form a form a “scatter cube” as shown in Figure 3.2(b). The three dimensions of the “scatter cube” contain the WDICs for the variation of frequencies, angles of transmitting PWASs, and angles of sensors. These WDICs can describe complicated 3-D interaction between the interrogating waves and damage, i.e., scattering and mode conversion. Two scatter cubes are needed for analyzing the interaction of two Lamb wave modes (S0 and A0).

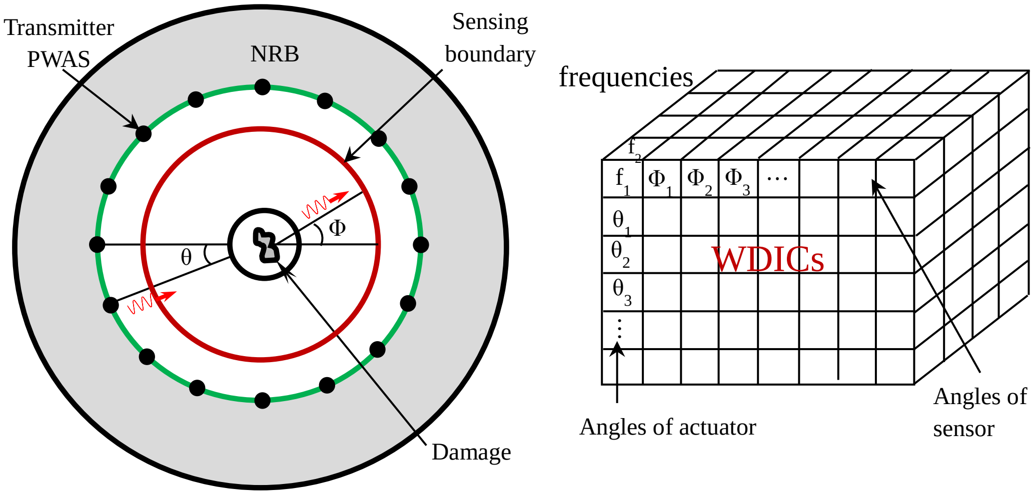

(a) (b)

Figure 3.2: (a) Azimuthally scattering of Lamb waves incident from multiple directions (b) “Scatter cube” of WDICs

The representation in Figure 3.2a gives the building block of analyzing the problem as shown in Figure 3.1. However, it does not consider the interactions of scattered waves among the adjacent rivet holes and with the edge of the riveted plates as shown in Figure 3.1. The incorporation of these two effects would invite more complexities in the scattered waveform. These two effects are not considered in the present study and would be focus of a future study.

3.3 CONCEPT OF WAVE DAMAGE INTERACTION COEFFICIENT (WDIC)

Several researchers have studied the interaction between guided waves and damage analytically using normal-mode expansion and boundary-condition matching [32][33][34]. Damage interaction coefficients were derived to quantify the guided-wave transmission, reflection, mode conversion, and scatter at the damage site. Due to their mathematical complexity, these analytical solutions are restricted to simple damage geometries: notches, holes, or partial through holes. Wave damage interaction coefficient (WDIC) may describe the 3D interactions of the incoming waves and the scattered waves. To clarify the idea of WDIC, let us consider an incoming wave of displacement field (u_{IN}) is striking an arbitrary damage at an incident angle θ as shown in Figure 3.3. The damage located at the center of the segment generate scattered waves are in multiple azimuth directions Φ. The scattered displacement fields (u_{SC}) are recorded at the sensing boundary located at radius r. The incident displacement field coming towards the center of the damage and the scattered displacement field recorded at the sensing boundary follows a certain relation [35], i.e.,

$$u_{IN}^{A} e^{-i\varphi_{IN}^{A}} C_{AB}\left(\omega,\theta,\Phi\right) e^{-i\varphi_{\mathrm{AB}}\left(\omega,\theta,\Phi\right)} H_{m}^{(1)}\left(\xi^{B} r\right) = u_{SC}^{B}\left(\omega,\theta,\Phi\right) e^{-i\varphi_{SC}^{B}\left(\omega,\theta,\Phi\right)} \tag{3.1}$$

where $u_{IN}^{\mathrm{A}} e^{-i\varphi_{IN}^{\mathrm{A}}}$ represents any incident mode A at the center of the damage; $C_{AB}\left(\omega,\theta,\Phi\right) e^{-i\varphi_{AB}\left(\omega,\theta,\Phi\right)}$ represents the amplitude $C_{AB}\left(\omega,\theta,\Phi\right)$ and phase $e^{-i\varphi_{AB}\left(\omega,\theta,\Phi\right)}$ of WDIC; r is the radius of sensing boundary; $H_{m}^{(1)}\left(\xi^{B} r\right)$ is the Hankel function of 2-D scattered wave field (B) propagates in outward direction with m = 1. C_{AB} stands for the incident A wave mode to the scattered B wave mode that depends on the direction of incident Lamb wave, azimuthal direction of the damage and the circular frequency. On the right side $u_{SC}^{B}(\omega,\theta,\Phi)e^{-i\varphi_{SC}^{B}(\omega,\theta,\Phi)}$ represents the scattered displacement field along the sensing boundary of radius r .

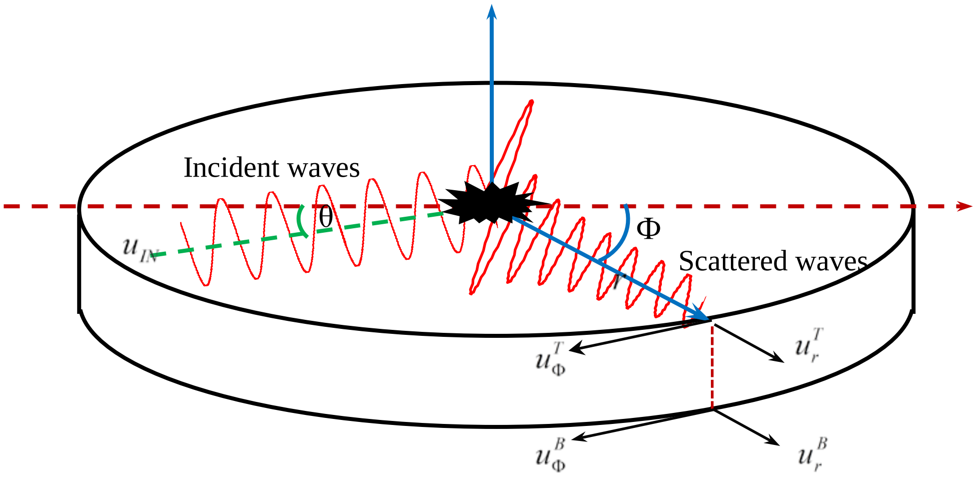

Figure 3.3: Extraction of WDIC from a damaged segment

Upon rearrangement Equation (14) yields

$$C_{AB}(\omega,\theta,\Phi)e^{-i\varphi_{AB}(\omega,\theta,\Phi)}=\frac{u_{SC}^{B}(\omega,\theta,\Phi)}{u_{IN}^{A}}\frac{1}{H_{m}^{(1)}(\xi^{B}r)}e^{-i\Delta\varphi_{AB}(\omega,\theta,\Phi)} \tag{3.2}$$

where, $\Delta\varphi_{AB}(\omega,\theta,\Phi)=\varphi_{SC}^{B}(\omega,\theta,\Phi)-\varphi_{IN}^{A}$. From Equation (15) the amplitude and phase may be separated as

$$C_{AB}(\omega,\theta,\Phi)=\left|\frac{u_{SC}^{B}(\omega,\theta,\Phi)}{u_{IN}^{A}}\frac{1}{H_{m}^{(1)}(\xi^{B}r)}\right| \tag{3.3}$$

$$\varphi_{AB}(\omega,\theta,\Phi)=\Delta\varphi_{AB}(\omega,\theta,\Phi)-\left[\angle\frac{1}{H_{m}^{(1)}(\xi^{B}r)}-\angle\frac{1}{H_{m}^{(1)}(0^{+})}\right] \tag{3.4}$$

For instance, when incident symmetric Lamb wave mode (*S*0 mode) causes scattered *S*0 mode then both *A* and *B* corresponds to the parameters of *S*0 mode. When incident *S*0 mode causes scattered symmetric *SH* mode then *A* corresponds to the parameters of *S*0 mode but *B* corresponds to the *SH* wave mode. Similarly when incident *A*0 mode causes scattered symmetric *A0* mode then *A* corresponds to the parameters of *A*0 mode and *B* corresponds to the *A0* wave mode.

3.4 SEPARATION OF SCATTTERED WAVE MODES

The wave fields of the local damage model can be solved using finite element method (The detail will be discussed in Chapter 4) and the displacement wave fields can be obtained throughout the local damage model. To identify the scattered wave modes two sensing boundaries can be used: one on the top surface of the plate and the other on the bottom surface of the plate. The sensing boundary located on the top surface of the plate gives the radial and tangential displacement components at each sensing node denoted as u_r^T and u_θ^T. The sensing boundary located on the bottom surface of the plate gives the radial and tangential displacement components at each sensing node denoted as u_r^B and u_θ^B The radial and tangential displacement components of the top and bottom sensing nodes are used to selectively separate each wave mode, as follows:

$$u_{SC}^{S0} = \frac{u_r^T + u_r^B}{2}; \quad u_{SC}^{A0} = \frac{u_r^T - u_r^B}{2}; \quad u_{SC}^{SH_{S0}} = \frac{u_\theta^T + u_\theta^B}{2}; \; u_{SC}^{SH_{A0}} = \frac{u_\theta^T - u_\theta^B}{2} \tag{3.5}$$

It should be clearly noted that in this study we focused on the fundamental Lamb wave modes (S0 and A0) and fundamental shear horizontal mode (SH0). The frequency range of our analysis is below the cut off frequencies of the higher Lamb and SH wave modes. We denote fundamental SH_{S0} mode as SH mode. The extension of our approach to higher modes will be done in a future study.

3.5 ANALYTICAL DERIVATION OF WDIC FOR A SIMPLE CASE

In this section we explain a simple case for better understanding of the concept of WDIC. We choose a simple pristine plate (Figure 3.4) to demonstrate the analytical WDIC. For the pristine plate it may be possible to derive the analytical expression of the WDIC.

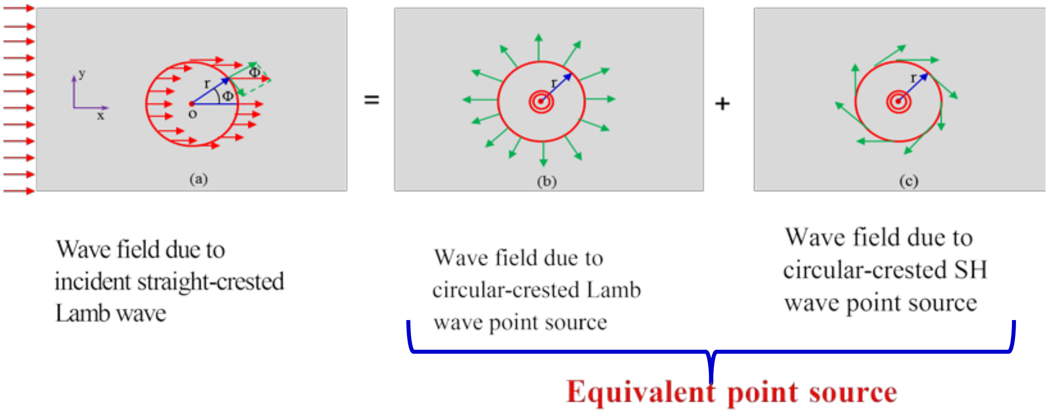

Figure 3.4: Equivalent source of a straight-crested Lamb wave

Let us consider a plane wave front Lamb waves travel in the $+x$ direction in an infinite plate. It generates a uniform wave field all over the pristine plate. At any sensing circle (red) of radius r, the wave fields are shown in Figure 3.4a that can be replaced by an equivalent source in Figure 3.4b,c. The equivalent source (ES) can be considered as the superposition of the two circular crested Lamb and SH wave point sources located at origin O. The circular crested Lamb wave takes care of the radial component of the wave field as shown in Figure 3.4b and the circular crested SH wave takes care of the tangential component of the wave field as shown in Figure 3.4c. Thus we may write,

$$\psi_{StarightLW} = \psi_{CircularLW} + \psi_{CircularSH} \tag{3.6}$$

3.5.1 ANALYTICAL DERIVATION OF WDIC

Let us consider the displacement field $\vec{u}_i$ as incident wave field for the straight-crested Lamb wave. Thus, $\vec{u}_i$ can be written as

$$\vec{u}_i = \begin{bmatrix} u_x^{IN} \\ 0 \\ u_z^{IN} \end{bmatrix} \text{(Cartesian coordinates)} \tag{3.7}$$

$$\vec{u}_i = \begin{bmatrix} u_x^{IN}\cos(\Phi) \\ -u_x^{IN}\sin(\Phi) \\ u_z^{IN} \end{bmatrix} \text{(cylindrical coordinates)} \tag{3.8}$$

The displacement field $\vec{u}_{ES}$ of the equivalent source placed at the origin O equalize the incident displacement field $\vec{u}_i$, i.e.,

$$\vec{u}_i = \vec{u}_{ES} \tag{3.9}$$

The equivalent displacement is the vector sum of Lamb and SH wave displacements as

$$\vec{u}_{ES} = \vec{u}_{ES}^{LW} + \vec{u}_{ES}^{SH} \tag{3.10}$$

The Lamb wave displacement field has components in the radial and thickness direction only whereas the SH wave displacement field has component in the tangential direction only, i.e.,

$$\vec{u}_{ES}^{LW} = \begin{bmatrix} u_r^{ES} H_1^{(1)}(\xi_{LW} r) \\ 0 \\ u_z^{IN} \end{bmatrix}; \quad \vec{u}_{ES}^{SH} = \begin{bmatrix} 0 \\ u_\Phi^{ES} H_1^{(1)}(\xi_{SH} r) \\ 0 \end{bmatrix} \tag{3.11}$$

where, u_r^{ES} and u_Φ^{ES} represent the amplitude of the circular crested Lamb and SH wave displacement fields; $H_1^{(1)}$ is the first kind first order Hankel function.

Substituting Eq. (3.11) into Eq. (3.10) yields

$$\vec{u}_{ES} = \begin{bmatrix} u_r^{ES} H_1^{(1)}(\xi_{LW} r) \\ u_\Phi^{ES} H_1^{(1)}(\xi_{SH} r) \\ u_z^{IN} \end{bmatrix} \tag{3.12}$$

Substituting Eq.(3.8) and Eq. (3.12) into Eq.(3.9), then comparing the components yields

$$u_r^{ES} H_1^{(1)}(\xi_{LW}.r) = u_x^{IN} \cos(\Phi) \tag{3.13}$$

$$u_\Phi^{ES} H_1^{(1)}(\xi_{SH}.r) = -u_x^{IN} \sin(\Phi) \tag{3.14}$$

Normalizing Eq.(3.13) and Eq.(3.14) by the incident displacement (u_x^{IN}) and taking magnitude, WDICs of the Lamb and SH waves can be obtained as

$$WDIC_{LW} = \left| C_{LW} \cos\Phi \right| \tag{3.15}$$

$$WDIC_{SH} = \left| C_{SH} \sin\Phi \right| \tag{3.16}$$

where, $C_{LW} = 1 \big/ H_1^{(1)}(\xi_{LW}.r)$ and $C_{SH} = 1 \big/ H_1^{(1)}(\xi_{SH}.r)$ depend on frequency dependent wave number ξ and sensing circle radius r. Hence, the expressions of the WDICs are much simpler for the pristine plate. For a certain frequency and sensing circle, the magnitude of WDICs of Lamb wave and SH wave depend on the azimuth direction Φ, i.e.,

$$WDIC_{LW} \propto \left| \cos\Phi \right| \tag{3.17}$$

$$WDIC_{SH} \propto \left| \sin\Phi \right| \tag{3.18}$$

The polar plot of the WDICs can be shown in Figure 3.5. Both of them have the ideal double circle shape. The WDIC for the Lamb wave is a horizontal double circle that indicates that the Lamb wave energy is mostly directed to the forward and backward azimuth directions. The WDIC for the SH wave is a vertical double circle that indicates that the SH wave energy is mostly directed to the upward and downward azimuth directions. It can be noted that both of the WDIC profiles are symmetric about the horizontal and vertical lines drawn though the origin.

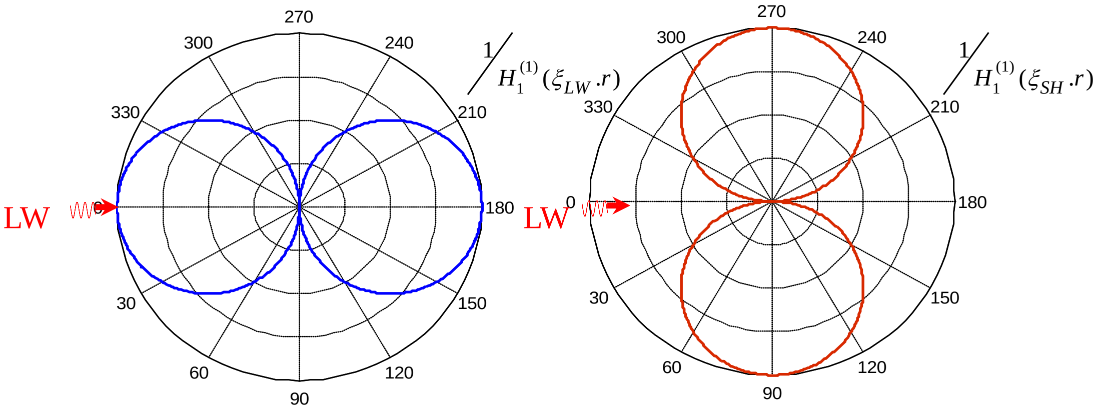

(a) (b)

Figure 3.5: Polar plot of analytically derived (a) WDIC$_{LW\_LW}$ (b) WDIC$_{LW\_SH}$

3.5.2 COMPARISON BETWEEN ANALYTICAL AND FEM RESULT

When the Lamb wave incident at $\theta = 9°$ to the horizontal line (Figure 3.6), the double-circle $WDIC_{S0\_S0}$ and $WDIC_{S0\_SH0}$ also tilted by the same amount of inclination. The ideal shapes maintain symmetry about the incident line and its perpendicular line drawn through the origin. The polar plot of the analytically derived WDIC profiles overlap the WDIC profiles from the FEM as shown in Figure 3.6 for both Lamb wave and SH wave. Hence, the analytical and FEM results follow a very good agreement.

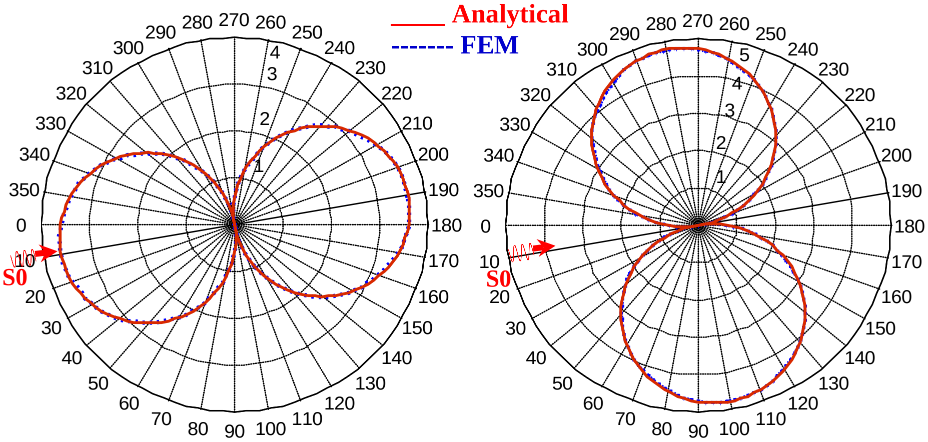

(a) (b)

Figure 3.6: analytical and FEM comparison of (a) WDIC$_{LW\_LW}$ (b) WDIC$_{LW\_SH}$, ($LW \to S0,\ \theta = 9^\circ,\ f = 486\ \text{kHz}$)

CHAPTER 4

LOCAL FINITE ELEMENT SIMULATION

This chapter presents the Finite Element analysis of the local damage for efficient simulation of guided Lamb wave propagation and interaction with damage. The development of computation models for Lamb wave propagation and interaction with damage is of great importance for both Structural Health Monitoring (SHM) system design and signal interpretation. Effective design of SHM systems requires the exploration of a wide range of parameters (frequency of excitation, sensor-damage relative locations, actuator position, transducer size, interrogating wave characteristics, etc.) to achieve the best detection and quantification of certain types of damage. On the other hand, active sensing signals using Lamb waves are usually difficult to interpret due to the multi-mode, dispersive nature of Lamb waves, and their interaction with damage, which involves complicated scattering and mode conversion phenomena. The advantage of numerical methods is that they can simulate wave damage interaction phenomena in very complicated structures; however, these methods usually require the discretization of the analyzed domain and the frequency/time marching procedure.

4.1 STATE OF THE ART

SHM techniques are increasingly being used for the damage detection and characterization in the aerospace structures[36][37][38]. The scattering of Lamb wave from the various types of damages were analyzed by many researchers[39][40][33][41].

Norris et al.[32] studied scattering of flexural waves on thin plates and used optical theorem to obtain far field scattering from a circular hole. They showed the azimuthal variation of the scattered flexural wave amplitude. A statistical approach to optimal sensor placement for SHM had been studied by Eric et al.[42] and their approach in the active sensing methods to three different types of plates had been demostrated. Bayes risk minimization implemented through the genetic algorithm (GA) had been used to find out the optimal arrangement of the transducers[43] The statistical model parameters were determined experimentally to avoid the difficulty in modeling the mechanical behavoiur of the individual transducers. However, artificial surface damages were generated at different locations of the plate to implement their statistical approach. Paul Fromme et al. [44] used analytical-Finite difference method (FDM) simulation to obtain the scattered field around the cracks at rivet holes and presented results at two different center frequencies for excitation and compared with the experimental results. Lamb waves propagating in an infinite plate containing a circular hole, with or without edge cracks, were investigated by Chang and Mal [25] using a hybrid method called the global local FEM. However, the research work was limited to the symmetric Lamb modes and the incident Lamb wave mode was perpendicular to the crack. Recent researches have put emphasis on the simulated results using fast and efficient numerical techniques to understand the Lamb wave behaviour prior to implementation of the results in the physical structures[34]. Recently, semi-analytical method and small-size numerical methods, such as semi-analytical finite element (SAFE) method and distributed point source method (DPSM) have been developed to make the computation load manageable[45]–[47]. The SAFE method has been used to combine with local finite element models to simulate wave interaction with damage in 1-D wave propagation problems, but 2-D wave propagation models have not been achieved. For DPSM method, 1-D wave propagation and mode conversion at damage have been reported. 2-D wave propagation interaction with through thickness damage has been simulated, but 2-D wave interaction with rivet hole with butterfly cracks and Lamb wave directionality effect has not been reported using DPSM. Yunju et al.[48] used a hybrid global matrix/local interaction simulation approach for modeling wave propagation in composites. The formulation uses a finite difference technique and requires time marching procedure. Numerical methodes are becoming a popular tool for understanding the complex Lamb wave interaction with complicated boundary conditions[49][50]. The scatter field of a single rivet hole cracks with single directed (incident) Lamb wave has been described introducing the wave damage interaction coefficient(WDIC) and the non-reflective boundary (NRB) was implemented to the simulate the infinite plate in a successful manner[51].

In the present study the interaction of Lamb waves with the cracked rivet hole from multiple directions is considered. Both symmetric and antisymmetric Lamb wave modes are incident from multiple directions and scattered coefficients are calculated around the damage corresponding to each incident direction. The 3D local damage is modeled and analyzed using finite element package (ANSYS15) while the Lamb wave generation, propagation, damage interaction insertion and detection are modeled using the exact analytical expressions. This chapter dedicates to the description of the local FEM modeling and results.

4.2 DESCRIPTION OF THE FEM MODELING

Considering the long standoff distance in the multiple-rivet-hole i.e. the excitation source (T-PWAS) is far away from the damage (rivet hole with butterfly cracks) as shown in Figure 4.1. The actuator (T-PWAS) is dispatching circular crested Lamb waves toward the damage. At large distances from the actuator, the behavior of circular-crested Lamb waves approaches asymptotically that of straight-crested Lamb waves, but the amplitude is affected by the factor which captures the geometric spreading of the circular wave front[18]. Considering the long standoff distance in the multiple-rivet-hole, thus, it's a good approximation to use straight crested Lamb modes as incident waves in the small local damage region during the nodal load calculations of FEM.

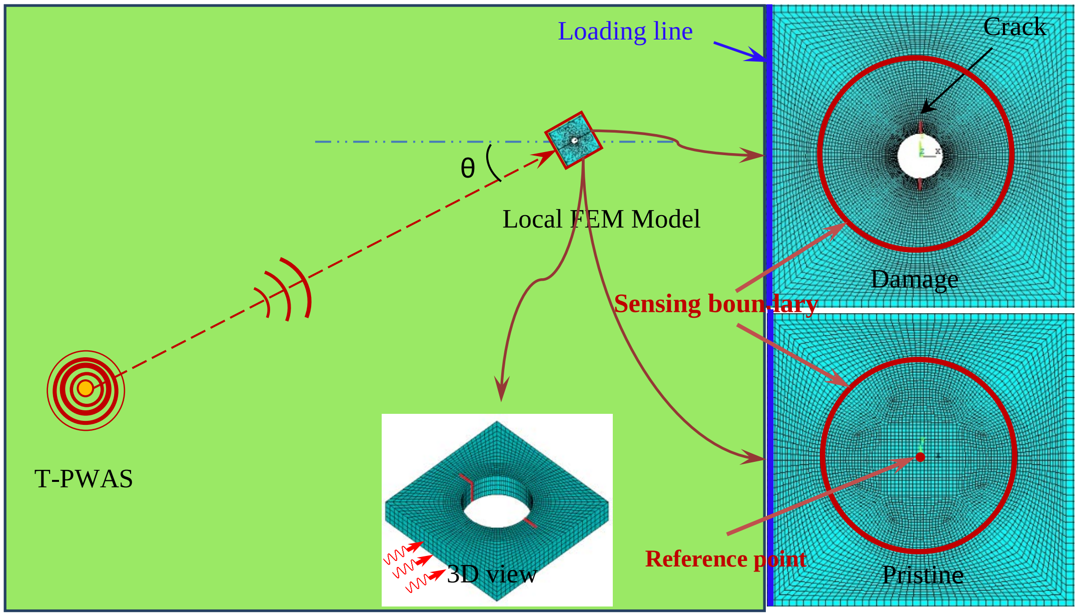

Figure 4.1: Small-size local damage in a large structure

4.2.5 MODEL GEOMETRY

A 3D local damage in the plate is modeled for the finite element analysis as shown in Figure 4.2. The dimension of the top view of the model is 40 mm x 40 mm with 1.6 mm thickness. A non-reflective boundary (NRB) of 20 mm wide at each side of the model is used. The crack length ($2a$) to diameter (d) of the hole ratio of 0.5 is used. For example, when the rivet hole diameter is 6.4 mm then the crack length is 1.6 mm on each side of the hole. The crack length to diameter ratio is kept low (0.5) so that it remains in the crack initiation stage of the crack growth during fatigue loading. The plate material is an aircraft grade aluminum-2024-T3. The density and poison's ratio of the plate material is 2700 kg/m^3 and 0.33 respectively.

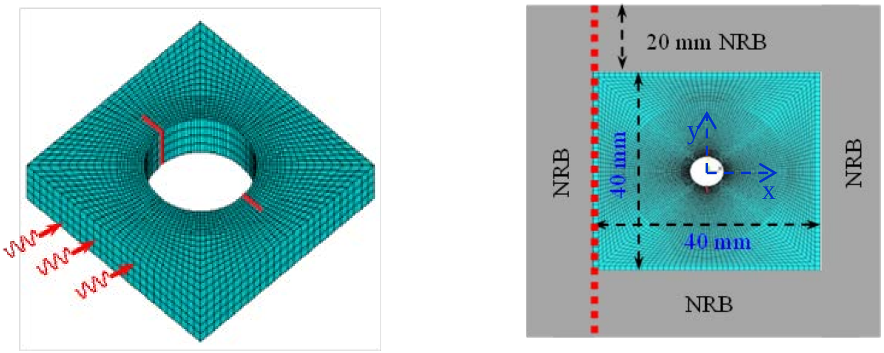

(a) 3D local damage model

(b) Top view of the model with NRB

Figure 4.2: Geometric information of the local damage model

4.2.6 MODELING OF THE CRACKS OF THE RIVET HOLE

Cracks in the rivet hole are modeled using the discontinuity at the adjacent pair of nodes along the cracks. Through thickness crack of crack length to diameter ratio of 0.5 is modeled. Hence, there are two crack faces along a crack in the rivet hole. In modeling, there are two sets of nodes along the crack faces and each set is representing the nodes on each face and the nodes are discontinuous along the crack faces. Two sets of nodes are adjacent to each other unlike the modeling of notch where there is a small gap between those sets of nodes. Like the nodes, the solid elements are also disbanded along the crack faces. The modeling of the cracks in finite element using the above approach is fair enough to model the actual cracks of rivet holes in the plate like structure [52].

4.2.7 MESHING OF THE MODEL

Eight node structural elements (SOLID45) are used to mesh the plate in a mapped meshing of “O” topology. The spring-damper elements (COMBIN14) are used to construct the NRB around the local model. In the thickness direction 0.4 mm mesh size is used which is fair enough to capture the thickness modeshapes. The scattered waves propagates in-plane directions (local x, y directions as shown in Figure 4.2b) and thus more denser mesh is required to capture the information in the in-plane directions. At least twenty elements per wavelength ($\lambda / l_e \geq 20$) are used to capture the detail of the propagating scattered waves. Finer meshing is used in the crack region to accommodate the high stress gradient and coarser meshing is used away from the crack and outside the sensing boundary.

4.2.8 IMPOSING THE NODAL POINT LOAD

The 3D view of the local FEM model is shown in Figure 4.3a. Incoming Lamb waves are shown as three red signal signs on one face of the model. Lamb mode excitation is imposed through nodal forces by evaluating integrals of stress mode shape components on the loading nodes. The stress mode shapes are calculated analytically [18] and converted into nodal forces through boundary integration on each element along the loading line. The element nodal force can be evaluated by using Eq.(4.1) [53].

$$F_{ix}^e = \int_0^{L_e} \sigma_{xx}^e(s) N_i^e(s)\, ds; \quad F_{iy}^e = \int_0^{L_e} \sigma_{xy}^e(s) N_i^e(s)\, ds \tag{4.1}$$

where subscript and superscript e stands for element, L_e represents the element size, F_{ix}^e and F_{iy}^e are nodal forces in x and y direction, i is the element node number, $N_i^e\left(s\right)$ is the shape function of selected element type, σ_{xx}^e and σ_{xy}^e are the normal and shear stresses respectively. In this study, SOLID45 3D eight-node structural elements are used, which utilize linear shape function $N_i^e\left(x,y,z\right)$. Along the thickness direction, it becomes $N_i^e\left(s\right)$, which is 1-D interpolation function along the line.

$$N_1^e\left(s\right)=1-\frac{s}{L_{element}};\quad N_2^e\left(s\right)=\frac{s}{L_{element}} \tag{4.2}$$

An assembly process enables to obtain the global nodal forces after all the nodal forces are obtained. The nodal forces are updated for each calculation step, imposing Lamb mode excitation for each excitation frequency. The stress modeshapes and loading line along a single line on that face is shown in Figure 4.3b. The Lamb wave modeshapes depend on the frequency of excitation. The stress modeshapes of S0 and A0 Lamb wave corresponding to a frequency of 250 kHz is shown in Figure 4.3c,d. The stress modeshapes for symmetric and antisymmetric Lamb wave are given by the equations Eqs.(4.3)-(4.4)

For symmetric modes:

$$\begin{aligned}
\sigma_{xx}^S(x,y,t) &= C^S\,2\mu\xi\eta_S\left[\left(\xi^2+\eta_S^2-2\eta_P^2\right)\cos\eta_S d\,\cos\eta_P y-(\xi^2-\eta_S^2)\cos\eta_P d\,\cos\eta_S y\right]e^{i\left(\xi x-\omega t\right)}\\
\sigma_{yy}^S(x,y,t) &= -C^S\,2\mu\xi\eta_S\left(\xi^2-\eta_S^2\right)\left(\cos\eta_S d\,\cos\eta_P y-\cos\eta_P d\,\cos\eta_S y\right)e^{i\left(\xi x-\omega t\right)}\\
\sigma_{xy}^S(x,y,t) &= iC^S\mu\left[4\xi^2\eta_P\eta_S\cos\eta_S d\,\sin\eta_P y+\left(\xi^2-\eta_S^2\right)^2\cos\eta_P d\,\sin\eta_S y\right]e^{i\left(\xi x-\omega t\right)}
\end{aligned} \tag{4.3}$$

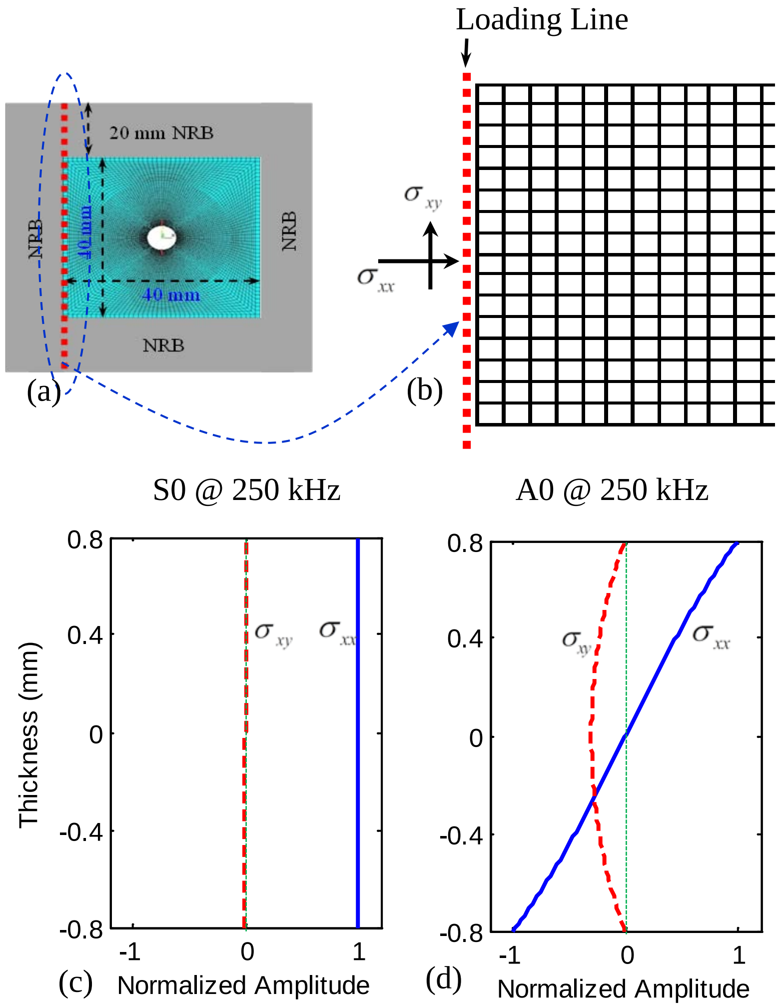

Figure 4.3: Imposing nodal forces and the stress modeshapes of incident Lamb waves

For antisymmetric modes:

$$\begin{aligned}
\sigma_{xx}^{A}(x,y,t) &= -C^{A}2\mu\xi\eta_{S}\left[\left(\xi^{2}+\eta_{S}^{2}-2\eta_{P}^{2}\right)\sin\eta_{S}d\sin\eta_{P}y-(\xi^{2}-\eta_{S}^{2})\sin\eta_{P}d\sin\eta_{S}y\right]e^{i(\xi x-\omega t)}\\
\sigma_{yy}^{A}(x,y,t) &= C^{A}2\mu\xi\eta_{S}\left(\xi^{2}-\eta_{S}^{2}\right)\left(\sin\eta_{S}d\sin\eta_{P}y-\sin\eta_{P}d\sin\eta_{S}y\right)e^{i(\xi x-\omega t)}\\
\sigma_{xy}^{A}(x,y,t) &= iC^{A}\mu\left[4\xi^{2}\eta_{P}\eta_{S}\sin\eta_{S}d\cos\eta_{P}y+\left(\xi^{2}-\eta_{S}^{2}\right)^{2}\sin\eta_{P}d\cos\eta_{S}y\right]e^{i(\xi x-\omega t)}
\end{aligned} \tag{4.4}$$

4.2.9 Imposing NRB around the Model

Non-reflective boundaries (NRB) can eliminate reflections from the edge of the plates, and thus allow for simulation of wave propagation in infinite medium with small-size models. In commercial FEM codes, such as ANSYS LS-DYNA solver with NRB option and ABAQUS using “solid infinite elements”, non-reflective viscous boundary condition has been realized by matching reacting forces at the defined NRB. Lysmer et. al [54] found that the matching normal and shear stresses should satisfy

$$\sigma = \rho c_P \frac{\partial u}{\partial t} \tag{4.5}$$

$$\tau = \rho c_S \frac{\partial v}{\partial t} \tag{4.6}$$

where the reacting stresses on the artificial boundary depends on the normal and tangential velocities $\frac{\partial u}{\partial t}$ and $\frac{\partial v}{\partial t}$. COMBIN14 spring-damper elements have been used to construct a viscoelastic boundary condition for wave propagation problems in seismic engineering, and a viscous boundary condition for wave propagation in honeycomb plates[55]–[57]. This NRB works well for bulk waves, and in the case of plate guided Lamb waves, it works well for S0 mode, but noticeable reflections occur when A0 mode interacts with the NRB.

Shen et al.[51] improved the NRB, making it effective for both symmetric and antisymmetric Lamb modes, in 3D FEM using COMBIN14 spring-damper elements. Figure 4.4a shows the schematic of COMBIN14 in ANSYS, and Figure 4.4b illustrates the method of constructing NRB in a 3D FEM mesh, where each node is connected with three COMBIN14 elements in three directions: one normal direction, and two tangential directions. To better absorb the boundary reflections, COMBIN14 elements are distributed along the target vertical plate surface, the top and bottom surfaces in the vicinity of the target boundary. Figure 4.4c illustrates the variation of the damping parameter along the NRB portion of the 3D FEM mesh.

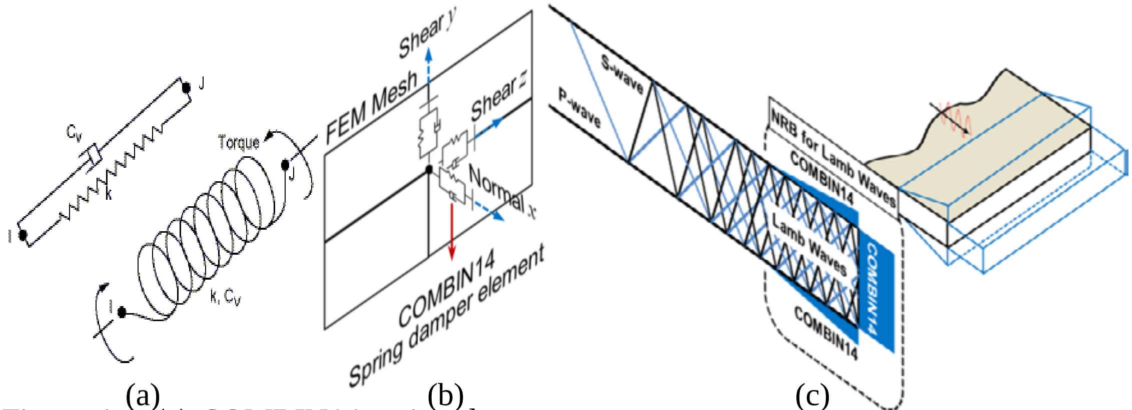

Figure 4.4: (a) COMBIN14 spring-damper element (ANSYS); (b) 3D NRB construction using COMBIN14; (c) COMBIN14 parameter distribution of NRB for Lamb waves[22]

According to Eqs. (4.5) and (4.6), the spring damper coefficients can be found

$$\begin{aligned} K_N &= 0; \quad C_N = \rho c_P L_Y L_Z \\ K_T &= 0; \quad C_T = \rho c_S L_Y L_Z \end{aligned} \tag{4.7}$$

Besides, when waves interact with the NRB, the sudden change in FEM matrices will cause reflections. After a series of numerical experiments, a linear transition distribution from zero up to 20% of the full coefficients (given in Eq.(4.7)) was chosen for top and bottom surface COMBIN14 element parameters. This transient distribution should cover at least two A0 wavelengths along the propagation direction. The vertical plate end was implemented with COMBIN14 elements with full coefficients calculated from Eq.(4.7). The effectiveness of this kind of NRB in FEM simulation in ANSYS is discussed in ref.[51]. In this study, the NRB is implemented following the ref.[51].

4.2.10 Selection of Frequency domain for the Harmonic analysis

The frequency domain of harmonic analysis was selected based on dispersion curves as shown in Figure 4.5. The frequency range corresponding to the fundamental Lamb and SH wave modes is selected in the present study. It enables us to avoid the complexities associated with higher Lamb and SH wave modes. However, at very low frequencies (<40 kHz), the wavelength of the Lamb modes are very high (Figure 4.6) and requires very wide NRB, hence, requires more computation resources in FEM. When incident fundamental Lamb wave modes (S0/A0) interact with the damage there could be presence of non-propagating (evanescent) A1 modes that die out at a certain distance from the source. It requires longer distance to die out the non-propagating A1 mode of Lamb wave at very low and very high frequencies as shown in Figure 4.7. At higher frequencies (>900 kHz), the wavelength becomes very small and requires very fine mesh to capture the damage feature, thus, require more computation efforts. At higher frequencies, the higher modes (S1, A1, S2, A2 etc.) of Lamb and SH waves can appear and make the analysis more complex. Considering these reasons, the frequency domain of 40 to 900 kHz with a frequency step of 2 kHz is selected for the harmonic analysis.

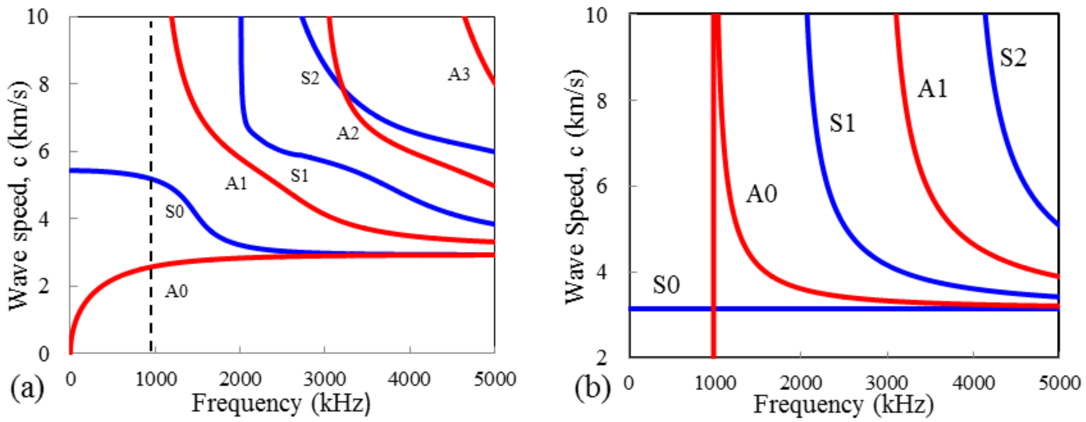

Figure 4.5: Dispersion curves for (a) Lamb wave and (b) SH wave for 1.6 mm thick aluminum plate

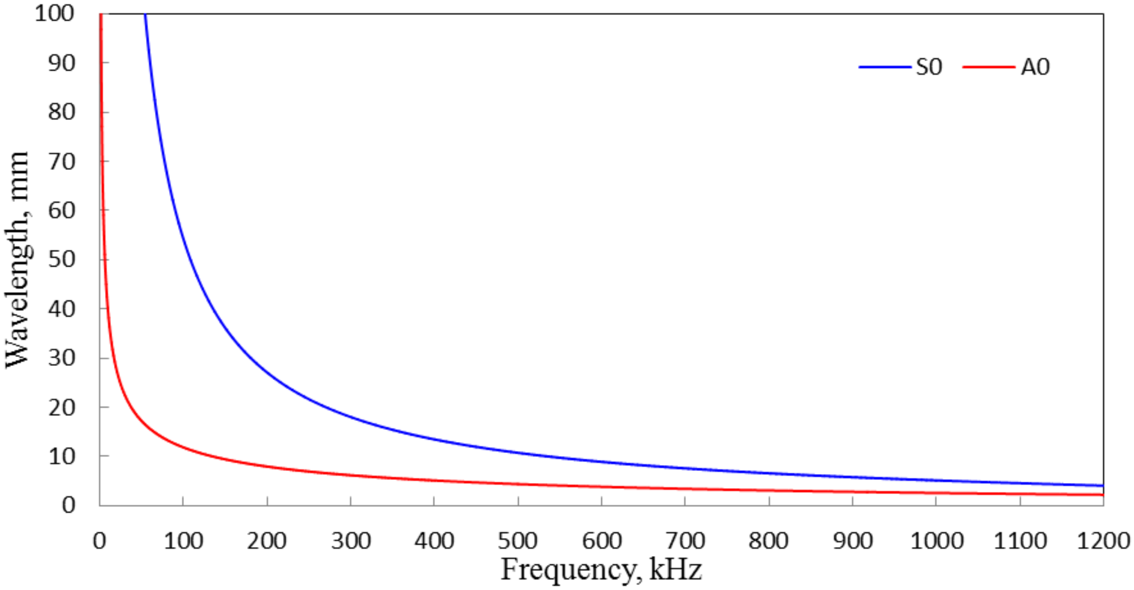

Figure 4.6: S0 and A0 Lamb mode wavelength variation with frequencies for 1.6 mm thick aluminum plate

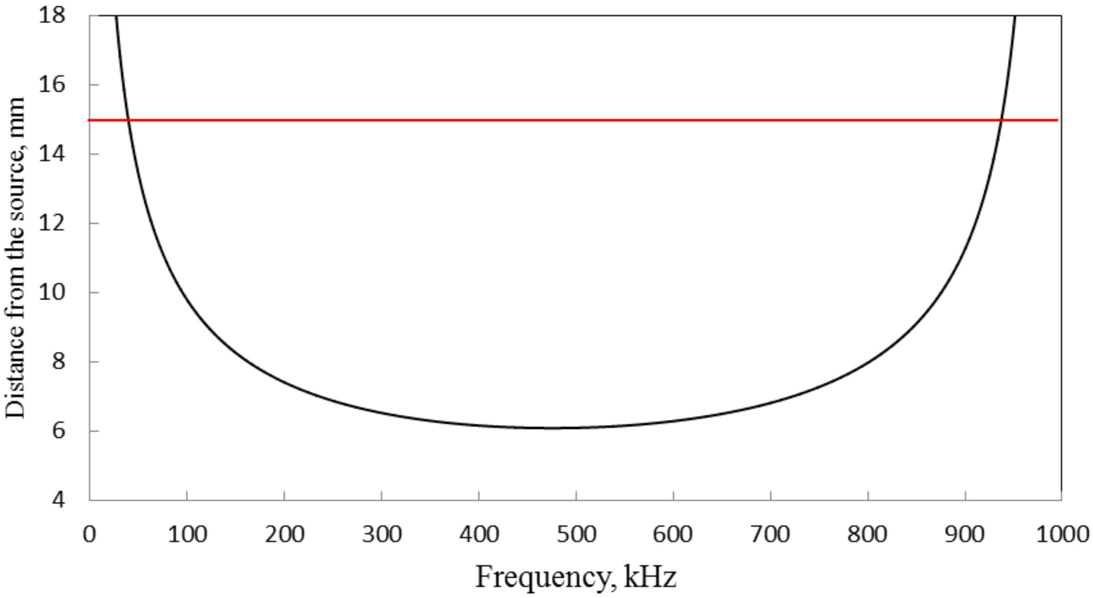

Figure 4.7: Die-out distance required for the non-propagating A1 mode

The sensing boundary is located sufficiently far away from the crack so that all non-propagating Lamb and SH scattered wave modes die out before they reach to the sensing locations. Thus, the wave fields at the sensing locations around the rivet hole with cracks are the contributions of propagating Lamb and SH wave modes.

4.2.11 VALIDATION OF THE FE MODEL

The finite element results are validated with the results obtained for Lamb wave incident at 0° in ref.[35]. Since no closed form solution is available for the type of damage that we are considering in the study, the final FEM result cannot be compared. However, a simple case in which analytical results are available can be used to validate our FEM results. The analytical WDIC profiles for the Lamb wave and SH wave for a pristine plate has been derived by Bhuiyan et al.[58] and shows that WDIC profiles follow ideal double-circled shape. The FEM result is compared with the analytical result as shown in Figure 4.8. The FEM results show very good agreement with the analytical results.

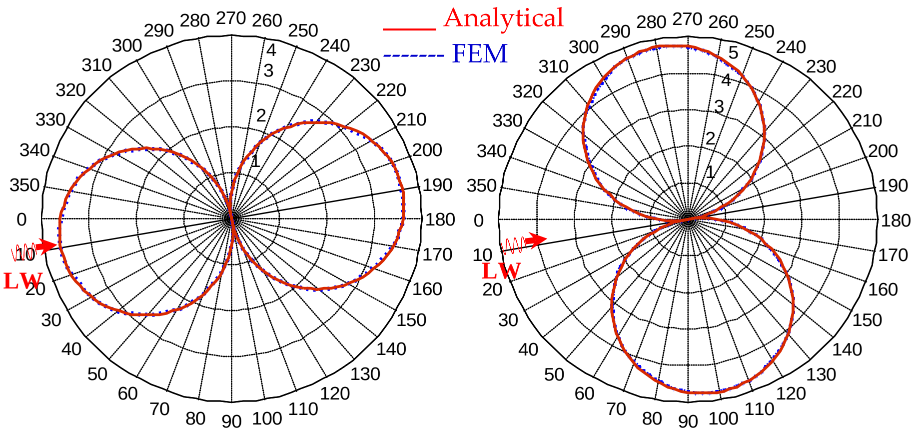

(a) Lamb wave (b) SH wave

Figure 4.8: Comparison between analytical and FEM results (a) $\text{WDIC}_{\text{LW\_LW}}$ (b) WDICLW$_{\text{\_SH}}$ in polar coordinates (pristine plate)

4.3 DISCUSSION OF THE SIMULATION RESULTS

Three sets of FEM simulations were carried out to find the contribution of the butterfly cracks into the WDICs: (a) Lamb wave interaction with rivet hole with butterfly cracks, (b) Lamb wave interaction with rivet hole, and (c) Lamb wave interaction with a pristine plate. In order to get the wave field at the sensing boundary due to the presence of butterfly cracks in a rivet hole, the wave field of hole was subtracted from the combined wave field of rivet hole with butterfly cracks. The wave field of the pristine model provides the required direct incident wave fields at the center of the damage and used for the normalization purpose. The WDICs provides the indication of getting strong or weak signals around the damage. In order to readily identify those locations, the WDICs are plotted in polar coordinate system.

4.3.1 FORMATION OF SCATTER CUBE

For each transmitting angle (θ), the WDICs are recorded at azimuth sensing angles (Φ) around the sensing boundary over the frequency domain. The results of the harmonic analyses of the 3D FEM model facilitate forming a "scatter cube" of complex-valued WDICs. The three dimensions of the scatter cube contain the WDICs for various frequencies, angles of transmitting PWASs, and angles of sensing PWASs. These WDICs can describe complicated 3-D interaction between the interrogating waves and damage, i.e., scattering and mode conversion. Since the problem of rivet hole with cracks is symmetric with respect to the midplane of the thickness direction, no antisymmetric wave mode generates for symmetric Lamb wave incident and vice versa.

4.3.2 DISTORTION OF WDIC PROFILE DUE TO THE PRESENCE OF CRACKS

The polar plot of WDIC (WDIC profile) of the scattered S0 Lamb mode and SH mode due to incident S0 Lamb mode at $\theta = 9°$ is shown in Figure 4.9. An arbitrary frequency $f = 486$ kHz is selected for the illustration purpose only. When there is no damage (pristine) in the plate, there is no scattered wave field and the WDIC profile is an ideal double-circled shape. When there is a rivet hole in the plate, the presence of scattered field makes distortion of the ideal shape of WDIC profile as shown in Figure 4.9b and the profile is symmetric about the line of incidence since the rivet hole is symmetric about the line of incidence. When there is damage (butterfly cracks) in the rivet hole, the additional scattered waves due to damage provides additional distortion to the WDIC profile. The WDIC profile for hole+crack is no more symmetric (Figure 4.9c) since the damaged rivet hole (hole+crack) is not symmetric about the line of incidence. In order to clearly identify the effect of damage in the plate, the scattered fields can be separated from the total fields.

To find out the scattered field due to the presence of hole, incident wave fields (wave fields due to pristine) needs to be subtracted from the total wave field (incident + scattered) and the corresponding WDIC profile of hole (only) is plotted in Figure 4.10a. Similarly, to find out the scattered field due to the presence of crack (only), the scattered wave field of hole (only) and the incident wave fields needs to be subtracted from the total wave fields (due to hole with crack + incident). The corresponding WDIC profile of scattered S0 Lamb mode and SH wave for crack (only) is plotted in Figure 4.10b. The WDIC profiles indicate that the magnitude of WDIC reaches to larger value at certain azimuth angles Φ.

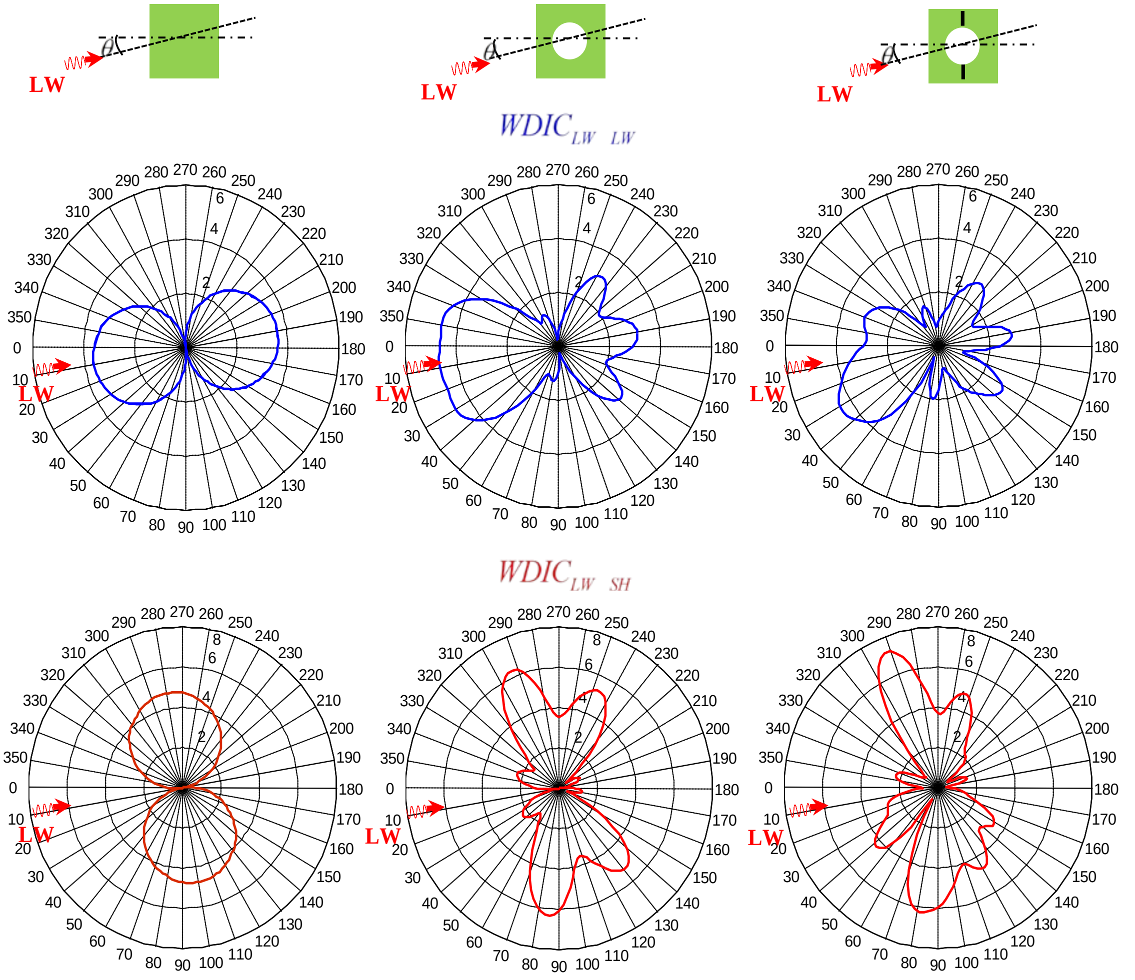

(a) Pristine (ideal)

(b) Hole

(c) Hole+Crack

Figure 4.9: Alteration of WDIC profiles of scattered Lamb and SH wave with different damage conditions

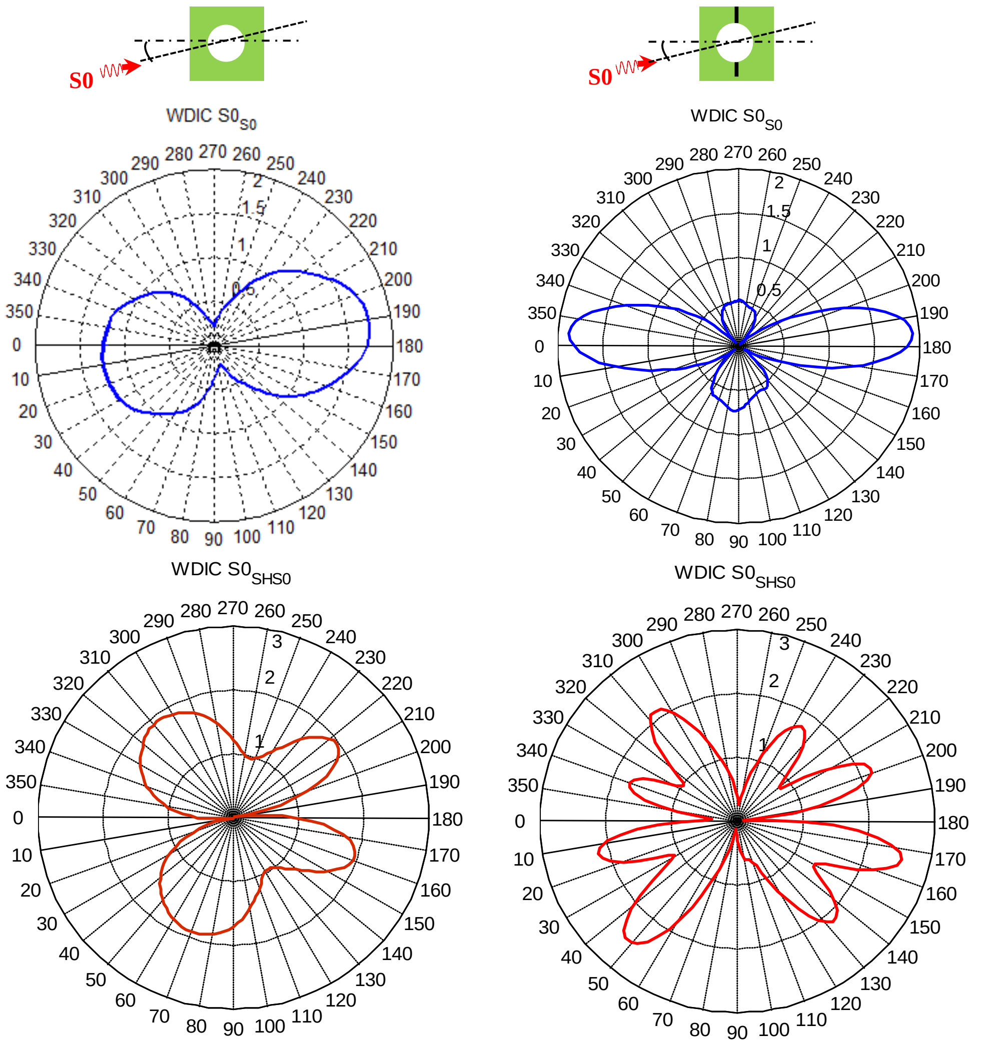

(a) Hole only (b) Crack only

Figure 4.10: Subtracted WDIC profiles of scattered Lamb and SH wave to account the damage effect only

4.3.3 FREQUENCY DOMAIN VARIATION OF WDIC AT DIFFERENT AZIMUTHAL POSITIONS

For a certain Lamb wave mode (S0 mode) incident from a particular direction ($\theta = 9^\circ$) to the cracked rivet hole is shown in Figure 4.11 Five different azimuthal locations are picked arbitrarily to show the frequency domain variation of the WDICs. It can be noticed that at a certain location, a certain frequency of excitation provides the largest magnitude of WDIC. This frequency may be termed as sensitive frequency of that location. However, at a certain sensitive frequency, not all the azimuthal locations are necessarily equally sensitive. Thus the selection of frequency of excitation as well as the location is important to capture the damage signature. By comparing all azimuthal location, it is possible to select a certain frequency that corresponds to the highest magnitude of the WDIC, for example, in this particular case, the star marked frequency ($f = 538\text{ kHz}$) can be the most sensitive excitation frequency at location 5 (“most sensitive location”).

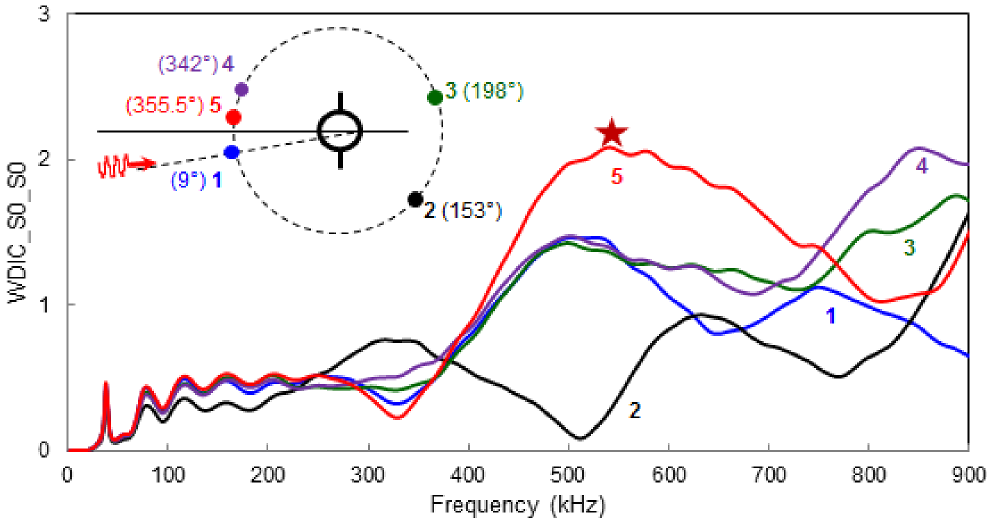

Figure 4.11: Frequency domain variation of WDIC_{S0_S0} at different azimuthal positions ($\theta = 9°$)

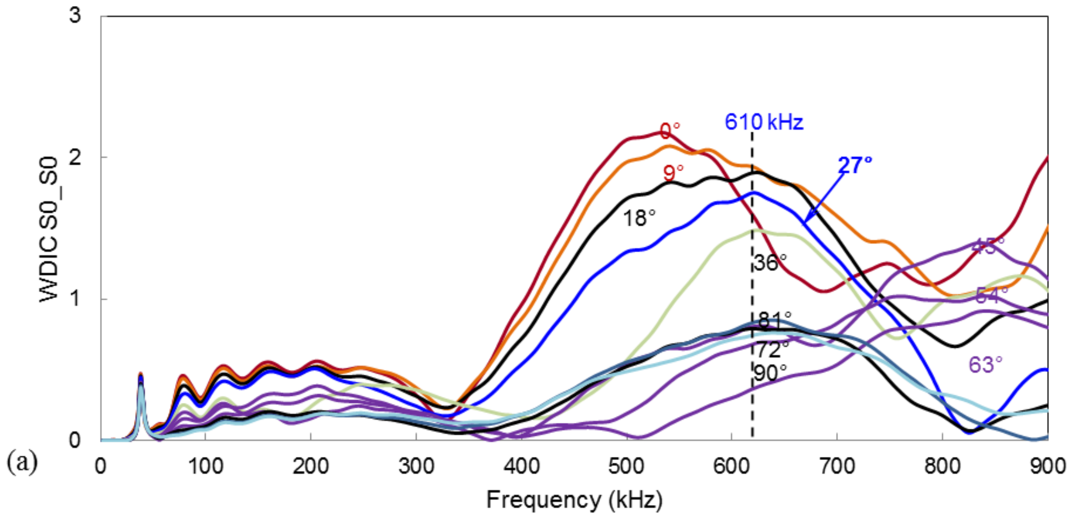

Figure 4.12: Frequency domain variation of WDIC$_{S0\_S0}$ for multiple incident directions

4.3.4 FREQUENCY DOMAIN VARIATION OF WDIC FOR MULTIPLE INCIDENT DIRECTIONS

The frequency domain variation of WDIC can be extended at the most sensitive locations for different directions of incident Lamb waves. Figure 4.12 illustrates all possible directions of incident Lamb waves for the multiple-rivet hole lap joint. This plot can be used to find out the optimum center frequency of excitation for a particular incident direction of Lamb waves. For example, when S0 Lamb wave mode hit the cracked rivet hole at $\theta = 27^\circ$, the excitation center frequency $f = 610$ kHz corresponds the highest WDIC. Later, we will show how the magnitude of WDIC affects the physical signal in Chapter 6.

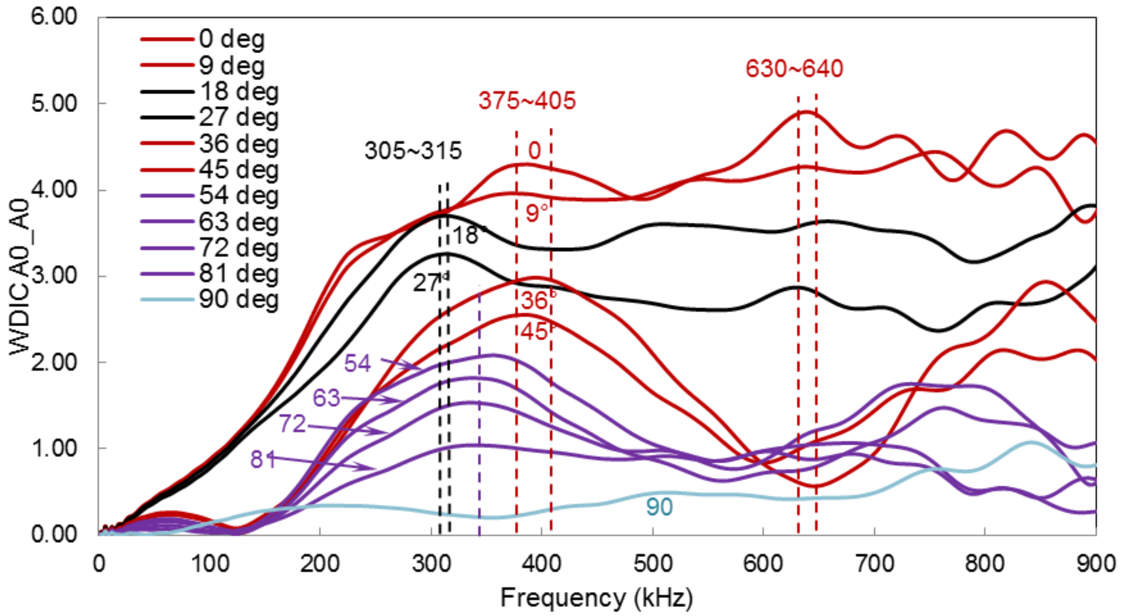

Figure 4.13: Frequency domain variation of WDIC$_{A0\_A0}$ for multiple incident directions

The similar frequency domain plots for scattered A0 mode can be produced from the scatter cube of A0 Lamb wave mode incident and has shown in Figure 4.13.

4.3.5 AZIMUTHAL VARIATION OF WDIC

The polar plot refers to the azimuthal variation of WDIC and can be used to identify the locations where WDIC reaches to maximum. The azimuthal variation of WDIC for symmetric and antisymmetric Lamb wave incident at 27° to the rivet hole cracks are shown in Figure 4.14. As the frequency changes, the WDIC profile for both symmetric and antisymmetric Lamb wave changes. It is possible to get multiple sensitive locations around the damage for a certain frequency of transmitting signal.

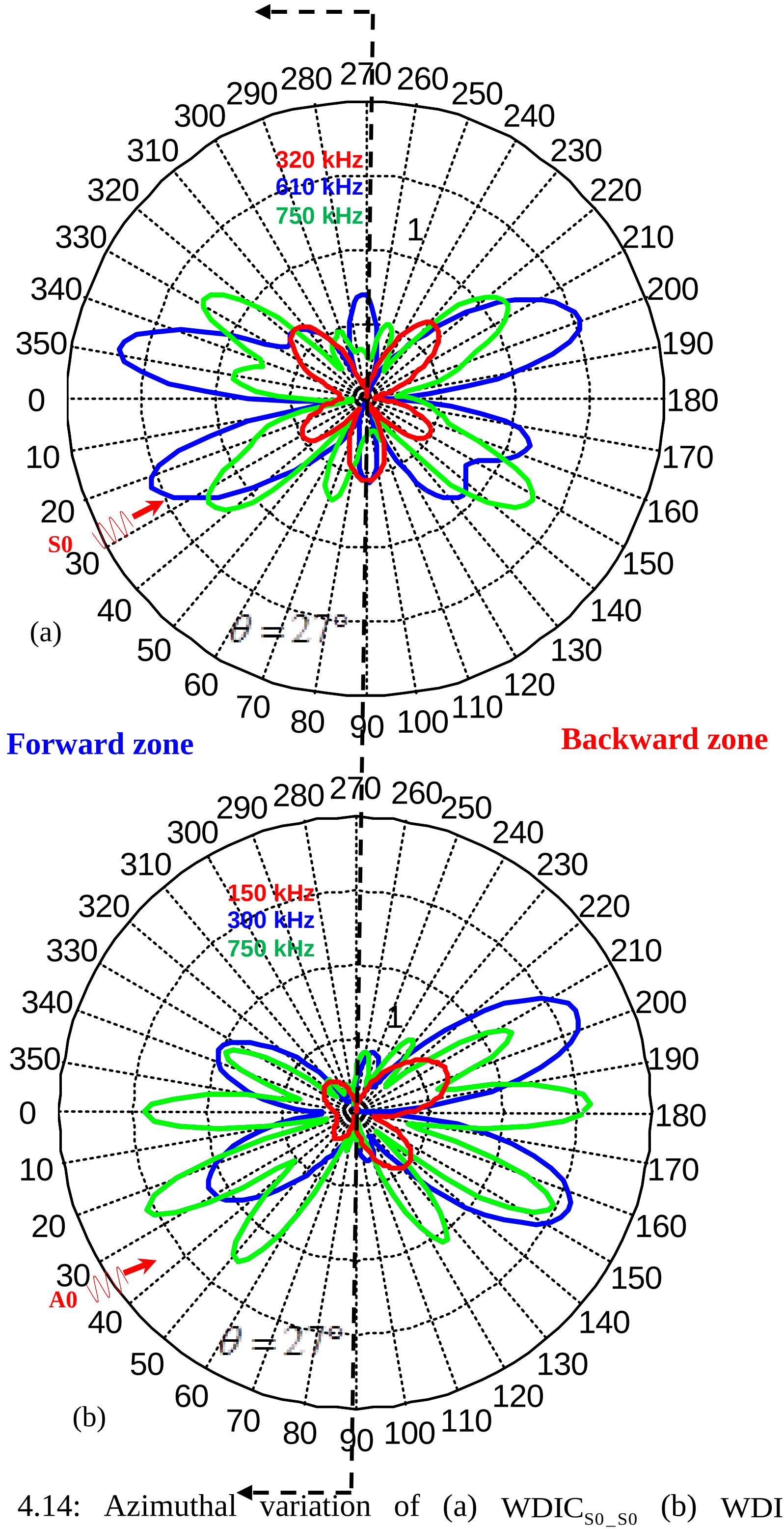

Figure 4.14: Azimuthal variation of (a) $\mathrm{WDIC}_{\mathrm{S0\_S0}}$ (b) $\mathrm{WDIC}_{\mathrm{A0\_A0}}$ at different frequencies

Sometimes, it may be important to classify the sensitive locations into two zones (forward and backward) because depending on applications there could be space limitations to install the sensors in a certain zone. In the problem of lap joint in real life structure it is convenient to install the PWASs in the forward zone only and thus, the most sensitive locations in the forward zone will come into play for optimum design of the sensors.

4.3.6 POLAR PLOTS OF WDIC FOR MULTIPLE INCIDENT DIRECTIONS

Figure 4.15 shows the variations of WDIC profiles for different angles of incident S0 Lamb wave modes. For each angle of incident most sensitive frequency is selected for these polar plots and the most sensitive locations can be obtained based on the highest magnitude of WDIC of scattered S0 modes for each angle of incident. Those sensitive locations can be used to optimize the installation of the sensors around the multiple-rivet-hole lap joints. It shows the polar plots for incident directions from 0° to 90°. The results for 0° to -90° would be the same because of symmetry with respect to the line of incidence. Thus the all possible location of the actuator with respect to the rivet hole is considered in this analysis. It can be noticed that as the inclination increases, the magnitude of WDIC decreases. When the incident Lamb wave is in line with the cracks ($\theta = 90^\circ$), the damage becomes symmetric with respect to the line of wave incidence. Hence, the WDIC profile for $\theta = 90^\circ$ is symmetric about the line of incidence as shown in Figure 4.15. Though Figure 4.15 shows the WDIC for incident S0 mode only, the similar plots can be generated for A0 mode using the scatter cube of incident A0 mode.

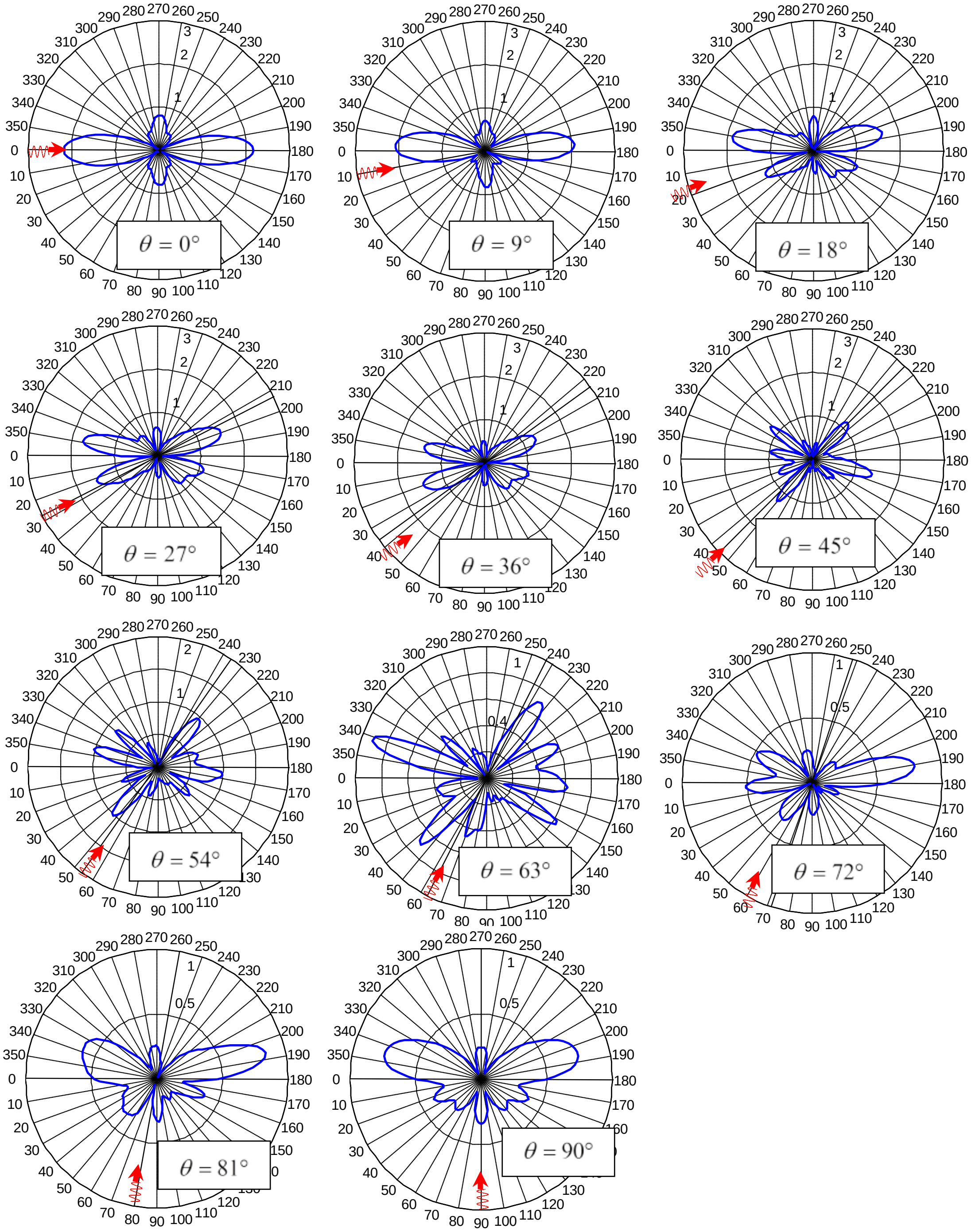

Figure 4.15: WDIC$_{S0\_S0}$ for various incident angles at most sensitive frequencies

CHAPTER 5

ANALYTICAL FRAMEWORK FOR GUIDED WAVE SENSING

This chapter focuses on the analytical part of the present study. It also illustrates the interfacing of the local FEM results with the global analytical framework. The overall process is termed as combined analytical and FEM approach (CAFA). This fundamentals of this approach was developed by Shen and Giurgiutiu[35] and showed the implementation of CAFA on a dent type damage in the structure. This is an efficient approach to simulate the signals corresponding to the detection of damage through Lamb wave interaction. An analytical predictive tool for the simulation of PWAS-generated guided waves called WFR-2D was developed[59] based on CAFA. However, WFR-2D is an interface that can simulate the wave propagation in the structure without any damage. To analyze the wave propagation in damages structure, it requires the wave damage interaction coefficients which act as the heart of the damage structure. In this study, we developed the scatter cube of wave damage interaction coefficients to analyze the cracked rivet hole problem and used WFR-2D as a useful tool to obtain the simulated signal.

5.1 OVERVIEW OF COMBINED ANALYTICAL AND FEM APPROACH

The overview of the combined analytical and FEM approach (CAFA) is illustrated in the schematic diagram as shown in Figure 5.1. It shows that the actuator excites the structure to generate the Lamb waves that propagate into the structure. Then the Lamb waves interact with the damage and undergo scattering and mode conversion.

The scattered wave also propagates into the structure and finally picked up by a sensor. In CAFA, the Lamb wave generation, propagation, damage interaction, and detection are modeled using the exact analytical expressions, while the wave damage interaction coefficients (WDICs) are extracted as a scatter cube from the small-size local FEM analysis

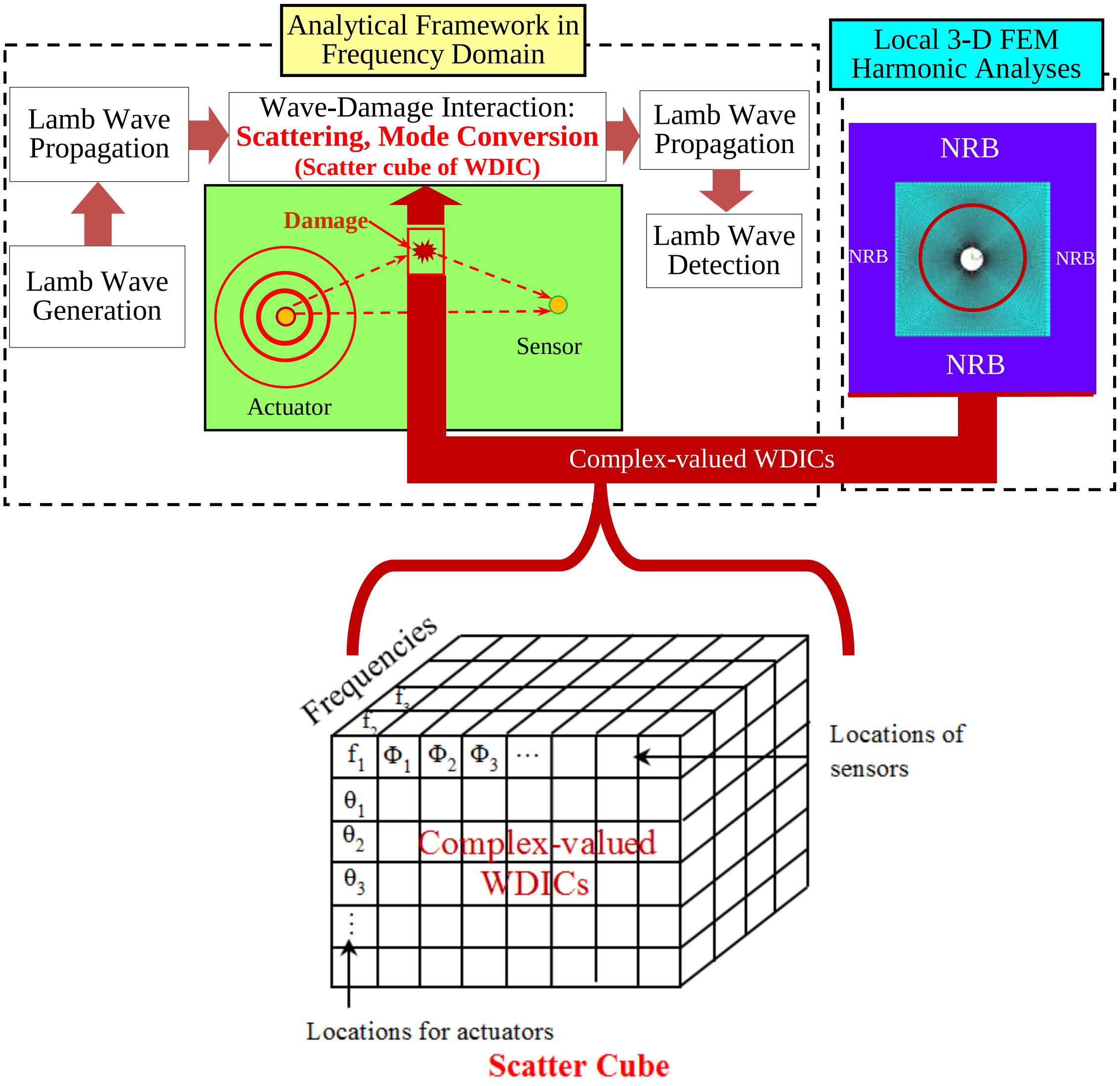

Figure 5.1: Overview of the combined analytical and FEM approach

5.2 DESCRIPTION OF THE ANALYTICAL MODEL

This section illustrates the SAFE formulation for plate structures. Details of the mathematical derivation and finite element implementation are shown.

5.2.5 LAMB WAVE GENERATION FROM THE ACTUATOR

Lamb waves are generated in the plate by a circular actuator and propagate toward the local damage. For outward propagating waves from the actuator, the radial displacement $u_r(r)$ on the top surface of the plate at any distance r from the actuator is given by Giurgiutiu[18], i.e.,

$$u_r(r)\big|_{z=d} = -\frac{\pi i}{2\mu}\sum_{j=0}^{J_S}\frac{\tilde{\tau}(\xi_j^S)N_S(\xi_j^S)}{D_S'(\xi_j^S)}H_1^{(1)}(\xi_j^S r)e^{-i\omega t} - \frac{\pi i}{2\mu}\sum_{j=0}^{J_A}\frac{\tilde{\tau}(\xi_j^A)N_A(\xi_j^A)}{D_A'(\xi_j^A)}H_1^{(1)}(\xi_j^A r)e^{-i\omega t} \tag{5.1}$$

where $\mu = G$, is the shear modulus of the plate, a is the radius of actuator and the components N_S, N_A, D_S, D_A can be defined as

$$\begin{aligned}
&N_S(\xi) = \xi\eta_S\left(\xi^2+\eta_S^2\right)\cos\eta_P d\,\cos\eta_S d \quad ; \quad N_A(\xi) = -\xi\eta_S\left(\xi^2+\eta_S^2\right)\sin\eta_P d\,\sin\eta_S d\\
&D_S = \left(\xi^2-\eta_S^2\right)^2\cos\eta_P d\,\sin\eta_S d + 4\xi^2\eta_P\eta_S\sin\eta_P d\,\cos\eta_S d\\
&D_A = \left(\xi^2-\eta_S^2\right)^2\sin\eta_P d\,\cos\eta_S d + 4\xi^2\eta_P\eta_S\cos\eta_P d\,\sin\eta_S d
\end{aligned} \tag{5.2}$$

where, $2d$ is the thickness of the plate; η_P, η_S can be defined as

$$\eta_P^2 = \frac{\omega^2}{c_P^2}-\xi^2; \quad \eta_S^2 = \frac{\omega^2}{c_S^2}-\xi^2 \tag{5.3}$$

The wavespeed $c_P = \sqrt{\lambda + 2\mu/\rho}$ and $c_S = \sqrt{\mu/\rho}$ depend on the plate material properties (Lame constants λ, μ and density ρ). The wavenumber ξ depends on the frequency and is the roots of the Rayleigh-Lamb equation [10], i.e.,

$$\frac{\tan \eta_S d}{\tan \eta_P d} = \left[\frac{-4\eta_P \eta_S \xi^2}{\left(\xi^2 - \eta_S^2\right)^2} \right]^{\pm 1} \tag{5.4}$$

where, +1 and -1 is for symmetric and antisymmetric Lamb wave modes respectively.

Considering the actuator is ideally bonded to the plate of thickness= $2d$, and τ_a be the shear stress between the plate and the transducer, the J_1 Hankel transform of the radial shear stress can be written as

$$\tilde{\tau}(\xi)_{J_1} = \tau_a a^2 J_1(\xi a) \tag{5.5}$$

where, J_1 is the first order Bessel function.

Substituting Eq.(5.5) into Eq.(5.1) yields

$$\begin{aligned} u_r(r)\big|_{z=d} = & -\pi i \frac{a^2 \tau_a}{2\mu} \sum_{\xi^S} \frac{J_1(\xi^S a) N_S(\xi^S)}{D_S'(\xi_j^S)} H_1^{(1)}(\xi^S r) e^{-i\omega t} \\ & -\pi i \frac{a^2 \tau_a}{2\mu} \sum_{\xi^A} \frac{J_1(\xi^A a) N_A(\xi^A)}{D_A'(\xi^A)} H_1^{(1)}(\xi^A r) e^{-i\omega t} \end{aligned} \tag{5.6}$$

The first kind Hankel function of order one $H_1^{(1)}$ represents an outgoing propagating waves. The wavenumber ξ depends on the frequency and is the roots of the Rayleigh-Lamb equation [10].

5.2.6 ACTUATOR TRANSFER FUNCTION

The PWAS acts as an actuator which is supplied with a voltage input. The PWAS transfer function $g_{PWAS}(\omega)$ relates the applied voltage $\tilde{V}_T(\omega)$ to shear stress τ_a and defined as

$$F_a = a\tau_a = g_{PWAS}(\omega)\tilde{V}_T(\omega) \tag{5.7}$$

where F_a is the reaction force per unit length from the structure due to the expansion of PWAS mounted on the surface of the structure, a is the radius of actuator, $\tilde{V}_T(\omega)$ can be obtained by the Fourier transform of the time-domain excitation signal $V_T(t)$. The transfer function $g_{PWAS}\left(\omega\right)$ of the actuator can be derived as in Eq.(5.8). The detail derivation can be found in ref. [60].

$$g_{PWAS}\left(\omega\right)=\frac{d_{31}}{s_{11}^{E}}\frac{r\left(\omega\right)}{1-r\left(\omega\right)} \tag{5.8}$$

where $r\left(\omega\right)=k_{str}(\omega)/k_{PWAS}$ is the stiffness ratio between host structure and actuator, d_{31} is piezoelectric strain coefficient, s_{11}^{E} is the mechanical compliance of the actuator material measured at zero electric field ($E=0$)[60].

The WDIC obtained from the FEM analysis depends on the material properties of host structure while the final signal received depends on both the transducer material properties and host structure properties.

5.2.7 STRUCTURE TRANSFER FUNCTION

The roots of the Rayleigh-Lamb equation Eq. (5.4) provide numerous symmetric and antisymmetric wavenumbers ξ^S , ξ^A for a certain excitation frequency ω. These wavenumbers are used in the summation process in Eq.(5.6). In general, the structural transfer function $G(\omega,r)$ may be defined as the conversion of the frequency domain voltage $\tilde{V}_T(\omega)$ and the displacement $u_r(\omega,r)$ induced in the host structure given by Eq.(5.9)

$$u_r(\omega,r)=G\left(\omega,r\right)\tilde{V}_T(\omega) \tag{5.9}$$

The structural transfer function $G(\omega, r)$ can be obtained by substituting Eq. (5.7) into Eq.(5.6) and dividing by $e^{-i\omega t}$. For convenience, the symmetric (S) and antisymmetric (A) part of the structure transfer function may be separated as

$$G^{S}\left(\omega, r\right) = -\pi i \frac{a g_{PWAS}\left(\omega\right)}{2\mu} \sum_{\xi^{S}} \frac{J_{1}(\xi^{S} a) N_{S}(\xi^{S})}{D_{S}'(\xi^{S})} H_{1}^{(1)}(\xi^{S} r) \tag{5.10}$$

$$G^{A}\left(\omega, r\right) = -\pi i \frac{a g_{PWAS}\left(\omega\right)}{2\mu} \sum_{\xi^{A}} \frac{J_{1}(\xi^{A} a) N_{S}(\xi^{A})}{D_{S}'(\xi^{A})} H_{1}^{(1)}(\xi^{A} r) \tag{5.11}$$

5.2.8 DIRECT INCIDENT SIGNAL

The structure transfer function can be multiplied by the frequency-domain excitation signal $\tilde{V}_T(\omega)$ to obtain the direct incident waves at the sensing location, i.e.,

$$u_{IN}\left(\omega, R_{IN}\right) = \tilde{V}_T(\omega)\left[G^{S}\left(\omega, R_{IN}\right) + G^{A}\left(\omega, R_{IN}\right)\right] \tag{5.12}$$

where the distance R_{IN} from actuator up to sensing location is used.

Similarly, the structure transfer function can be multiplied by $\tilde{V}_T(\omega)$ up to the damage location to obtain the interrogating waves arriving at the damage, i.e.,

$$u_{D}\left(\omega, R_{D}\right) = \tilde{V}_T(\omega)\left[G^{S}\left(\omega, R_{D}\right) + G^{A}\left(\omega, R_{D}\right)\right] \tag{5.13}$$

where the distance R_D from actuator up to the damage location is used

It can be noticed that the Lamb modes propagate independently and direct incident wave field is the superposition of symmetric and antisymmetric wave modes.

5.2.9 INSERTING THE SCATTER CUBE OF WDICS FOR THE SCATTERED WAVEMODES

The scatter cube obtained from the local FE analysis provides the scattered coefficients for the scattered wave modes ($C_{SS}, C_{AS}, C_{SA}, C_{AA}, C_{SSH}, C_{ASH}$) following Eq.

(5.14). The detail has been discussed in Chapter 3 and 4. Each scattered mode forms a scatter cube considering the multiple incident directions of Lamb wave.

$$C_{AB}(\omega,\theta,\Phi) = \left| \frac{u_{SC}^{B}(\omega,\theta,\Phi)}{u_{IN}^{A}} \frac{1}{H_m^{(1)}\left(\xi^B r\right)} \right| \tag{5.14}$$

$$\varphi_{AB}(\omega,\theta,\Phi) = \Delta\varphi_{AB}(\omega,\theta,\Phi) - \left[\angle \frac{1}{H_m^{(1)}\left(\xi^B r\right)} - \angle \frac{1}{H_m^{(1)}\left(0^+\right)} \right] \tag{5.15}$$

Scattered wave source at the damage location is obtained by modifying incident waves at the damage with WDICs

$$u_N^S = C_{SS}(\omega,\theta,\Phi) e^{-i\varphi_{SS}(\omega,\theta,\Phi)} u_D^S + C_{AS}(\omega,\theta,\Phi) e^{-i\varphi_{AS}(\omega,\theta,\Phi)} u_D^A \tag{5.16}$$

$$u_N^A = C_{SA}(\omega,\theta,\Phi) e^{-i\varphi_{SA}(\omega,\theta,\Phi)} u_D^S + C_{AA}(\omega,\theta,\Phi) e^{-i\varphi_{AA}(\omega,\theta,\Phi)} u_D^A \tag{5.17}$$

$$u_N^{SH} = C_{SSH}(\omega,\theta,\Phi) e^{-i\varphi_{SSH}(\omega,\theta,\Phi)} u_D^S + C_{ASH}(\omega,\theta,\Phi) e^{-i\varphi_{ASH}(\omega,\theta,\Phi)} u_D^A \tag{5.18}$$

where u_N^S, u_N^A, and u_N^{SH} represent the damage scattered S0, A0, and SH0 wave source respectively. The new wave source (damage) irradiates the scattered waves that propagate to the sensing location. The 2-D Lamb wave irradiating from a point source accepts the following solution in the cylindrical coordinate system with reference to the new wave source location [18][23].

$$u_r = \sum_{n=1}^{\infty} a_n^{LW}(z) H_1^{(1)}\left(\xi_n^{LW} r\right) e^{-i\omega t} \tag{5.19}$$

$$u_\theta = \sum_{n=1}^{\infty} b_n^{SH}(z) H_1^{(1)}\left(\xi_n^{SH} r\right) e^{-i\omega t} \tag{5.20}$$

where $a_n^{LW}(z)$ and $b_n^{SH}(z)$ are the thickness dependent modeshapes for Lamb and SH waves of nth wave mode.

5.2.10 SCATTERED SENSING SIGNALS

Since the amplitude relationship between the interrogating waves and the scattered waves is enclosed in the WDICs, the transfer function from the damage up to the sensing location is simply $H_1^{(1)}\left(\xi R_{SC}\right)$, where R_{SC} is the distance from the damage up to the sensing location. Thus, the scattered waves arriving at the sensing point can be calculated.

$$u_{SC}^{S}=u_N^S H_1^{(1)}\left(\xi^S R_{SC}\right);\quad u_{SC}^{A}=u_N^A H_1^{(1)}\left(\xi^A R_{SC}\right);\quad u_{SC}^{SH}=u_N^{SH} H_1^{(1)}\left(\xi^{SH} R_{SC}\right) \qquad (5.21)$$

It should be noted that the scattered wave fields in Eq.(5.21) are the in-plane wave displacements. The symmetric and antisymmetric scattered wave displacements (u_{SC}^{S}, u_{SC}^{A}) can be detected by the PWAS transducers and the scattered SH waves can be detected by the horizontally polarized transducers. To detect the scattered waves using laser vibrometer measurement, one needs to convert the in-plane wave motion into out-of-plane wave motion since laser vibrometer measures the out-of-plane particle velocity

The out-of-plane displacement wave field may be obtained through the multiplication of the in-plane displacements by the modeshape component ratio as in Eq. (5.22)[18].

$$u_z^S=u_r^S\frac{U_z^S\left(f,d\right)}{U_r^S\left(f,d\right)};\quad u_z^A=u_r^A\frac{U_z^A\left(f,d\right)}{U_r^A\left(f,d\right)} \qquad (5.22)$$

where $U_r^S, U_z^S, U_r^A, U_z^A$ are Lamb wave modeshape displacement components evaluated at the top surface of the structure. The modeshape solutions can be found in ref.[18]. The out-of-plane velocity would be the time derivative of the out-of-plane displacement as in Eq.(5.23).

$$\dot{u}_z\left(\omega, R_D, R_{SC}, \theta\right) = -i\omega u_z \tag{5.23}$$

The time domain signal can be obtained by operating the inverse Fourier Transform of the Eq. (5.23)

$$\dot{u}_z\left(t, R_D, R_{SC}, \theta, \Phi\right) = IFFT\left[\dot{u}_z\left(\omega, R_D, R_{SC}, \theta, \Phi\right)\right] \tag{5.24}$$

The simulated time domain signal carries the damage information that is introduced in the next Section.

5.3 SIMULATED TIME DOMAIN SIGNALS

In this section we will show how the time domain signals vary with the selection of the frequency and locations of the sensors. Three count tone burst signal is excited from the actuator. A 7 mm diameter PWAS is used as an actuator. The actuator is located at 100 mm away from the damage (rivet hole with butterfly cracks). The position of the sensor is varied around the damage. The radial distance from the damage to the sensor is kept 30 mm.

5.3.1 ILLUSTRATION OF THE SIGNAL EXTRACTION DUE TO CRACKS ONLY

The signal extraction process is illustrated in Figure 5.2. When there is hole in the plate the signal in the sensor is shown in Figure 5.2a, and in presence of cracks in the rivet holes, the sensor signal changes as shown in Figure 5.2b. By subtracting two signals, the signals due to the cracks can be obtained as Figure 5.2c. This illustration is shown for a particular frequency of 538 kHz and when Lamb waves incident horizontally to the rivet hole with cracks.

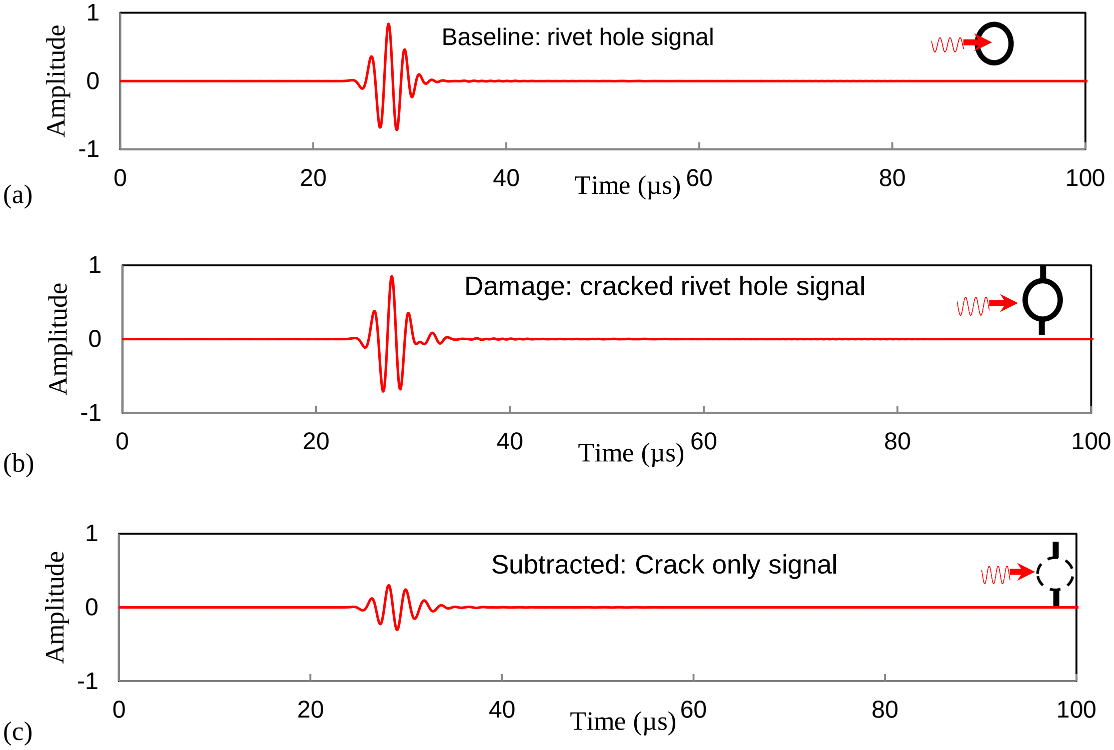

Figure 5.2: (a) The base line reference signal for the hole. (b) The signal due to Hole + Crack (c) Signal due to the crack only ($f = 538$ kHz , $\theta = 0°$)

5.3.2 DETERMINATION OF THE OPTIMUM PARAMETER FOR A SIMPLIFIED CASE

In this present research, we consider a simplified case of the multiple-rivet-hole problem as shown in Figure 5.3 where the actuator is located at θ. Later, some specific values of θ are taken ($9°$, $18°$, $27°$) for the illustration A single rivet hole is considered for determining the optimum location of the sensor and the optimum frequency of excitation. Furthermore, the rivet hole is considered located at sufficiently far away from the edge of the plate (the length, B, is large) so that: (1) the reflection from the edge dies out sufficiently before it reaches the sensor (2) the very low amplitude reflected signal if any would be seen in the trailing part of the main signal and can be easily discarded. When there are multiple rivet holes, there will be mutual the interactions of the scattered waves among the rivet holes. When the plate edge is located close to the rivet holes, the plate boundary would act as a secondary source of the scattered waves and distance B would have an effect on the overall result. These complexities have not been included in this present study and will be focused in our future research.

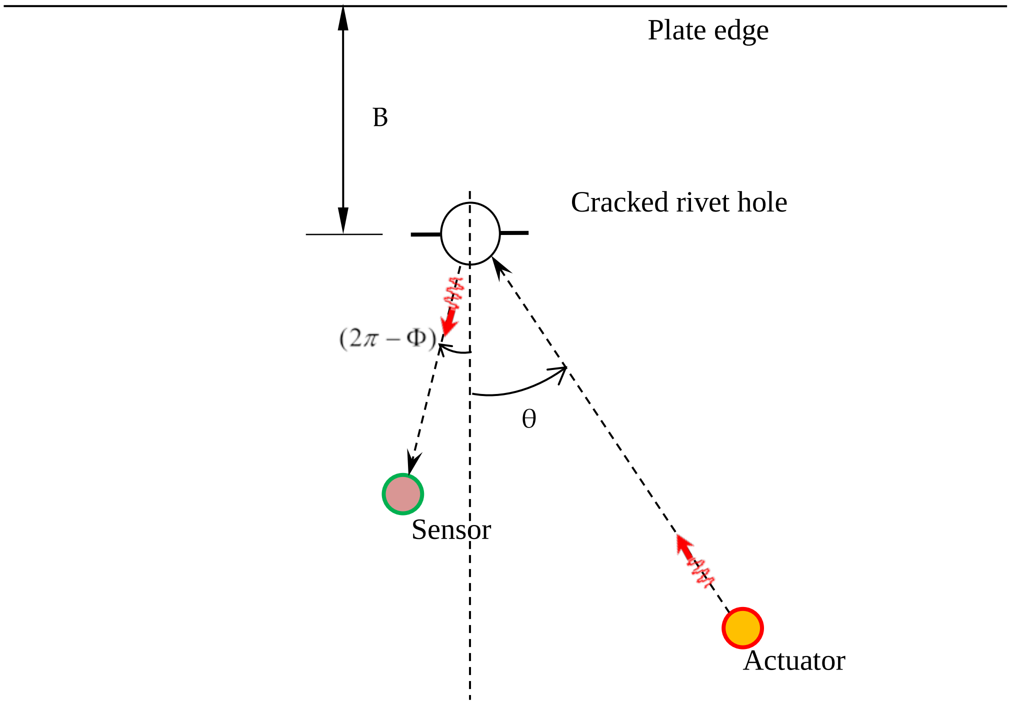

Figure 5.3: A simplified case of the multiple-rivet-hole problem

5.3.3 OPTIMUM PARAMETER FOR LAMB WAVE INCIDENT AT $\theta = 9°$

Now we consider a case when the Lamb wave (S0 mode) incident on the damage at $\theta = 9°$. The sensing signal for the cracks (in the rivet hole) only is illustrated as shown in Figure 5.4. Four different sets of parameters (frequency and location) are considered based on the analysis of scatter cube of complex-valued WDICs. (The analysis of the scatter cube is discussed in Chapter 4)

(a) Set 1: $f = 328$ kHz, $\Phi = 355.5°$ - correspond to the low magnitude of WDIC

(b) Set 2: $f = 538$ kHz, $\Phi = 355.5°$ - correspond to the highest magnitude of WDIC

(c) Set 3: $f = 728$ kHz, $\Phi = 355.5°$ - correspond to the moderate magnitude of WDIC

(d) Set 4: $f = 538$ kHz, $\Phi = 340°$ - correspond to the low magnitude of WDIC

In the first three parameter sets 1, 2, 3, the frequencies are changing while the location of the sensor is same. In set 4, the frequency is corresponding to the highest magnitude of WDIC while bad location of sensor corresponds to the low magnitude of WDIC. It can be easily noticed from the Figure 5.4 that, the parameter set 2 ($f = 538$ kHz, $\Phi = 355.5°$) provides the most noticeable signal picked up by the sensor Thus the right frequency as well as right location of the sensor is important to harness the damage information in the structure. Thus, for the Lamb wave incident at $\theta = 9°$, set 2 is the optimum parameter and is the best choice for the NDE/SHM engineers.

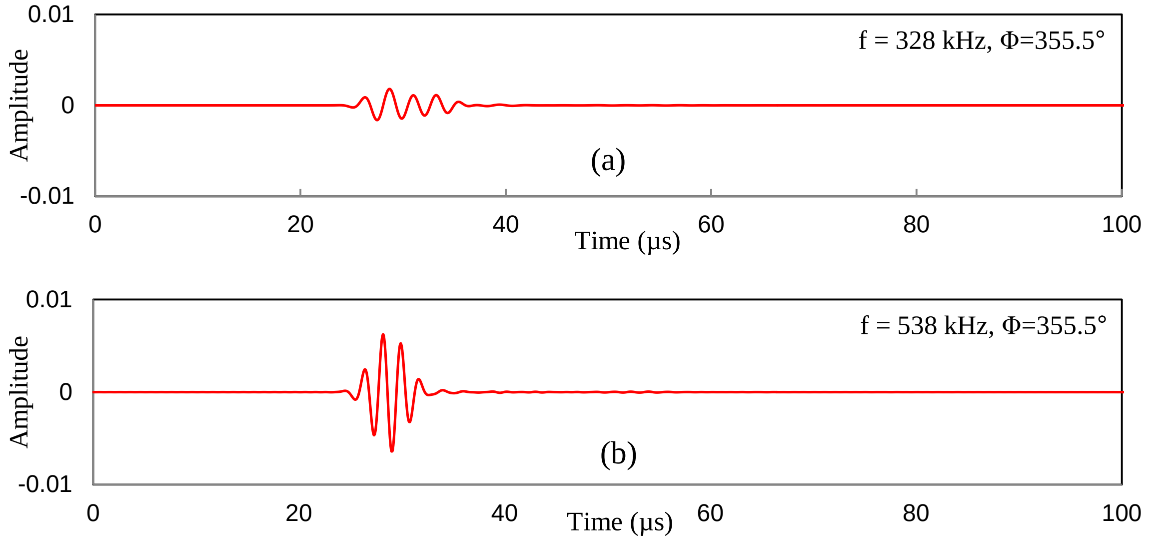

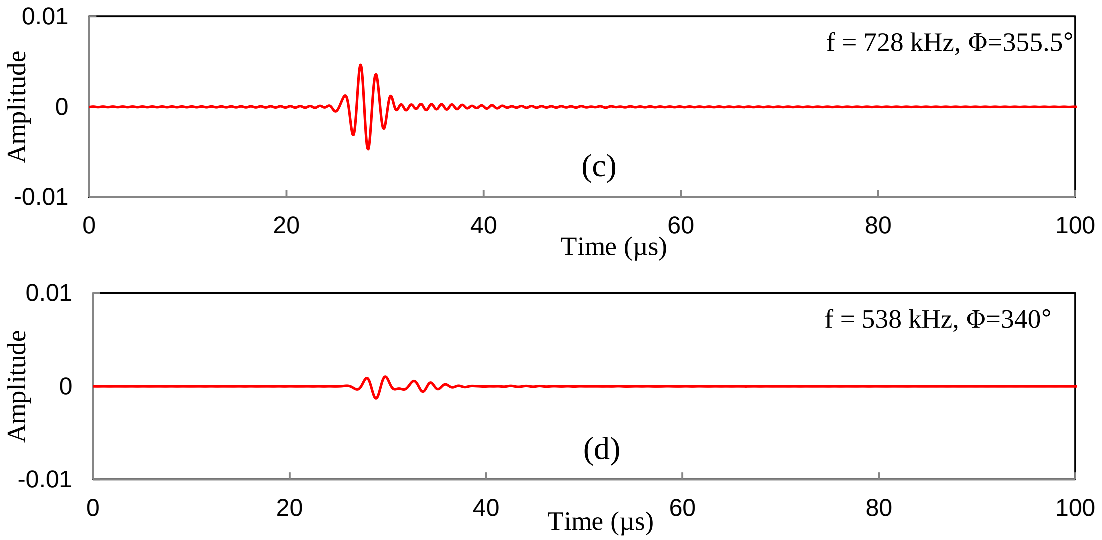

Figure 5.4: Sensing signals for different sets of frequency-location ($\theta = 9°$)

5.3.4 OPTIMUM PARAMETER FOR LAMB WAVE INCIDENT AT $\theta = 18°$

Another case may be illustrated when the Lamb wave (S0 mode) hit the rivet hole at $\theta = 18°$ which corresponds to one of the situations of the multiple-rivet-hole problem. The real time domain signals are shown in Figure 5.5 for four different sets of parameter. These parameter sets are selected based on the scatter cube analysis that has been discussed in Chapter 4.

(a) Set 1: $f = 320$ kHz, $\Phi = 350°$ - correspond to the low magnitude of WDIC

(b) Set 2: $f = 486$ kHz, $\Phi = 350°$ - correspond to the highest magnitude of WDIC

(c) Set 3: $f = 618$ kHz, $\Phi = 350°$ - correspond to the moderate magnitude of WDIC

(d) Set 4: $f = 618$ kHz, $\Phi = 75°$ - correspond to the low magnitude of WDIC

By observing the time domain signal of, the obvious selection of Figure 5.5, parameter is either (b) or (c), because both of them correspond to the most sensible signal. Thus the excitation frequency of 486~618 kHz at the transmitter and the receiver sensor at $\Phi = 350°$ is the optimum design parameter for detecting the cracks in that rivet hole.

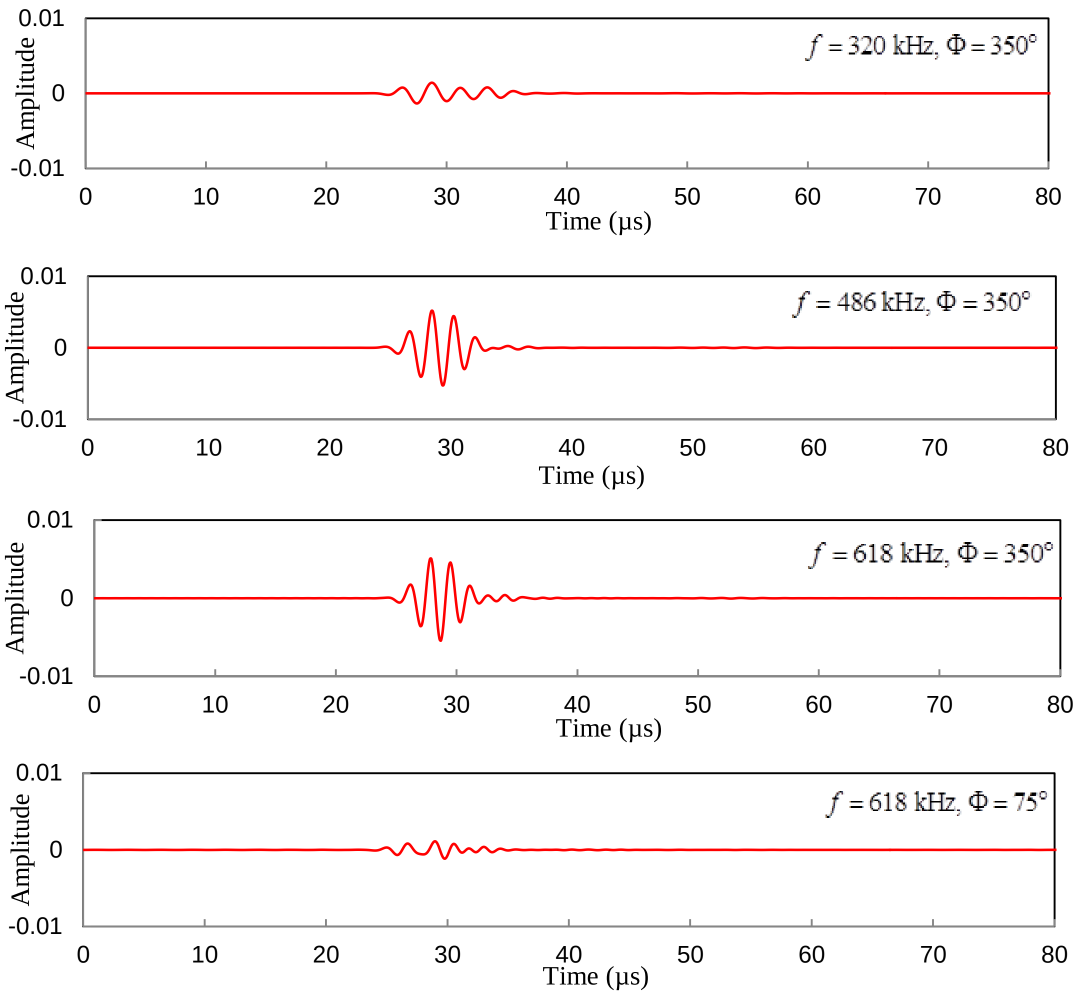

Figure 5.5: Sensing signals for different sets of frequency-location ($\theta = 18°$)

5.3.5 Optimum Parameter for Lamb Wave Incident at $\theta = 27°$

When the Lamb wave (S0 mode) incident at $\theta = 27°$ i.e. the actuator is located at $\theta = 27°$, we may choose four different sets of parameters (frequency and location) based on the analysis of scatter cube of complex-valued WDICs.

(e) Set 1: $f = 320$ kHz, $\Phi = 348°$ - correspond to the low magnitude of WDIC

(f) Set 2: $f = 610$ kHz, $\Phi = 348°$ - correspond to the highest magnitude of WDIC

(g) Set 3: $f = 710$ kHz, $\Phi = 348°$ - correspond to the moderate magnitude of WDIC

(h) Set 4: $f = 610$ kHz, $\Phi = 292°$ - correspond to the low magnitude of WDIC

In the first three parameter sets 1, 2, 3, the frequencies are changing while the location of the sensor is same. In set 4, the frequency is corresponding to the highest magnitude of WDIC while bad location of sensor corresponds to the low magnitude of WDIC. It can be easily noticed from the Figure 5.6 that, the parameter set 2 ($f = 610$ kHz, $\Phi = 348^\circ$) provides the most noticeable signal picked up by the sensor Thus the right frequency as well as right location of the sensor is important to harness the damage information in the structure. Thus, for the Lamb wave incident at $\theta = 27^\circ$, set 2 is the optimum parameter and is the best choice for the NDE/SHM engineers.

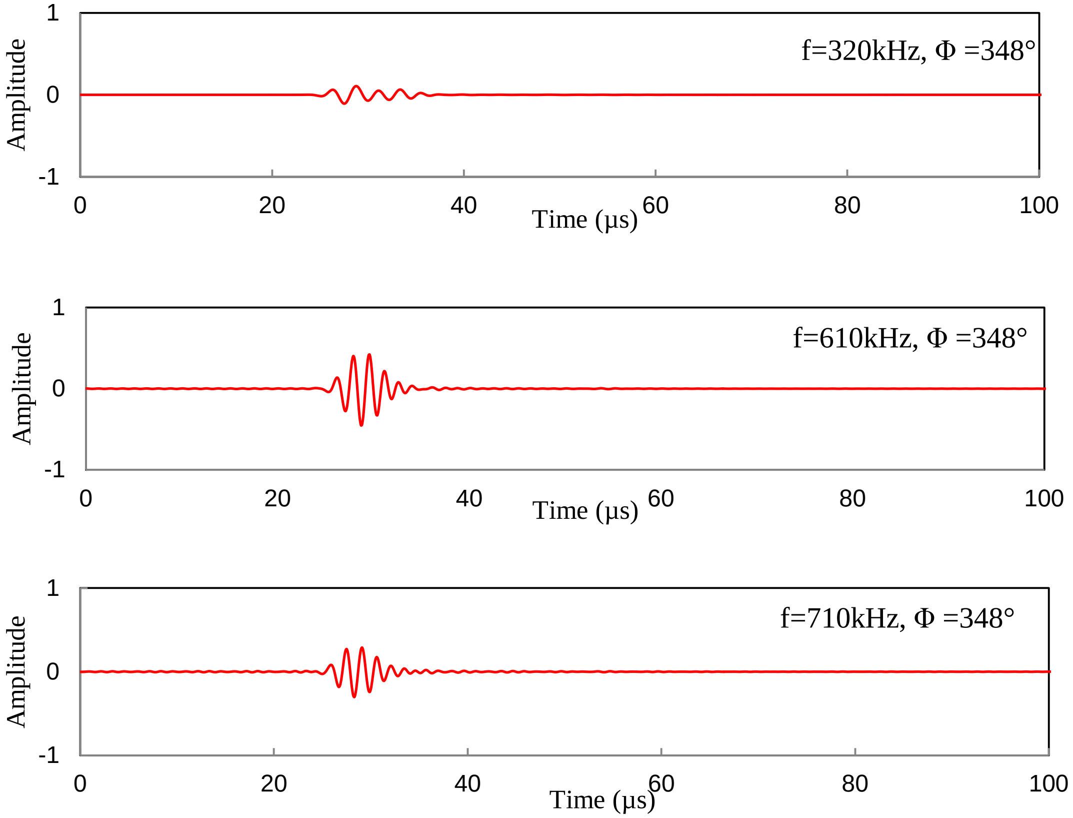

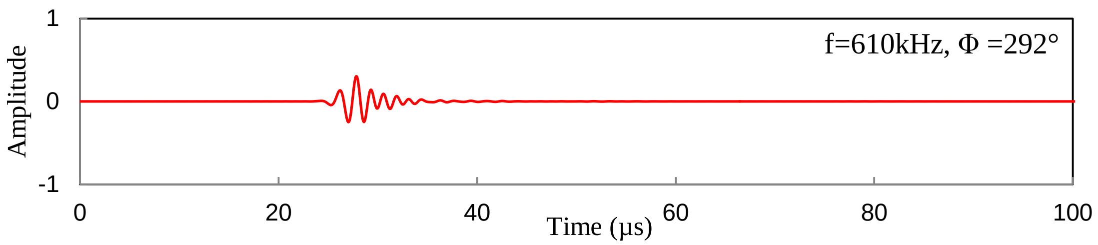

Figure 5.6: Sensing signals for different sets of frequency-location ($\theta = 27°$)

In this present study, the generalize procedure is illustrated followed by some specific examples. We may do the similar analysis for each of the rivet hole of the multiple-rivet-hole problem and determine the optimum positions of the actuator and sensors. We can also optimize the required number of actuators and sensors that demands future study.

CHAPTER 6

CONCLUSIONS AND FUTURE WORK

This thesis has presented the development of accurate, efficient, and versatile modeling techniques for guided wave based active sensing procedures for the crack monitoring in the rivet hole. The main conclusions and future work are mentioned below.

6.1 CONCLUSION

Exact analytical formulation has been used throughout the structure except the local damage area and the local damage is analyzed using the finite element method. In order to analyze some simplified case of the multiple-rivet-hole lap joint cracks, the Lamb waves have been impinging to the damage from all possible directions. Interactions of Lamb waves with rivet hole cracks from multiple directions have been described by the complex-valued wave damage interaction coefficients. Finite element analyses have been used to determine the wave damage interaction coefficients (WDICs) that involve scattering and mode conversion. SH waves appear in the scattered waves besides the Lamb waves because of the mode conversion. Local small-size damage model with proper non-reflective boundary is analyzed for efficient FE analysis. The scatter cubes are produced for the scattered waves to accommodate the 3D interaction (frequency-incident direction-azimuth direction) of Lamb waves with the rivet hole cracks.

WDIC profiles for pristine case are developed analytically and comparison with the finite element results shows very good agreement. The scattered fields for the presence of cracks are obtained through the subtraction process and corresponding WDIC shows the frequency of excitation and azimuthal location dependency. The higher magnitude of WDIC gives the better signal in the sensor. Scatter cubes of WDICs are obtained that contain the scatter field information over the frequency domain, around the damage and all possible directions of incident Lamb wave modes. Both symmetric and antisymmetric fundamental Lamb wave modes (S0 and A0) are used as the incident waves for the analyses. Frequency domain analyses of the WDICs have been performed that provides the optimum frequency of most sensitive signal and the azimuth variations in the polar plots confirm the optimum location for installing the sensor. The selection of optimum frequency and location can capture the damage information better than any arbitrary selection of frequency and location.

The local FEM results are fed into the exact analytical formulations of the guided wave propagation through the insertion of the scatter cube. The simulated signals corresponding to the presence of the cracks are produced. At the end, some example cases of multiple-rivet-hole cracks is addressed and optimum parameters (optimum frequency of actuator and location of the actuator-sensor) are obtained for each case. The time domain signals corresponding to the optimum parameters are produced to confirm the cracks detection in the rivet hole using the scatter cube and exact analytical framework. The optimum parameters can be used for making an algorithm of NDE/SHM unit for inspecting the multiple-rivet-hole lap joint.

6.2 RECOMMENDATION FOR FUTURE WORK

This dissertation has presented various modeling techniques for the simulation of guided wave propagation and interaction with damage. This work has laid the foundation for future investigations to extend the methodologies to more complicated structures. The suggestions for future work are listed below:

1. An experiment may be designed based on the simulated results to detect the cracks in the rivet holes with Lamb wave incident from multiple directions.
2. The design may be extended for making an algorithm for the multiple-rivet-hole lap joint and detecting the cracks in any of the rivet holes. The research may be further extended by considering the interactions among the rivet holes and the boundary reflections from the edges.
3. In the bonded section of the plate, there may occur some wave leakages through the bonded rivet, thus, the thickness of the bonded plate will come into play. The wave leakages may be considered while obtaining the optimum parameters.
4. Higher frequencies may be considered and the extension to more than the basic S0, A0, and SH0 modes should be made.
5. Inclusion of nonlinear effects in the analytical-FEM approach should be attempted.
6. FEM simulation could be performed for different crack to rivet hole diameter ratios.

REFERENCES

[1] MIL STD 1530C, "Aircraft Structural Integrity Program (ASIP)," *Department of Defense Standard Practice*, 2005. .

[2] Anon, "The Aircraft Structural Integrity Program Conference," *http://www.asipcon.com/*, 2013. .

[3] NTSB, "United Airlines Flight 232 Aircraft Accident Report," 1989.

[4] Wikimedia, "United Airlines Flight 232: Engine 2," *https://commons.wikimedia.org/w/index.php?curid=3016416*, 2007. .

[5] A. W. Hoggard and S. R. Johnson, "Understanding the new widespread fatigue damage rule," *Boeing Aero Magazine*, pp. 1–8, 2012.

[6] R. B. Thompson, L. H. Brasche, D. Forsyth, E. Lindgren, P. Swindell, and W. Winfree, "Recent Advances in Model-Assisted Probability of Detection," in *4th European-American Workshop on Reliability of NDE*, 2009.

[7] M. D. Bode, J. Newcomer, and S. Fitchett, "Transfer function model-assisted probability of detection for lap joint multi site damage detection," in *The 31th Review of Progress in Quantitative Nondestructive Evaluation*, 2012, vol. 1430, pp. 1749–1756.

[8] C. M. Schubert Kabban, B. M. Greenwell, M. P. DeSimio, and M. M. Derriso, "The probability of detection for structural health monitoring systems: Repeated measures data," *Struct. Heal. Monit.*, vol. 14, no. 3, pp. 252–264, 2015.

[9] F.-K. Chang, V. Janapati, F. Kopsaftopoulos, S. J. Lee, F. Li, and K. Lonkar, "Quantification of Structural Health Monitoring for Damage Detection," in *The 30th Aircraft Structural Integrity Program (ASIP)*, 2014.

[10] K. F. Graff, *Wave Motion in Elastic Solids*, Dover. Oxford University Press, 1991.

[11] H. Helmholtz, "Uber Integrale der Hydrodynamischen Gleichungen, Welche den Wirbelbewegungen Entsprechen," *J. fur die reine und Angew. Math.*, vol. 1858, no. 55, pp. 25–55, 1858.

[12] H. Helmholtz, "On Integrals of the Hydrodynamical Equations, which Express Vortex-Motion," *Philos. Mag. J. Sci.*, vol. 33, no. 226, pp. 485–512, 1867.

[13] P. M. Morse and H. Feshbach, *Methods of Theoretical Physics*. New York, Toronto, London: McGraw-Hill Book Company, Inc., 1953.

[14] D. C. Gazis, "Three Dimensional Investigation of the Propagation of Waves in Hollow Circular Cylinders. I. Analytical Foundation," *J. Acoust. Soc. Am.*, vol. 31, no. 5, pp. 568–578, 1959.

[15] C. E. Baum, "Vector and scalar potentials away from sources. and gauge invariance in quantum electrodynamics," *Phys. Notes*, vol. Note 3, pp. 1–31, 1991.

[16] J. D. Jackson and L. B. Okun, "Historical roots of gauge invariance," *Rev. Mod. Phys.*, vol. 73, no. 3, pp. 663–680, 2000.

[17] F. Gronwald and J. Nitsch, "The Physical Origin of Gauge Invariance," *Electr. Eng.*, vol. 81, pp. 363–367, 1999.

[18] V. Giurgiutiu, *Structural health monitoring with piezoelectric wafer active sensors*, 2nd ed. Elsevier Academic Press, 2014.

[19] V. Kamal, A,; Gresil, M,; and Giurgiutiu, "Shear Horizontal Guided Waves in Laminated Composite Plates Using SH-PWAS," in *NDT of Composites*, 2013.

[20] W. Zhou, H. Li, and F.-G. Yuan, "Guided wave generation, sensing and damage detection using in-plane shear piezoelectric wafers," *Smart Mater. Struct.*, vol. 23, no. 1, pp. 1–10, 2014.

[21] H. Lamb, "On Waves in an Elastic Plate," *Proc. R. Soc. A Math. Phys. Eng. Sci.*, vol. 93, no. 648, pp. 114–128, 1917.

[22] Y. Shen, "Structural health monitoring using linear and nonlinear ultrasonic guided waves," *PHD Thesis*, p. 224, 2014.

[23] M. Glushkov, E,; Glushkova, N,; Lammering, R,; Eremin, A,; and Neumann, "Lamb wave excitation and propagation in elastic plates with surface obstacles: proper choice of central frequency.," *Smart Mater. Struct.*, p. 11, 2011.

[24] V. Giurgiutiu, a. Zagrai, and J. Jing Bao, "Piezoelectric Wafer Embedded Active Sensors for Aging Aircraft Structural Health Monitoring," *Struct. Heal. Monit.*, vol. 1, no. 1, pp. 41–61, 2002.

[25] Z. Chang and A. Mal, "Scattering of Lamb waves from a rivet hole with edge cracks," *Mech. Mater.*, vol. 31, no. 3, pp. 197–204, 1999.

[26] V. Giurgiutiu and J. Bao, "Embedded-ultrasonics Structural Radar for In Situ Structural Health Monitoring of Thin-wall Structures," *Struct. Heal. Monit.*, vol. 3, no. 2, pp. 121–140, 2004.

[27] L. Yu and V. Giurgiutiu, "In-situ optimized PWAS phased arrays for Lamb wave structural health monitoring," *J. Mech. Mater. Struct.*, vol. 2, no. 3, pp. 459–487, 2007.

[28] F. Wang, C,; Rose , J,; and Chang, "A Synthetic Time-Reversal Imaging Method for Structural Health Monitoring," *Smart Mater. Struct.*, pp. 415–423, 2004.

[29] V. Giurgiutiu, A. Reynolds, and C. a Rogers, "Experimental Investigation of E / M Impedance Health Monitoring for Spot-Welded Structural Joints Description of the Specimen," *J. Intell. Mater. Syst. Struct.*, vol. 10, pp. 802–812, 1999.

[30] V. Giurgiutiu and A. Zagrai, "Electro-mechanical impedance method for crack detection in in Thin Plates," *J. Intell. Mater. Syst. Struct.*, vol. 12, no. 10, pp. 709–718, 2001.

[31] V. Giurgiutiu, "Embedded NDE with Piezoelectric Wafer- Active Sensors in Aerospace Applications," *J. Mater.*, vol. January, no. Special, 2003.

[32] A. N. Norris and C. Vemula, "Scattering of Flexural Waves on Thin Plates," *J. Sound Vib.*, vol. 181, no. 1, pp. 115–125, 1995.

[33] L. Moreau, M. Caleap, a. Velichko, and P. D. Wilcox, "Scattering of guided waves by flat-bottomed cavities with irregular shapes," *Wave Motion*, vol. 49, no. 2, pp. 375–387, 2012.

[34] T. Grahn, "Lamb wave scattering from a circular partly through-thickness hole in a plate," *Wave Motion*, vol. 37, no. 1, pp. 63–80, 2003.

[35] Y. Shen and V. Giurgiutiu, "Combined analytical FEM approach for efficient simulation of Lamb wave damage detection," *Ultrasonics*, vol. 69, pp. 116–128, 2016.

[36] Z. Sharif-Khodaei and M. H. Aliabadi, "Assessment of delay-and-sum algorithms

for damage detection in aluminium and composite plates," *Smart Mater. Struct.*, vol. 23, no. 7, p. 75007, 2014.

[37] S. Zhongqing and Y. Lin, *Identification of Damage Using Lamb Waves: From Fundamentals to Applications*, 2009th ed. Springer, 2009.

[38] S. Pavlopoulou, W. J. Staszewski, and C. Soutis, "Evaluation of instantaneous characteristics of guided ultrasonic waves for structural quality and health monitoring," *Struct. Control Heal. Monit.*, vol. 20, pp. 937–955, 2013.

[39] Y. Lu, L. Ye, Z. Su, and C. Yang, "Quantitative assessment of through-thickness crack size based on Lamb wave scattering in aluminium plates," *NDT E Int.*, vol. 41, no. 1, pp. 59–68, 2008.

[40] A. Golato, R. Demirli, and S. Santhanam, "Lamb wave scattering by a symmetric pair of surface-breaking cracks in a plate," *Wave Motion*, vol. 51, no. 8, pp. 1349–1363, 2014.

[41] A. Velichko and P. D. Wilcox, "Efficient finite element modeling of elastodynamic scattering with non-reflecting boundary conditions," in *Review of Progress in Quantitative Nondestructive Evaluation*, 2012, vol. 31, pp. 142–149.

[42] E. B. Flynn and M. D. Todd, "A Bayesian approach to optimal sensor placement for structural health monitoring with application to active sensing," *Mech. Syst. Signal Process.*, vol. 24, no. 4, pp. 891–903, 2010.

[43] E. B. Flynn and M. D. Todd, "Optimal Placement of Piezoelectric Actuators and Sensors for Detecting Damage in Plate Structures," *J. Intell. Mater. Syst. Struct.*, vol. 21, no. 3, pp. 265–274, 2010.

[44] P. Fromme and M. B. Sayir, "Detection of cracks at rivet holes using guided waves," *Ultrasonics*, vol. 40, no. 1–8, pp. 199–203, 2002.

[45] A. Srivastava and F. di Scalea, "On the existence of antisymmetric or symmetric Lamb waves at nonlinear higher harmonics," *J. Sound Vib.*, vol. 323, no. 3–5, pp. 932–943, 2009.

[46] E. Rahani and T. Kundu, "Modeling of Transient Ultrasonic Wave Propagation Using the Distributed Point Source Method," *IEEE Trans. Ultrason. Ferroelectr. Freq. Control*, vol. 58, no. 10, 2011.

[47] Z. Ahmad, J. Vivar-Perez, and U. Gabbert, "Semi-analytical finite element method for modeling of Lamb wave propagation," *CEAS Aeronaut J.*, vol. 4, pp. 21–33, 2013.

[48] Y. Yan, P. Li, and H. Lin, "Analysis and experimental validation of the middle-frequency vibro-acoustic coupling property for aircraft structural model based on the wave coupling hybrid FE-SEA method," *J. Sound Vib.*, vol. 371, pp. 227–236, 2016.

[49] E. Glushkov, N. Glushkova, A. Eremin, and V. Giurgiutiu, "Low-cost simulation of guided wave propagation in notched plate-like structures," *J. Sound Vib.*, vol. 352, pp. 80–91, 2015.

[50] S. Wang, S. Huang, and W. Zhao, "Simulation of Lamb wave's interactions with transverse internal defects in an elastic plate," *Ultrasonics*, vol. 51, no. 4, pp. 432–440, 2011.

[51] Y. Shen and V. Giurgiutiu, "Effective non-reflective boundary for Lamb waves: Theory, finite element implementation, and applications," *Wave Motion*, vol. 58, pp. 22–41, 2015.

[52] I. Trendafoilova, D. G. Gorman, and E. Manoach, “An Investigation on Vibration-based Damage Detection in Circular Plates,” *Struct. Heal. Monit.*, vol. 8, no. 4, pp. 291–302, 2009.

[53] J. N. Reddy, *An Introduction to the Finite Element Method*, 3rd ed. Newyork, NY: McGraw-Hill, 2006.

[54] J. Lysmer and R. Kuhlemeryer, “Finite-dynamic model for infinite media,” *J. Eng. Mech. Div*, vol. 95, no. 4, pp. 859–877, 1969.

[55] J. Liu, “Three dimensional viscoelastic artificial boundaries in time domain for wave motion problems,” *Eng. Mech.*, vol. 200, no. 6, pp. 46–51, 2005.

[56] S. Hosseini, S. Duczek, and U. Gabbert, “Non-reflecting boundary condition for Lamb wave propagation problems in honeycomb and CFRP plates using dashpot elements,” *Compos. Part B*, vol. 54, pp. 1–10, 2013.

[57] C. Wang and Z. Liu, “Realization of viscoelastic boundary condition in wave field simulation with ANSYS finite element software,” *J. Geod. Geodyn.*, vol. 32, no. 2, 2012.

[58] Y. Bhuiyan, Y. Shen, and V. Giurgiutiu, “Ultrasonic inspection of multiple-rivet-hole lap joint cracks using global analysis with local finite element approach,” in *Health Monitoring of Structural and Biological Systems 2016*, 2016, vol. 9805, pp. 1–15.

[59] Y. Shen and V. Giurgiutiu, “WFR-2D: an analytical model for PWAS-generated 2D ultrasonic guided wave propagation,” in *Proceedings of SPIE (Health Monitoring of Structural and Biological Systems)*, 2014, vol. 9064, p. 906411 1–13.

[60] B. Lin, A. Kamal, V. Giurgiutiu, and T. Kamas, “Multimodal Lamb Waves Power and Transfer Function Analysis of Structurally-bounded PWAS,” in *ASME SMASIS*, 2012.